Band structure renormalization at finite temperatures from first principles

Dissertation

zur Erlangung des akademischen Grades

Doctor rerum naturalium

(Dr. rer. nat.)

im Fach: Physik

Spezialisierung: Theoretische Physik

eingereicht an der

Mathematisch-Naturwissenschaftlichen Fakultät der

Humboldt-Universität zu Berlin

von

M.Sc. Nikita Rybin

Präsidentin der Humboldt-Universität zu Berlin:

Prof. Dr. Julia von Blumenthal

Dekanin der Mathematisch-Naturwissenschaftlichen Fakultät:

Prof. Dr. Caren Tischendorf

Gutachterinnen:

Prof. Dr. Claudia Draxl

Prof. Dr. Gabriel Bester

Prof. Dr. Samuel Poncé

Tag der mündlichen Prüfung: 10 Juli, 2023

Contents

Abstract

In English

In this thesis, we investigate the influence of electron-phonon interactions (EPI) on the band gap renormalization in crystalline solids at finite temperatures. The main goal is to identify the impact of the nuclear motion and the lattice thermal expansion on the band structure in a wide range of materials. For this purpose, the temperature influence on the EPI is calculated in the harmonic approximations by utilizing the stochastic sampling methodology and fully anharmonically, by performing *ab initio* molecular dynamics simulations (aiMD). The band gap at finite temperatures is extracted from the thermodynamically averaged spectral function, which is calculated using band-unfolding technique. While utilization of aiMD was already used for calculations of EPI the combination of aiMD and band-unfolding to treat the band gap renormalization was used only recently. In this thesis, we employed an improved band unfolding technique in order to effectively manage the calculations. This improved method incorporates several methodological innovations that serve to mitigate computational cost and minimize statistical noise in the final results. The updated method was thoroughly benchmarked, documented, and designed with a user-friendly interface. We present a comprehensive examination of the numerical aspects of thermodynamic averaging, the estimation of error bars, and the evaluation of convergence with respect to the size of the simulation supercell. Our established protocol enables the calculation of band gap renormalization at finite temperatures, which is in good agreement with prior theoretical studies and experimental data.

By utilizing aforementioned methodology, we evaluated the band gap renormalization in a collection of materials with varying structural types and levels of anharmonicity. This analysis contains an examination of the influence of quantum and classical treatments of the nuclear motion on the band gap renormalization. Furthermore, it enables an assessment of the impact of lattice dynamics anharmonicity on the band structure renormalization. The results indicate that materials with greater anharmonicities typically experience larger band gap renormalization at finite temperatures. These findings not only shed light on the underlying microscopic mechanisms of the band gap renormalization, but also have the potential to enable non-perturbative assessment of the charge transport coefficients. To illustrate this point, the electronic lifetimes of silicon were calculated. However, the convergence of the imaginary part of the electron-phonon self-energy with respect to the supercell size still presents a challenge and requires further methodological advancements.

Auf Deutsch

In dieser Doktorarbeit untersuchen wir den Einfluss von Elektron-Phonon-Wechselwirkungen (EPW) auf die Bandlückenrenormierung in kristallinen Festkörpern bei endlichen Temperaturen. Das Hauptziel besteht darin, den Einfluss der Kernbewegung und der thermischen Ausdehnung des Gitters auf die Bandstruktur in einer Vielzahl von Materialien zu quantifizieren. Zu diesem Zweck wird der Temperatureinfluss auf das EPW in harmonischen Näherungen unter Verwendung der stochastischen Abtastmethode und vollständig anharmonisch durch Durchführung von *ab initio* Molekulardynamiksimulationen (aiMD). Die Bandlücke bei endlichen Temperaturen wird aus der thermodynamisch gemittelten Spektralfunktion extrahiert, die unter Verwendung der Bandentfaltungstechnik berechnet wird. Während die Verwendung von aiMD bereits für Berechnungen von EPW verwendet wurde, wurde die Kombination von aiMD und Bandentfaltung zur Behandlung der Bandlücken renormalisierung erst kürzlich verwendet. In dieser Doktorarbeit haben wir eine verbesserte Bandentfaltungstechnik verwendet, um die Berechnung effektiv zu verwalten. Diese verbesserte Methode enthält mehrere methodische Neuerungen, die dazu dienen, den Rechenaufwand zu verringern und das statistische Rauschen in den Endergebnissen zu minimieren. Die aktualisierte Methode wurde gründlich bewertet, dokumentiert und mit einer benutzerfreundlichen Oberfläche gestaltet. Wir präsentieren eine umfassende Untersuchung der numerischen Aspekte der thermodynamischen Mittelung, der Schätzung von Fehlerbalken und der Bewertung der Konvergenz in Bezug auf die Größe der Simulationssuperzelle. Unser etabliertes Protokoll ermöglicht die Berechnung der Bandlückenrenormierung bei endlichen Temperaturen, was in guter Übereinstimmung mit früheren theoretischen Studien und experimentellen Daten steht.

Unter Verwendung der oben genannten Methodik haben wir die Bandlücken Renormalisierung in einer Sammlung von Materialien mit unterschiedlichen Strukturtypen und Anharmonizitätsgraden bewertet. Diese Analyse beinhaltet eine Untersuchung des Einflusses von Quanten- und klassischen Behandlungen der Kernbewegung auf die Bandlückenrenormierung. Darüber hinaus ermöglicht es eine Bewertung des Einflusses der Anharmonizität der Gitterdynamik auf die Renormierung der Bandstruktur. Die Ergebnisse zeigen, dass Materialien mit größeren Anharmonizitäten typischerweise eine größere Bandlückenrenormierung bei endlichen Temperaturen erfahren. Diese Ergebnisse werfen nicht nur Licht auf die zugrunde liegenden mikroskopischen Mechanismen der Bandlückenrenormierung, sondern haben auch das Potenzial, eine störungsfreie Bewertung der Ladungstransportkoeffizienten zu ermöglichen. Um diesen Punkt zu veranschaulichen, wurden die elektronischen Lebensdauern von Silizium berechnet. Die Konvergenz des Imaginärteils der Elektron-Phonon-Selbstenergie in Bezug auf die Größe der Superzelle stellt jedoch immer noch eine Herausforderung dar und erfordert weitere methodische Fortschritte.

Acknowledgements

This thesis is the outcome of the research conducted at the Fritz Haber Institute in Berlin and devoted to the exploration of electron-phonon interactions in crystals. I would like to thank my supervisor Christian Carbogno for his guidance and scientific advice throughout the research process. I acknowledge the financial support of the Max Planck Society, which was awarded by Matthias Scheffler, the director of the NOMAD laboratory. I am grateful to Alexander Paarman and Carsten Baldauf for their assistance in the final stages of the project through supporting my stay at the FHI through the International Max Planck Research School. Without this support, pursuing a doctoral degree would not have been possible. I also thank Committee members, Claudia Draxl, Gabriel Bester, and Samuel Poncé, for reviewing my thesis. I would like to express my gratitude to all members of the department, particularly Eugen Moerman, Florian Knoop, Karen Fidanyan, Dima Maksimov, Tom Purcell, and Sebastian Kokott. I thank Tanya Medvedeva for her support and understanding. This thesis is dedicated to my mother and grandmother, who valued my education more than anything else and provided tremendous support at every step of my life.

Nikita Rybin

Berlin, February 2023

Introduction

Advances in electronic-structure methods [1,2] and increasing functionality of computational software packages [3–6] now allow for routine calculations of various fundamental physical phenomena in materials science. In recent years, the interactions between electrons and lattice vibrations (phonons) have attracted considerable attention. These effects are the root of multiple effects [7–11], such as the temperature dependence of electronic energy states [12–22], charge transport [23–32], hot electrons dynamics [33,34], optical properties [35–39], polarons [40–44], and phonon-mediated superconductivity [45,46]. First principles calculations of the electron-phonon interactions (EPI) typically rely on density-functional theory (DFT) [47–50] or its linear-response extension density-functional perturbation theory (DFPT) [51,52].

Theoretical studies of the temperature influence on band structures have been started many years ago [53–56]. Nowadays, such investigations are usually performed using the so-called Allen-Heine-Cardona formalism [52,57,58]. This formalism originally relied on three approximations: (i) adiabatic approximation, (ii) the dependence of electronic states on nuclear motion is approximated in a Taylor series up to the second order and (iii) the potential energy surface is approximated by a harmonic model. Although pioneering first-principles calculations based on the AHC formalism appeared long time ago [59], the method has gained momentum recently, due to the development of practical computational schemes [60–62], which have been implemented in open-source programs [3, 16, 63–66], and because of the substantial increase in the capabilities of modern high-performance computers [67]. The limiting factor in the EPI evaluation is that the perturbative approach is not suited for materials in which the harmonic ansatz for lattice dynamics is not applicable. These materials are quite common [11, 68]. To account for anharmonicity, the harmonic approximation for lattice dynamics is extended by higher order perturbative calculations [69–73]. This allows to study the impact of anharmonic effects in highly-anharmonic superconductors [74,75] and calculate the band gap renormalization and electronic transport properties of anharmonic materials like SrTiO3 [76,77]. Notably, while the obtained trends of temperature-dependent mobility agrees with experiments, the absolute values differ from experimental results by an order of magnitude [77]. Whether polaronic effects, as later pointed out in another study [78], are solely responsible for this discrepancy or if higher-order terms of anharmonicity should be taken into account is an open question from our perspective.

In this thesis, we aim to quantitatively understand the EPI influence on the band gap renormalization at finite temperatures. We are specifically interested in investigating the impact of anharmonic effects, as this information is currently missing in the literature. To

address this challenge, we use a combination of fully anharmonic *ab initio* molecular dynamics simulations (aiMD) and band-unfolding technique [79–84] following the work [85]. To evaluate the EPI, wave functions calculated during the aiMD simulation are expanded as a linear combination of the static reference wave functions of the primitive cell. The obtained linear expansion coefficients contain information about the EPI [85] and allow to obtain vibronically averaged temperature-dependent spectral function [81, 82, 85] and evaluate band gap renormalization at finite temperatures.

This thesis is arranged as follows. The first section comprises the theoretical foundations of the concepts and tools employed in this work. In Chapter 1, we discuss the general electrons-nuclei many-body problem and Kohn-Sham DFT, which is used to perform first-principles calculation in this work. Chapter 2 introduces the methods utilized for lattice dynamics calculations, both the harmonic approximation and aiMD simulations. Then, in Chapter 3, the influence of temperature on the band structure is discussed. We will briefly discuss the AHC formalism, along with its advantages and limitations. Then we will show aforementioned approach based on the combination of the aiMD and band-unfolding technique, which overcomes limitations of the AHC formalism. In the same chapter, we will discuss the influence of the lattice thermal expansion (LTE) and the long-range electrostatic effects on the band gap value.

The second section of the thesis focuses on the benchmark and application of the methods outlined in the first section. In Chapter 4, the numerical aspects of band gap renormalization calculations and the influence of computational and physical parameters are discussed. This for instance includes the numerical aspects such as thermodynamic averaging, estimation of the error bars, and the influence of the supercell size used in simulations. For this benchmark we used diamond and zinc blende gallium nitride (GaN), since there is a large amount of reference data [16, 17, 52, 86–94]. Although the workflow follows recently published work [85], here we utilized an improved version of the band unfolding technique. An improvement is manifested in the better control over the simulation artifacts, and in several methodological advancements that alleviate the computational cost and reduce the statistical noise of calculations. Apart from being accurately tested, the current workflow is well documented and is managed using user-friendly interface, which can be coupled to any DFT code. Here, all calculations are performed with the FHI-aims code [5].

In Chapter 5, we systematically explore the role of different contributions to the band gap renormalization through calculations performed on a broad range of materials. These materials have different structural types (rock salt, zinc blende, wurtzite, fluorite, and antifluorite), exhibit a diversity of band gaps, bonding types (ionic and covalent), atomic masses, and lattice anharmonicity. We will demonstrate the distinctions between classical and quantum, as well as harmonic and anharmonic treatments of the nuclear motion. We will also explore how the ZPR and band gap renormalization at finite temperatures correlates with simple descriptors such as an amplitude of atomic vibrations and ionic mass. In addition, we disentangled the contributions of nuclear motion and lattice thermal expansion (LTE), quantified the role of different effects, and, in particular, showed the impact of anharmonicity. Finally, the thesis concludes with a summary of the results and an outlook on future steps, including considerations arising from our attempts to calculate electronic transport coefficients.

Chapter 1

Electronic structure methods

In this chapter, we briefly review essential concepts of *ab initio* (first-principles) calculations [95–97]. We will start with the non-relativistic time-independent Schrödinger equation and discuss the many-body problem. Then, we will present the Born-Oppenheimer approximation and show how to resolve the electronic structure problem by means of Density Functional Theory (DFT). We will also discuss characteristics of the FHI-aims (Fritz Haber Institute *ab initio* molecular simulations) package, which is used for all DFT calculations in this thesis.

1.1 The many-body problem

The static properties of the quantum mechanical many-body system consisting of electrons and nuclei can be obtained by solving the time-independent Schrödinger equation:

$$\hat{H}\Psi = E\Psi \tag{1.1}$$

where E is the total energy of the system and Ψ is a many-body wave function, which depends on the coordinates of N electrons and M nuclei:

$$\Psi(r, R) = \Psi(\{r_1, r_2, \ldots, r_N\}, \{R_1, R_2, \ldots, R_M\}) \tag{1.2}$$

The Hamiltonian $\hat{H}$ is given by[1]:

$$\hat{H} = \hat{T}_e + \hat{T}_n + \hat{V}_{ee} + \hat{V}_{nn} + \hat{V}_{en} = \underbrace{-\sum_{i=1}^{N}\frac{\nabla_i^2}{2} - \sum_{I=1}^{M}\frac{\nabla_I^2}{2M_I}}_{\text{kinetic energy}} + \underbrace{\frac{1}{2}\sum_{i\neq j}^{N}\frac{1}{|r_i - r_j|}}_{\text{e-e repulsion}} + \underbrace{\frac{1}{2}\sum_{I\neq J}^{M}\frac{Z_I Z_J}{|R_I - R_J|}}_{\text{n-n repulsion}} - \underbrace{\frac{1}{2}\sum_{i,I}^{N,M}\frac{Z_I}{|r_i - R_I|}}_{\text{e-n attraction}} \tag{1.3}$$

where Z_I, Z_J are charges of nuclei I and J, M_I is the mass of ion I, while N and M are the number of electrons and nuclei, respectively. We denote $\hat{T}_e$ as the kinetic energy operator for the electrons, $\hat{T}_n$ as the kinetic energy operator for the nuclei, $\hat{V}_{ee}$ as the repulsive

[1] We will use atomic units, i.e $m_e = \hbar = \frac{1}{4}\pi\epsilon_0 = e = 1$, where m_e is the mass of electron, $\hbar$ is Plank's constant, ϵ_0 is the vacuum permittivity, e is the electron charge.

interaction of electrons, $\hat{V}_{nn}$ as the repulsive interaction between nuclei, and $\hat{V}_{en}$ as the attractive interaction between nuclei and electrons.

In practice, the time-independent Schrödinger equation Eq. (1.1) can only be solved analytically for simple systems, such as the hydrogen atom or an ionized hydrogen molecule [98]. However, solutions for systems with many electrons are not feasible to obtain even numerically, due to the exponential increase in complexity with system size [49]. This complexity arises from the many-body wave function and the presence of the electron-electron repulsion term in the Hamiltonian. We can naively estimate how hard it is to deal with the full many-body wave function, by estimating the cost of a numerical solution of the Schrödinger equation for silicon. The unit cell of silicon contains 2 atoms and the lattice constant of this unit cell is 5.43 Å. We will consider only valence electrons. Thus, each silicon atom will contribute 4 electrons, in couple with 2 nuclei it means that the silicon unit cell is described by a wave function of 10 variables $\Psi(r_1, r_2, \ldots, r_8; R_1, R_2)$. We can sample the unit cell using a uniform grid with a step size of 0.1 Å in each direction. This means that approximately 40000 points are used. The wave function of Si contains $\approx 10^{46}$ complex numbers and manipulating objects of such size is outright impossible – there is simply not enough computer memory on the whole planet to store such an object. Therefore, due to the practical complexity of the Schrödinger equation many approximations were developed. We will discuss the approximations needed to proceed to practical calculations in the following sections.

1.2 The Born-Oppenheimer approximation

The many-body problem can be simplified by separating the electrons and nuclei dynamics through the Born-Oppenheimer approximation, which is valid since electrons have much smaller mass than nuclei and can adjust their positions to remain in the lowest energy state at each time step of the nuclear movement [99]. The Hamiltonian in Eq.(1.3) can be separated into the part related to the electrons and the part related to the nuclei, which allows to work with an electronic sub-Hilbert space H_e of the total Hilbert space $H = H_e \bigotimes H_n$ of electron-nuclei states. The Schödinger equation for electrons reads:

$$\hat{H}_e \left|\phi_\nu(r;R)\right\rangle = E^e_\nu \left|\phi_\nu(r;R)\right\rangle \tag{1.4}$$

where the E^e_ν are eigenvalues of the electronic Hamiltonian $\hat{H}_e$ for a given nuclear configuration $\{R\}$ and $\phi_\nu(r;R)$ are its eigenfunctions. $\hat{H}_e$ is the Hamiltonian for interacting electrons, which move in an external field generated by the stationary nuclei:

$$\hat{H}_e = \underbrace{-\sum_{i=1}^{N} \frac{\nabla_i^2}{2}}_{\text{e kinetic energy}} + \underbrace{\frac{1}{2}\sum_{i\neq j}^{N} \frac{1}{|r_i - r_j|}}_{\text{e-e repulsion}} - \underbrace{\frac{1}{2}\sum_{i,I}^{N,M} \frac{Z_I}{|r_i - R_I|}}_{\text{e-n attraction}} \tag{1.5}$$

Since the electronic Hamiltonian $\hat{H}_e$ is Hermitian, its eigenvectors $\phi_\nu(r;R)$ define a complete orthonormal basis for each set of nuclear coordinates. The many-body wave function $\Psi(r,R)$ introduced in Eq. (1.2) can be expanded in this basis:

$$\left|\Psi(r,R)\right\rangle = \sum_\nu C_\nu(R) \left|\phi_\nu(r;R)\right\rangle \tag{1.6}$$

where the expansion coefficients $C_\nu(R)$ depend on the nuclear configuration.

Substituting Eq. (1.6) into Eq. (1.1), multiplying the resulting equation by ϕ_μ^* from the left, and integrating it, we obtain:

$$\langle\phi_\mu|\hat{H}|\sum_\nu C_\nu\phi_\nu\rangle = E\,\langle\phi_\mu|\sum_\nu C_\nu\phi_\nu\rangle = EC_\mu \tag{1.7}$$

where we have used the fact that electronic Hamiltonian eigenfunctions are orthonormal:

$$\langle\phi_i|\phi_j\rangle = \delta_{ij} \text{ and } \sum_i C_i\,\langle\phi_i|\phi_j\rangle = C_j \tag{1.8}$$

Then, we decompose the Hamiltonian in Eq. (1.3) into electronic and nuclear parts and utilize the chain rule for derivatives, to obtain:

$$\sum_\nu \langle\phi_\mu|\hat{H}_e + \hat{T}_n + \hat{V}_{nn}|C_\nu\phi_\nu\rangle = \\ [E_\mu^e + \hat{V}_{nn}]C_\mu - \sum_{\nu,I}\frac{\hbar^2}{2M_I}[\langle\phi_\mu|\nabla_I^2|\phi_\nu\rangle\,C_\nu + 2\,\langle\phi_\mu|\nabla_I|\phi_\nu\rangle\,\nabla_I C_\nu] \tag{1.9}$$

The second and the third terms on the right-hand side are called adiabatic and non-adiabatic terms, respectively. To this point, no approximations have been introduced in our analysis. However, for practical applications it is necessary to utilize two approximations:

1. The terms $\langle\phi_\mu|\hat{T}_n|\phi_\nu\rangle$ with $\mu \neq \nu$ are non-diagonal coupling terms. They represent the transition of an electron from the state μ to the state ν caused by nuclear motion. We will assume that atomic motion does not induce electronic excitations, consequently:

   $$\langle\phi_\mu|\nabla_I|\phi_\nu\rangle = 0, \text{ for } \mu \neq \nu \tag{1.10}$$

   The detailed discussion of the validity of this approximation is presented in [100]

2. Then we assume that the second term on the right-hand side of Eq. (1.9) is small. This can be substantiated by comparing this term to its electronic counterpart:

   $$|\,\langle\phi_\mu|\nabla_I^2|\phi_\mu\rangle\,| \leq \langle\phi_\mu|\nabla_i^2|\phi_\mu\rangle\,| \tag{1.11}$$

   Then one can estimate an upper bound:

   $$|\frac{\hbar^2}{2M_I}\,\langle\phi_\mu|\nabla_I^2|\phi_\mu\rangle\,| \leq |\frac{m_e}{M_I}\frac{\hbar^2}{2m_e}\,\langle\phi_\mu|\nabla_i^2|\phi_\mu\rangle\,| \tag{1.12}$$

   Here, we multiplied Eq. (1.11) by $\hbar^2/2M_I$ from both sides and used the identity $m_e/m_e = 1$. Neglecting diagonal terms $\langle\phi_\mu|\nabla_I|\phi_\mu\rangle$ is reasonable, because the electron-to-proton mass ratio is $\approx 5\cdot 10^{-4}$.

In the remainder of this thesis, we will assume that nuclei move on the Born-Oppenheimer Potential Energy Surface (BO-PES). This is described by the following equation:

$$V_{\mathrm{BO}}(R) = E_0^e(R) + V_{nn}(R) \tag{1.13}$$

where $V_{\mathrm{BO}}(R)$ is the BO-PES, $E_0^e(R)$ is the ground state energy of the electronic system, and $V_{nn}(R)$ denotes the repulsion between nuclei.

1.3 Density-functional theory

The electronic structure problem is defined as a problem in which one has to find a solution for the electronic Schrödinger Eq. (1.4) assuming that the nuclear positions are fixed, as introduced in the previous section. The Rayleigh-Ritz minimization principle can be used to find the energy of the electronic ground-state:

$$E_0 = E[\psi_o] \leq E[\psi] = \frac{\langle\psi|\hat{H}_e|\psi\rangle}{\langle\psi|\psi\rangle} \tag{1.14}$$

where E_0 and ψ_0 denote the ground-state energy and wave function, respectively. $\hat{H}_e$ is the electronic Hamiltonian introduced in Eq. (1.5), and ψ is some normalized trial wave function.

Although the eigenvalue problem introduced in Eq. (1.4) is simplified to a minimization problem written in Eq. (1.14), the solution is hard to obtain due to the huge Hilbert space that is spanned by the many-body electronic problem. To circumvent this problem, a number of so-called wave function based methods were developed [101–103]. For example, in the Hartree-Fock (HF) approximation [104, 105] the electronic trial electronic wave function is represented in the form of a Slater determinant. The HF method yields an approximate solution of the electronic Schrödinger equation by treating electrons as free particles existing in mean-field electrostatic and exchange potentials, which is also created by these particles. The ground-state energy of a system in the HF method is computed in an iterative manner, i.e., calculations are started from a set of initially guessed orbitals, which are then updated using Hartree-Fock equations, and the new orbitals are then used to obtain the new total energy. The calculation runs until the difference between input and output total energy does not exceed some predetermined threshold.

The Hartree-Fock method is a mean-field method that was widely used in quantum chemistry to approximate the electronic structure of molecules and solids [102,103,106]. It is generally quite successful at predicting the ground state energy and geometry of a molecule, but it can fail when the system has strong electron correlations or if the system has a multi-reference character, meaning that it has multiple configurations that are nearly degenerate in energy. Increasing the accuracy of wave function based methods comes with higher computational cost [107], limiting the applicability of these methods [102].

An alternative approach was suggested by Thomas and Fermi who proposed a method for calculating the energy of a system based on the assumption that the electron density is the fundamental quantity that can describe many-body electron-nuclei systems [108, 109]. The Thomas-Fermi theory served as a precursor to the groundbreaking density-functional theory (DFT) [47–49] – a widely used framework in the computational materials science community. In DFT, similarly to the Thomas-Fermi theory, the N-electron wave function is replaced by the electron density that depends only on three Cartesian coordinates. The electron density of the ground-state can be obtained from the N-electron wave function by integration:

$$n_0(r) = N \int |\Psi_0(r, r_2, \ldots, r_N)|^2 dr_2 \ldots dr_N \tag{1.15}$$

where N is the number of electrons, and $\Psi_0(r)$ is the ground state wave function of the electronic system.

DFT relies on two theorems [47] and the practical applicability of the method is based on the scheme proposed by Kohn and Sham [48]. Below we present a brief discussion of the DFT formalism. More details can be found in literature [49, 50, 95–97, 110, 111].

The Hohenberg-Kohn theorems

The first Hohenberg-Kohn theorem states that there is a one-to-one mapping between the electronic ground-state density $n_0(r)$ and the external potential V_{ext}, where by the external potential we mean the electron-nuclear attraction term of Eq. (1.3).

For the non-degenerate electronic ground state the proof can be done by considering two different external potentials V_{ext} and V'_{ext} that differ from each other by more than an additive constant. To start, assume that they give rise to the exactly same ground-state electron density $n_0(r)$. The external potential V_{ext} corresponds to the Hamiltonian $\hat{H}$, the ground state wave function Ψ, and the energy E. Similarly, V'_{ext} corresponds to Ψ' (it is necessary that $\Psi' \neq e^{i\theta}\Psi$), $\hat{H}'$, and E'. Then, we can utilize the Rayleigh-Ritz minimal principle:

$$E < \langle \Psi' | \hat{H} | \Psi' \rangle = E' - \langle \Psi' | (V'_{\text{ext}} - V_{\text{ext}}) | \Psi' \rangle = E' - \int dr n_0(r)[V'_{\text{ext}} - V_{\text{ext}}] \tag{1.16}$$

Since Ψ is not the ground state of the system determined by V'_n:

$$E' < \langle \Psi | \hat{H}' | \Psi \rangle = E - \int dr n_0(r)[V_{\text{ext}} - V'_{\text{ext}}] \tag{1.17}$$

Adding Eqs. (1.16) and (1.17) leads to the contradiction:

$$E + E' < E + E' \tag{1.18}$$

Thus, we conclude that the assumption of the existence of a second external potential V'_{ext}, which is equal to the potential V_{ext} up to an additive constant and gives the same $n_0(r)$ must be wrong. The theorem was also proved for the degenerate case, as discussed in [110].

The second Hohenberg-Kohn theorem states that for the static external potential V_{ext}, there exist a universal Hohenberg-Kohn functional $F[n(r)]$ of the electron density $n(r)$, which is independent of V_{ext}. Its energy can be written as:

$$E[n(r)] = \int d^3 r n(r) V_{\text{ext}} + F[n(r)] \tag{1.19}$$

and for any external potential V_{ext} the ground-state electron density $n_0(r)$ minimizes the energy functional $E[n(r)]$ such that:

$$E_0 = E[n_0(r)] \leq E[n(r)] \tag{1.20}$$

The introduction of the Hohenberg-Kohn theorems allows to resolve the many-body problem for the electronic ground-state, if the form of the universal functional $F([n(r)])$ is known. In order to proceed to the discussion of this functional form, we again have to reintroduce the electronic orbitals and make the problem again dependent on the number of electrons. This is achieved by introducing the Kohn-Sham equations.

The Kohn-Sham equations

To construct practical solution to the electronic structure problem, Kohn and Sham suggested [48] to consider an auxiliary, fictitious system of N non-interacting electrons with the same density $n(r)$ as the real system with N interacting electrons. Then the universal functional $F[n(r)]$ of the system of interacting electrons introduced in Eq. (1.19) can be written as:

$$F[n(r)] = \hat{T}_e^s[n(r)] + \hat{E}_{\rm H}[n(r)] + \hat{E}_{\rm xc}[n(r)] \tag{1.21}$$

where $\hat{T}_e^s[n(r)]$ is the kinetic energy operator of the non-interacting electrons:

$$\hat{T}_e^s[n(r)] = -\frac{1}{2}\sum_{i=1}^{N}\int \psi_i^*(r)\nabla^2\psi_i(r)dr \tag{1.22}$$

where $\phi_i(r)$ are auxiliary one-electron orbitals, orthonormal by construction. $\hat{E}_{\rm H}[n(r)]$ is the electrostatic energy (Hartree energy) of the electrons :

$$\hat{E}_{\rm H}[n(r)] = \frac{1}{2}\int\int \frac{n(r)n(r')}{|r-r'|}drdr' \tag{1.23}$$

Finally, $\hat{E}_{\rm xc}[n(r)]$ is the so-called exchange-correlation (xc) functional, which contains the entire difference between the true system and the auxiliary system:

$$\hat{E}_{\rm xc}[n(r)] = \hat{T}_e - \hat{T}_e^s + \hat{V}_{ee}[n(r)] - \hat{E}_{\rm H}[n(r)] \tag{1.24}$$

where $\hat{T}_e$ is the kinetic energy operator of interacting electrons.

The energy functional $E[n(r)]$ can then be written as:

$$E[n(r)] = \hat{T}_e^s[n(r)] + \hat{E}_{\rm H}[n(r)] + \hat{E}_{\rm xc}[n(r)] + \hat{V}_{en}[n(r)] = \underbrace{\int drn(r)V_{\rm ext}(r)}_{\text{External potential}} - \underbrace{\sum_i \int dr\phi_i^*(r)\frac{\nabla^2}{2}\phi_i(r)}_{\text{Kinetic energy}} + \underbrace{\frac{1}{2}\int\int drdr'\frac{n(r)n(r')}{|r-r'|}}_{\text{Hartree energy}} + E_{\rm xc}[n] \tag{1.25}$$

The Hohenberg-Kohn variational principle introduced in Eq. (1.20) in the combination with the method of Lagrange multipliers allows us to write a problem for a given number of electrons in the following form [47, 48]:

$$\epsilon = \frac{\delta E[n(r)]}{\delta n(r)} = \frac{\delta \hat{T}_e^s[n(r)]}{\delta n(r)} + \frac{\delta \hat{E}_{\rm xc}[n(r)]}{\delta n(r)} + \frac{\delta \hat{V}_{en}[n(r)]}{\delta n(r)} + \frac{\delta \hat{E}_{\rm H}[n(r)]}{\delta n(r)} = \frac{\delta \hat{T}_e^s[n(r)]}{\delta n(r)} + V_{\rm H} + V_{\rm ext} + V_{\rm xc} = \frac{\delta \hat{T}_e^s[n(r)]}{\delta n(r)} + V_{\rm eff} \tag{1.26}$$

where ϵ is a Lagrange multiplier chosen in such a way that the Kohn-Sham orbitals $\phi(r)$ are orthonormal. We have also introduced an effective potential $V_{\rm eff}$, which contains the xc-potential, Hartree potential and the external potential. The xc potential $\hat{V}_{\rm xc}$ and the Hartree potential $\hat{V}_{\rm H}(r)$ are defined as:

$$\hat{V}_{\rm xc} = \frac{\delta E_{\rm xc}[n(r)]}{\delta n(r)} \tag{1.27}$$

$$\hat{V}_{\mathrm{H}}(r) = \frac{\delta E_{\mathrm{H}}[n(r)]}{\delta n(r)} = \int \frac{n(r')}{|r - r'|} dr' \tag{1.28}$$

The treatment of the electronic structure problem in the case of the independent electron approximation, i.e., when neither exchange nor correlation terms are taken into account, leads to the equation with a similar structure:

$$\epsilon' = \frac{\delta E'[n(r)]}{\delta n(r)} = \frac{\delta \hat{T}_e^s[n(r)]}{\delta n(r)} + \frac{\delta \hat{V}_{en}[n(r)]}{\delta n(r)} = \frac{\delta \hat{T}_e^s[n(r)]}{\delta n(r)} + V_{\mathrm{ext}} \tag{1.29}$$

where ϵ' and $E'[n(r)]$ are a Lagrange multiplier and an energy functional defined in the independent electron approximation problem.

The similarity between Eqs. (1.26 and 1.29) allows to map the problem of N interacting electrons moving in an external field V_{ext} to the problem of N non-interacting electrons moving in an effective potential V_{eff}. Consequently, the solution for the electronic structure problem is presented as a single Slater Determinant of Kohn-Sham orbitals $\phi_i(r)$, which are obtained by solving single-particle Kohn-Sham equations [47, 49]:

$$h^{\mathrm{KS}} \phi_i(r) = \epsilon_i \phi_i(r) \tag{1.30}$$

$$\left[-\frac{1}{2}\nabla^2 + \underbrace{\hat{V}_{\mathrm{ext}}(r) + \hat{V}_{\mathrm{H}}(r) + \hat{V}_{\mathrm{xc}}}_{V_{\mathrm{eff}}} \right] \phi_i(r) = \epsilon_i \phi_i(r) \tag{1.31}$$

where h^{KS} denotes Kohn-Sham Hamiltonian.

Since the effective potential is electronic density-dependent the DFT problem has to be solved iteratively, similarly as in the HF approach [102]. If the electron density $n_0(r) = \sum_i^N |\psi_i(r)|^2$ is calculated, the total energy is determined as:

$$E = \sum_{i=1}^{N} \epsilon_i - \frac{1}{2} \int \int \frac{n(r) n(r')}{|r - r'|} dr dr' + E_{\mathrm{xc}}[n(r)] - \int n(r) V_{\mathrm{xc}}(r) dr \tag{1.32}$$

DFT is, in principle, exact assuming that the exact xc-functional $E_{\mathrm{xc}}[n(r)]$ is known. In practice, the exact xc-functional is not known and is obtained using a variety of approximations [112, 113]. The accuracy of the ground-state DFT depends entirely on the choice of the xc-functional [49] and increasing the accuracy comes with increasing computational cost [112].

Exchange-correlation functionals

In this subsection, we review the functionals used in this thesis. We will briefly outline the local density approximation (LDA), which was presented in the seminal paper of Kohn and Hohenberg [48] and the generalized gradient approximation (GGA) [114]. In this thesis, we used PBE [114] and PBEsol [115] GGA-type xc-functionals. In addition, we will discuss the hybrid [116] xc-functional HSE06 [117]. Detailed discussions of the different aspects of xc-functionals can be found in literature [111].

Local density approximation

In the LDA it is assumed that the electronic density varies slowly in space and the system can be approximated by a homogeneous electron gas (HEG), which is an idealized system of electrons situated in an infinite background of positive charge, specified with the local density at each point of space. LDA allows to describe the xc-functional as a function of the electronic density with the analytical form [118]:

$$E_{\mathrm{xc}}[n] \approxeq E_{\mathrm{xc}}^{\mathrm{LDA}}[n(r)] = \int n(r)\epsilon_{\mathrm{xc}}^{\mathrm{HEG}}[n(r)]dr = \int n(r)\left[\epsilon_{\mathrm{x}}^{\mathrm{HEG}}(n(r)) + \epsilon_{\mathrm{c}}^{\mathrm{HEG}}(n(r))\right]dr \quad (1.33)$$

where the ϵ_{xc} term is decomposed into exchange ϵ_{x} and correlation ϵ_{c} terms. The exchange term for the HEG can be derived analytically [118]:

$$\epsilon_{\mathrm{x}}^{\mathrm{HEG}}(n) = -\frac{3}{4}\left(\frac{3n}{\pi}\right)^{1/3} \quad (1.34)$$

The correlation term can be calculated to a very good degree using many-body perturbation theory [119] or nearly exactly by means of the Quantum Monte Carlo techniques [120]. The latter approach allows to obtain the fitted analytical form of the correlation term as was done by Perdew and Wang [121]. In this thesis, we used the LDA xc-functional parameterized using this Perdew-Wang approach [121].

Although, the validity of the LDA is limited to systems with a uniform or slightly-varying density, it appears to produce qualitatively and partially even quantitatively accurate results for systems with inhomogeneous density [50, 102, 103]. Well-known drawbacks of LDA xc-functionals is the underestimation of lattice constants [122,123], related to the overestimation of binding energies, and the systematic underestimation of band gaps [124–126].

Generalized gradient approximation

The Generalized Gradient Approximation (GGA) xc-functionals utilize not only the local values of the electronic density, but also its gradient to account for the inhomogeneity of the electron density:

$$E_{\mathrm{xc}}[n] \approxeq E_{\mathrm{xc}}^{\mathrm{GGA}}[n(r), \nabla n(r)] = \int n(r)\epsilon_{\mathrm{x}}^{\mathrm{HEG}}[n(r)]F_{\mathrm{xc}}[n(r), \nabla n(r)]dr \quad (1.35)$$

Since there is no one unique recipe for obtaining $F_{\mathrm{xc}}\left[n(r), \nabla n(r)\right]$, a variety of functionals have been introduced under the name GGA-type xc-functionals. Most widely used are PBE [114], and its re-optimized version for solids PBEsol [115] (PBEsol improves the prediction of lattice parameters). The derivation of $E_{\mathrm{xc}}^{\mathrm{PBE}}[n(r)]$ is discussed in [114].

The PBE xc-functional is generally more accurate than the LDA xc-functional and at the same time does not increase the computational cost substantially. However, PBE is also not able to precisely determine lattice constants, since its underestimation of binding energies leads to an overestimation of structural parameters. This drawback is arguably alleviated once PBEsol [115] is utilized.

Hybrid functionals

One of the main drawbacks of the xc-functionals mentioned so far is the considerable underestimation of electronic band gaps [124, 127]. This is often caused by the so-called over-delocalization error widely described in literature [124,126,128–134]. Hybrid xc-functionals [135] do not resolve over-delocalization error, but allow to compute band gaps with the higher accuracy than LDA and GGA xc-functionals [136, 137]. Hybrid xc-functionals are constructed by adding a portion of exact exchange from HF theory:

$$E_{\mathrm{xc}}[n(r)] \approxeq \alpha E_{\mathrm{x}}^{\mathrm{HF}} + (1-\alpha)E_{\mathrm{x}}^{\mathrm{GGA}}[n(r)] + E_{\mathrm{c}}^{\mathrm{GGA}}[n(r)] \tag{1.36}$$

where $E_{\mathrm{x}}^{\mathrm{HF}}$ is the exact exchange calculated using the HF approach, and α=0.25 is a parameter, which determines the portion of the exact exchange. The exact exchange explicitly depends on the one-electron orbitals:

$$E_{\mathrm{x}}^{\mathrm{HF}} = -\frac{1}{2}\sum_{ij}^{N}\int\int \frac{\psi_i^*(r)\psi_j^*(r')\psi_j(r)\psi_i(r')}{|r-r'|}drdr' \tag{1.37}$$

The one-electron orbitals then become solutions to the generalized Kohn-Sham equations [138, 139]:

$$\left[-\frac{1}{2}\nabla^2 + V_{\mathrm{loc}}\right]\psi_i(r) + \int V_x^{\mathrm{HF}}(r,r')\psi_i(r')dr' = \epsilon_i\psi_i(r) \tag{1.38}$$

where V_{loc} is a GGA potential and a fraction α of the GGA exchange potential is replaced with the HF exchange V_x^{HF}. The non-locality of the exact (HF) exchange makes a numerical solution expensive. Somewhat of a simplification can be done by separating the Coulomb operator into short-range and long-range terms:

$$\frac{1}{r} = \underbrace{\frac{\mathrm{erfc}(\omega r)}{r}}_{\text{short-range}} + \underbrace{\frac{\mathrm{erf}(\omega r)}{r}}_{\text{long-range}} \tag{1.39}$$

where the complementary error function is defined as $\mathrm{erfc}(\omega r) = 1 - \mathrm{erf}(\omega r)$, and ω is an adjustable parameter [116, 136, 140].

The separation of the Coulomb operator and utilization of a screened short-range exchange was suggested by Heyd, Scuseria and Ernzerhof, hence functionals constructed in such a way are called HSE hybrid functionals [116] and have the following form:

$$E_{\mathrm{xc}}^{\mathrm{HSE}}[n] = \alpha\,\underbrace{E_{\mathrm{x}}^{\mathrm{HF}}(\omega)}_{\text{short-range}} + (1-\alpha)\,\underbrace{E_{\mathrm{x}}^{\mathrm{PBE}}(\omega)}_{\text{short-range}} + \underbrace{E_{\mathrm{x}}^{\mathrm{PBE}}(\omega)}_{\text{long-range}} + E_{\mathrm{c}}^{\mathrm{PBE}} \tag{1.40}$$

In this thesis we will use the HSE06 [117] (ω=0.11 bohr^{-1} and α=0.25) xc-functional to inspect the reliability of the band gap renormalization calculated with LDA or PBEsol. The implementation of this xc-functional in the FHI-aims code is described in detail in [141].

Electronic structure calculations with FHI-aims

A numerical solution of the Kohn-Sham equations is in practice pursued by expanding the single-particle Kohn-Sham states $\psi_i(r)$ in some basis set:

$$\psi_i(r) = \sum_{j=1}^{N_{basis}} C_{ij}\phi_j(r) \tag{1.41}$$

where N_{basis} is the number of basis functions used for the linear expansion, which has to be reasonably larger than the number of Kohn-Sham eigenfunctions ψ_i.

Expansion of the Kohn-Sham eigenfunctions introduced in Eq. (1.41) reduces the Kohn-Sham equations to a matrix equation for the coefficients C_{ij}, which can be solved using standard matrix diagonalization techniques. Different DFT codes feature different types of basis sets, e.g., plane waves [6], projector-augmented waves [4, 142], Gaussian-type orbitals [143] and many others. In this thesis, we used the FHI-aims package (Fritz Haber Institute ab initio molecular simulation package) [5] for all DFT calculations. FHI-aims is an all-electron, full-potential electronic structure code, which utilizes numeric atom-centered orbitals (NAOs) as its basis set. The basis functions in FHI-aims are of the following form:

$$\phi_i(r) = \frac{u_i(r)}{r} Y_{l,m}(\Omega) \tag{1.42}$$

with the spherical harmonics $Y_{l,m}(\Omega)$ and the numerically tabulated radial functions $u_i(\mathbf{r})$, which are obtained by solving the radial Schrödinger-like equation on a logarithmic grid [144]:

$$\left[-\frac{1}{2}\nabla_r^2 + \frac{l(l+1)}{r^2} + v_i(r) + v_{cut}(r)\right] u_i(r) = \epsilon_i u_i(r) \tag{1.43}$$

where $v_i(r)$ is the potential that determines the shape of radial function and $v_{cut}(r)$ is the confining potential of the following form:

$$v_{cut}(r) = \begin{cases} 0, & r \leq r_{onset} \\ s \cdot \exp\left[\frac{r_{cut}-r_{onset}}{r-r_{onset}}\right] \cdot \frac{1}{(r-r_{cut})^2}, & r_{onset} < r < r_{cut} \\ \infty, & r \geq r_{cut} \end{cases} \tag{1.44}$$

where s is a global scaling parameter. Usage of the confining potential allows to obtain smooth basis functions without long tails once $r \to \infty$. Interested readers can read the technical details of the methods used in FHI-aims in [5] and references therein (for example, the optimized partitioning of the integration grids are presented in [144–146]).

The minimal basis contains core and valence basis functions, which were constructed from the spherically symmetric free atoms. This rather crude choice gives a sufficiently good description of the strongly oscillatory behavior of the wave function near the nucleus. Then hydrogen-like and free-ion-like radial functions with different angular momenta are added to the minimal basis. Basis functions in FHI-aims are constructed for each chemical element and arranged hierarchically into *tiers*. Separation into different *tiers* is done based on the improvements of the LDA total energy of a dimer for each chemical element once particular *tier* settings are used. Inclusion of basis functions from higher *tiers* increases the number of basis function and consequently the accuracy of a calculation. The numerical accuracy (and of course the cost of calculations) also depends on the density of the integration grid. For production calculations all numerical settings have to be reasonably chosen and physical conclusions have to be drawn based on converged numerical settings.

Once Kohn-Sham eigenfunctions are expanded in a linear combination of basis functions with the linear expansion coefficients C_{ij}, one can obtain a generalized eigenvalue problem:

$$\sum_j h_{ij} C_{jl} = \epsilon_l \sum_j s_{ij} C_{jl} \tag{1.45}$$

where h_{ij} and s_{ij} denote the matrix elements of the Kohn-Sham Hamiltonian introduced in Eqs. (1.30 and 1.31) $h_{ij} = \langle \phi_i | h^{KS} | \phi_j \rangle$ and the overlap matrix $s_{ij} = \langle \phi_i | \phi_j \rangle$, respectively.

The generalized Kohn-Sham eigenvalue problem Eq. (1.45) is solved in an iterative, self-consistent way [147] (denoted as self-consistent field (SCF) calculations from now on). The SCF cycle begins with an initial guess for the electron density n_0, which can be constructed from the superposition of the constituent atomic densities. Then n_0 is used to compute the Hartree and exchange-correlation potentials. The matrix elements of the Kohn-Sham Hamiltonian are then computed and used to solve Eq. (1.45). The overlap matrix is computed only once, since it does not change during the SCF cycle. The algebraic procedures, which are performed during the SCF cycle, are powered by the ELPA (eigenvalue solvers for petascale applications) library [148]. The coefficients of the linear expansion C_{ij} from Eq. (1.45) are used to obtain a new electronic density n_0^{out}, which is used to generate an input density n_1^{in} for the next SCF step. This algorithm is then repeated until the difference between the electronic densities of consecutive steps becomes smaller than some particular threshold. Generating a new input density is a crucial part of the algorithm, which has a substantial influence on the stability and speed of the SCF convergence. We performed all calculations with the Pulay mixer scheme [149].

1.4 The periodic boundary conditions

In this thesis we will only consider ideal crystals and will not take into consideration structures with defects, impurities, glasses, or amorphous solids. A crystal structure is denoted as a periodic lattice with a basis, which contains a certain number of atoms or molecules. The smallest cell from which the crystal can be constructed by translations is called the unit cell. The unit cell choice has some arbitrariness, so the unit cell with the smallest volume and the highest symmetry among all possible unit cells is called a primitive cell. Lattice parameters and atomic coordinates constitute the main input for any computational simulation. For a three-dimensional crystal the unit cell is described by three lattice vectors a_1, a_2, a_3 (Bravais lattice vectors), which can be used to build an infinitely big crystal by translating the unit cell along them. Hence, the position of any lattice point R can be described by using a linear combination of lattice vectors:

$$R(n) = n_1 a_1 + n_2 a_2 + n_3 a_3, n_i \in \mathbb{Z} \tag{1.46}$$

If the unit cell contains M atoms, the position of any atom is determined with respect to the origin by using a set of vectors $R(l)$. For example, the l-th atom in the n-th unit cell has the position:

$$R(n, l) = R(n) + R(l) \tag{1.47}$$

The presence of translational symmetry in the crystal allows to use Bloch's theorem [9] for the Kohn-Sham orbitals and present them as plane waves modulated with a function that

has the periodicity of the lattice $u_{nk}(r) = u_{nk}(r + R(n))$:

$$\psi_{nk}(r) = e^{ikr} u_{nk}(r) \tag{1.48}$$

Then, the eigenfunctions ψ_{nk} and also eigenvalues ϵ_{nk} are labeled by two quantum numbers: band index n and wave vector k. Eigenfunctions ψ_{nk} should satisfy the Born-von Karman (BvK) boundary conditions. This implies that:

$$\psi_{nk}(r + R(n)) = \psi_{nk}(r) \tag{1.49}$$

where $R(n)$ denotes the number of repetitions along lattice vectors a_i introduced in Eq. (1.46) and means that the BvK supercell contains n unit cells. Consequently, the BvK conditions and the periodicity of the modulation function $u_{nk}(r)$ introduced in Eq. (1.48) determine the allowed values of k:

$$k = \sum_{i=1}^{3} \frac{m_i}{n_i} b_i, \text{ where } m_i = 0, 1, \ldots, ni - 1 \tag{1.50}$$

Thus, in total there are as many allowed values of k as there are unit cells in the crystal, i.e., there are $n = n_1 \times n_2 \times n_3$ unique values of wave vector k labeled by m_i that are expressed in terms of the reciprocal lattice vectors b_i. The reciprocal lattice is generated by these translation vectors b_i (analogously to the real space unit cell and translation vectors a_i), such that $a_i \cdot b_i = 2\pi\delta_{ij}$. The primitive cell in the reciprocal space defines the first Brillouin zone (BZ). The relationship introduced in Eq. (1.50) shows that the BvK supercell, which consists of $n_1 \times n_2 \times n_3$ unit cells, corresponds to a regularly spaced grid of $n_1 \times n_2 \times n_3$ points in the BZ and vice versa. The electron density in the case of the periodic boundary conditions is then computed as:

$$n(r) = \sum_{k} \sum_{n=1}^{N} |\psi_{nk}(r)|^2 \tag{1.51}$$

where N denotes the number of electrons in the primitive cell.

Consequently, Eq. (1.51) requires the calculation of a finite number of one-electron orbitals at a finite number of k-points, taken into account that infinite number of k-points corresponds to an infinitely large BvK supercell. In practice, the electron density is converged with respect to the finite number of k-points [150], which are sampled using, for example, a Monkhorst-Pack scheme [151] – a regularly spaced grid of k-points in the BZ primitive cell.

In FHI-aims [5], the periodic boundary conditions are taken into account by defining the Block-like generalized basis functions $\chi_{ik}(r)$ derived from the real-space atom-centered basis functions $\phi_i(r)$ introduced in Eq. (1.42):

$$\chi_{ik}(r) = \sum_{R(n)} e^{ikR(n)} \phi_i(r - R(l) + R(n)) \tag{1.52}$$

where $\phi_i(r - R(l) - R(n))$ denotes the i-th basis function centered at the l-th atom situated in the n-th unit cell within the BvK supercell. Block-like functions satisfy Bloch's theorem, i.e. $\chi_{ik}(r + R(n)) = e^{ikR(n)} \chi_{ik}(r)$.

The Kohn-Sham eigenfunctions $\psi_{nk}(r)$ are then expressed in terms of the linear combination of these Bloch-like generalized basis functions:

$$\psi_{nk}(r) = \sum_i C_{in}(k)\chi_{ik}(r) = \sum_i C_{in}(k) \sum_{R(n)} e^{ikR(n)}\phi_i(r - R(l) - R(n)) \tag{1.53}$$

Consequently, the matrix elements h_{ij} introduced in Eq. (1.45) become k-dependent:

$$h_{ij}(k) = \langle \chi_{ik} | h^{KS} | \chi_{jk} \rangle \tag{1.54}$$

Summary of the chapter

In this chapter, we formulated the essential concepts used in first-principles calculations based on the DFT framework. We showed how the many-body electron-nuclei problem is decoupled into two separate problems based on the Born-Oppenheimer approximation. Everything in this thesis is done under the assumption that the Born-Oppenheimer approximation is valid. Then we showed how DFT allows to utilize the electronic density for computations and resolve the problems related to the complexity of the N-electron Schrödinger equation. Although DFT is exact, xc-functionals are constructed using a variety of approximations. Some of these xc-functionals (LDA, PBE, PBEsol, HSE06), which are used in this thesis, were briefly discussed or references to detailed explanation of the theory were provided. Finally, we noted that we will use the FHI-aims software package for performing DFT calculations.

Chapter 2

Lattice dynamics

In the previous chapter we assumed that a crystal structure (lattice vectors and positions of atoms forming the basis) is immobile. This allowed us to develop a formalism to calculate the electronic ground state and the total energy of a crystalline system. However, atoms move around their equilibrium positions both at finite temperatures and even at zero temperature (due to the uncertainty principle). Consequently, in this chapter, we focus on the fundamental aspects of lattice and nuclear dynamics modeling [7, 152–154]. In particular, we will discuss the phonon formalism and demonstrate how atomic movement can be treated within the harmonic approximation. Then, we will outline the essentials of *ab initio* molecular dynamics simulations (aiMD) [155, 156] and discuss how to calculate lattice thermal expansion.

2.1 The harmonic approximation

We assume that the Born-Oppenheimer approximation is valid and determines the potential-energy surface $V_{\mathrm{BO}}(R) = E_o^e(R) + V_{nn}(R)$ on which the nuclei move (BO PES). The interaction between electrons and nuclei is completely described by the BO PES. If the crystalline structure is in equilibrium, which we denote as a set of nuclei coordinates $\{R^0\}$, the BO PES approaches a minimum. We are going to consider atomic configurations $\{R\}$ that are very close to the equilibrium configuration $\{R^0\}$. Thus, if atom I is displaced by $U_{I\alpha}$ from the equilibrium position R^0 along the Cartesian direction α, we can write a Taylor expansion of $V_{\mathrm{BO}}(R)$ around the equilibrium configuration:

$$V_{\mathrm{BO}}(R) = V_{\mathrm{BO}}(R^0) + \underbrace{\sum_{I\alpha} \left.\frac{\partial V_{\mathrm{BO}}(R)}{\partial R_{I\alpha}}\right|_{R^0} (R_{I\alpha} - R^0_{I\alpha})}_{=0} + \frac{1}{2} \sum_{I\alpha,J\beta} \underbrace{\left.\frac{\partial^2 V_{\mathrm{BO}}(R)}{\partial R_{I\alpha} \partial R_{J\beta}}\right|_{R^0}}_{\Phi^{\alpha\beta}_{IJ}} (R_{I\alpha} - R^0_{I\alpha})(R_{J\beta} - R^0_{J\beta}) + \mathcal{O}(||R_I - R^0_I||_2^3) + \cdots \quad (2.1)$$

where indices I and J run over the individual atoms, and indices α and β denotes the three Cartesian coordinates. The Hessian $\Phi^{\alpha\beta}_{IJ}$ denotes the interatomic force constant matrix, which represents the response of atom I upon the displacement of atom J. In static equilibrium,

the forces acting on the atoms are zero. Thus, the second term on the right hand side of Eq. (2.1) vanishes.

If the expansion given in Eq. (2.1) is truncated after the second-order term, we obtain the harmonic approximation for the BO PES:

$$V_{\mathrm{BO}}(R) - V_{\mathrm{BO}}(R^0) \approx \frac{1}{2} \sum_{I\alpha, J\beta} \frac{\partial^2 V_{\mathrm{BO}}(R)}{\partial R_{I\alpha} \partial R_{J\beta}} \bigg|_{R^0} U_{I\alpha} U_{J\beta} \tag{2.2}$$

where $U_{I\alpha} = R_I - R_I^0$ is the displacement of atom I from the equilibrium position. To progress further, we need to find out how to calculate the Hessian matrix $\Phi_{IJ}^{\alpha\beta}$, which requires calculations of the forces acting on atoms. The force F_I acting on atom I is given as a derivative of the Born-Oppenheimer potential energy:

$$F_I = -\frac{dV_{\mathrm{BO}}(R)}{dR_I} = \frac{d}{dR_I} \left[E[n(r)] + V_{nn} \right] \tag{2.3}$$

where we used the electronic contribution in terms of the energy functional defined in Eq. (1.25). The derivative of the electronic part with respect to the atomic displacements is:

$$\frac{dE[n(r)]}{dR_I} = \frac{\partial E[n(r)]}{\partial R_I} + \int dr \frac{\delta E[n(r)]}{\delta n(r)} \frac{\partial n(r)}{\partial R_I} \tag{2.4}$$

The first term on the right-hand side of Eq. (2.4) is further transformed taking into account that only the nuclei-electrons interaction depends on R_I:

$$\frac{\partial E[n(r)]}{\partial R_I} = \int dr n(r) \frac{Z_I(R_I - r)}{|R_I - r|^3} \tag{2.5}$$

The second term on the right-hand side of Eq. (2.4) is evaluated using the results of Eq. (1.26):

$$\int dr \frac{\delta E[n(r)]}{\delta n(r)} \frac{\partial n(r)}{\partial R_I} = -\epsilon \frac{d}{dR_I} \int dr n(r) = 0 \tag{2.6}$$

Then, the force F_I is evaluated as:

$$F_I = -\frac{dV_{\mathrm{BO}}(R)}{dR_I} = \int dr n(r) \frac{Z_I(R_I - r)}{|R_I - r|^3} - \sum_{I \neq J} \frac{Z_I Z_J (R_I - R_J)}{|R_I - R_J|^3} \tag{2.7}$$

Therefore, calculations of forces acting on atoms only require knowledge about the electronic density (wave functions) and structural parameters (nuclear charges and lattice parameters). This result is known as the Hellman-Feynman theorem [157, 158]. In FHI-aims forces are calculated analytically, but the utilization of NAOs introduces additional challenges. In particular, so-called Pulay forces [159] appear due to the incompleteness of the basis set. Detailed expressions for all force terms, which appear during calculations with a NAO basis, can be found in [160].

Contrary to interatomic forces, the Hessian matrix $\Phi_{IJ}^{\alpha\beta}$ requires to know the total derivatives of the wave function density, which can be formalized using the 2n+1 theorem [161], which states that the evaluation of the (2n+1)-th derivative of the BO PES requires the knowledge of n-th derivative of the density. This approach is widely used in lattice dynamics calculations performed in the framework of DFPT [51]. However, we use an alternative route, in which the force constants are evaluated numerically by a finite difference approach [162, 163]:

$$\Phi_{I\alpha J\beta} = \frac{\partial^2 V}{\partial R_{I\alpha}\partial R_{J\beta}} = -\frac{\partial F_{I\alpha}(R)}{\partial R_{J\beta}} = -\frac{\partial F_{J\beta}(R)}{\partial R_{I\alpha}} \approx \frac{F_{J\beta}(R_0 + U_{I\alpha}) - F_{J\beta}(R_0)}{U_{I\alpha}} \tag{2.8}$$

This means that the second derivative is obtained by displacing atom I along direction α by a small (≈ 0.01 Å) displacement and by calculating the change in forces from first principles.

The straightforward evaluation of Eq. (2.8) requires $3M$ displacements. However, the problem can be simplified due to the symmetric equivalence of certain displacements. The symmetry of a crystal structure is a crucial factor in practical calculations, because it allows to reduce the amount of calculations. There are numerous programs developed for lattice dynamics calculations, such as Phonopy [164], TDEP [69–71], hiPhive [165], Alamode [166], ShengBTE [167], and many others, which all utilize crystallographic symmetry information to decrease computational costs and potentially eliminate numerical noise. Most of these programs use the spglib [168] package to determine symmetry of the crystal.

Since we have assumed that the nuclei move in the harmonic potential described by Eq. (2.2) and showed how to calculate the forces acting on the atoms, we now can progress with the description of the lattice dynamics. The equation of motion for the I-th atom is given by:

$$M_I \ddot{U}_{I\alpha}(t) = F_{I\alpha} = -\sum_{J\beta} \Phi_{IJ}^{\alpha\beta} U_{J\beta}(t) \tag{2.9}$$

where M_I is the mass of the I-th atoms. Note that the time dependence of the displacement $U_{I\alpha}$ is not explicitly included. To get rid of the time dependence we use the following ansatz:

$$U_{I\alpha}(t) = u_{I\alpha} e^{i\omega t} \tag{2.10}$$

then the ansatz above is inserted into Eq. (2.9) and we obtain:

$$M_I \omega^2 u_{I\alpha} = -\sum_{J\beta} \Phi_{IJ}^{\alpha\beta} u_{J\beta} \tag{2.11}$$

which represents a system of coupled algebraic equations with $3M$ unknowns. The solution can be found by exploiting the periodicity of the crystalline lattice. As was shown in the previous chapter (see Eq. (1.47)), the position $R_{n,l}$ of the l-th atoms in the n-th primitive cell can be written in terms of the Bravais lattice vector $R(n)$, which points to this primitive cell and the vector R_l, which points to the l-th atom in the primitive cell $R_{n,l} = R_n + R_l$. This allows to replace the atomic index I, which runs over all atoms in the solid, by the index pair (n, l) running over the unit cells and the basis atoms. Then, the Hessian reads:

$$\Phi_{IJ}^{\alpha\beta} = \Phi_{lm}^{\alpha\beta}(n, p) \tag{2.12}$$

From the translational invariance of the lattice it follows that:

$$\Phi_{lm}^{\alpha\beta}(n, p) = \Phi_{lm}^{\alpha\beta}(n - p) \tag{2.13}$$

This motivates to search for a solution of $u_{l\alpha}(R(n))$ in terms of traveling harmonic waves of different wave vector q [152].

$$u_{l\alpha}(R(n)) = \frac{1}{\sqrt{M_l}} \epsilon_{l\alpha} e^{iqR(n)} \tag{2.14}$$

where $\epsilon_{l\alpha}$ is the amplitude of the vibration and q denotes the reciprocal wave vector, respectively. Using Eq. (2.11) and Eq. (2.14) we obtain:

$$\omega^2 \epsilon_{l\alpha} = \sum_{m\beta} \sum_{p} \frac{1}{\sqrt{M_l M_m}} \Phi_{l\alpha m\beta}(n-p) e^{iq(R(n)-R(p))} \epsilon_{m\beta} \tag{2.15}$$

We define the dynamical matrix, which is the mass weighted Fourier transform of the force constant matrix, as:

$$D_{lm}^{\alpha\beta}(q) = \frac{1}{\sqrt{M_l M_m}} \sum_{p} \Phi_{lm}^{\alpha\beta}(n-p) e^{iq(R(n)-R(p))} \tag{2.16}$$

Note that the summation is done over p only. Definition of the dynamical matrix allows to write the homogeneous linear system of equations in a compact form:

$$\omega^2 \epsilon_{l\alpha} = \sum_{m\beta} D_{lm}^{\alpha\beta}(q) \epsilon_{m\beta} \tag{2.17}$$

The eigenvalue problem established by Eq. (2.17) has $3M$ eigenvalues $\omega_s(q)$ and eigenvectors $\epsilon_s(q)$, with $s = 1, 2, \ldots, 3M$. The obtained eigenvalues are called phonon frequencies and collectively constitute the phonon dispersion $\omega(q)$. The time-dependent displacement of the atoms is then:

$$U_{I\alpha} = \frac{1}{\sqrt{M_I}} \sum_{q} \sum_{s=1}^{3M} A_{Is}(q) \epsilon_{I\alpha,s}(q) e^{i(qR(n)-\omega_i(q)t)} \tag{2.18}$$

where the amplitude $A_{Is}(q)$ is determined from the initial conditions. Finally, the system of $3M$ coupled equations is transformed to $3M$ decoupled equations. The solutions of these equations correspond to waves, which propagate throughout the crystal and are called normal modes [152]. Thus any arbitrary displacement of atoms from the equilibrium configuration can now be written in the form of normal modes. Moreover, given that Eq. (2.17) describes the nuclear dynamics analytically in the harmonic approximation, we can also calculate the thermodynamic partition function Z as:

$$Z = \prod_{q,s} \frac{\exp\left[-\frac{\hbar\omega_s(q)}{k_B T}\right]}{1 - \exp\left[-\frac{\hbar\omega_s(q)}{k_B T}\right]} \tag{2.19}$$

which allows to calculate thermodynamic quantities such as vibrational free energies or the specific heat [152, 153].

As an example, the phonon dispersion calculated from first principles for MgO is presented in Fig. 2.1(a). The calculations are done with at the DFT-LDA level of theory using FHI-aims package. The dispersion is illustrated for the high-symmetry Γ-X BZ path of the rock salt structure with the $Fm\bar{3}m$ space group. In practice, it is sufficient to present the dispersion for the first BZ, because phonon frequencies have the same periodicity as the reciprocal lattice.

Non-analytical correction

Out of the 3M phonon branches 3 are called *acoustic* and 3M-3 are called *optical*, respectively. In the simulations with supercells and using finite differences approach, optical modes

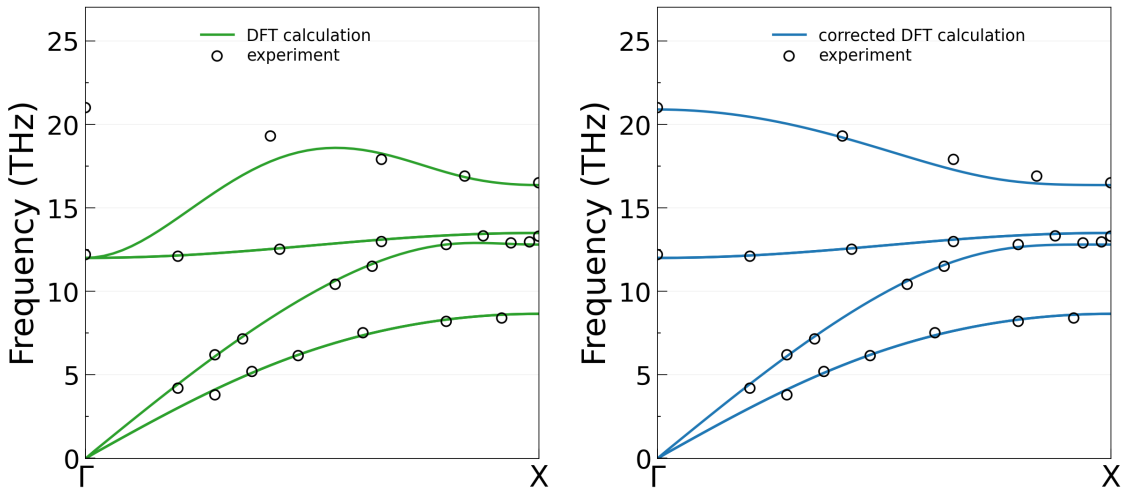

(a) (b)

Figure 2.1: Phonon dispersion in MgO along high-symmetry Γ-X BZ path (a) without NAC correction, (b) with NAC correction. Calculations were done with the LDA xc-functional and 3×3×3 supercell containing 216 atoms. The experimental measurements of the phonon spectrum are done using neutron scattering [169].

are predicted systematically incorrectly, because of the limited simulation cell size and the consequently missing long-range electrostatic effects. The splitting of the longitudinal and the transverse optical modes at the Γ point (LO-TO splitting [9, 170]) is not present (see experimental data in Fig. 2.1(a)). This inconsistency can be resolved by inspecting how a macroscopic electric field influences the lattice dynamics [99] of the crystal and correcting the dynamical matrix with a special contribution, which captures the long-range electrostatic interaction [171]. It can be shown (in the first order approximation) that then the dynamical matrix introduced in the Eq. (2.16) will contain an extra contribution [170, 172]:

$$D_{IJ}^{\alpha\beta}(q \to 0) = D_{IJ}^{\alpha\beta}(q = 0) + \frac{4\pi}{\Omega\sqrt{M_I M_J}} \frac{[qZ_I^*]_\alpha \, [qZ_J^*]_\beta}{q \cdot \epsilon_\infty q} \tag{2.20}$$

where M_I and M_J are the masses of atoms I and J, Ω is the unit cell volume, ϵ_∞ is the high-frequency dielectric tensor, Z^* are the Born Effective Charges, and q denotes the phonon wave vector. Higher order multipolar contributions to NAC can be also calculated [173]. The Z^* formalizes the relationship between the change in polarization upon an atomic displacement [154, 170, 174]:

$$Z_{I\alpha\beta}^* = \frac{\Omega}{e} \frac{\partial P_\alpha}{\partial R_{I\beta}} = \frac{\Omega}{e} \lim_{\Delta R_{I\beta} \to 0} \frac{\Delta P_\alpha}{\Delta R_{I\beta}} \tag{2.21}$$

where ΔP_α is the change in polarization, the index I runs over atoms, the indices α and β denote Cartesian directions, Ω is the unit cell volume, and e is the charge of an electron. Once Z^* and ϵ_∞ are known, the NAC can be applied to obtain the LO-TO splitting [171]:

$$\omega_s^2(q) = \omega_s^2(q = 0) + \frac{4\pi}{\Omega} \cdot \sum_I \frac{|qZ_I^* U_I(q = 0, s)|^2}{q\epsilon_\infty q} \tag{2.22}$$

The approach that leads to Eq. (2.22) is called non-analytical term correction (NAC) and

requires the calculation of the Z^* of each atom in the primitive cell and the ϵ_∞. In FHI-aims, the ϵ_∞ tensor can be computed using DFPT [51] following the formalism presented in [175]. The Z^* tensor is computed using the formalism of the modern theory of polarization [176–178], which itself is based on the Berry-phase theory [179]. In practice, we calculate Z^* by using two-points symmetric finite differences as shown in Eq. (2.21), involving small displacements from the equilibrium position of each symmetrically inequivalent atom in the primitive unit cell. The search for equivalent atom is done using spglib [168] and do not require any visual inspection of the crystal structure. As an example, for MgO we obtained $Z^*_{\mathrm{Mg}} = 1.97$, $Z^*_{\mathrm{O}} = -1.97$, and the high-frequency dielectric tensor is diagonal with all diagonal elements equal to 3.25. The phonon dispersion calculated for MgO with inclusion of the NAC is presented in Fig. 2.1(b). Notably, the NAC correction leads to a better agreement between calculated and experimental data [169], since LO-TO splitting is presented.

Atomic motion in the harmonic approximation

The solution of the Eq. (2.17) yields phonon frequencies and normal modes that can be used to calculate velocities and thermally induced displacements of atoms, consistent with the canonical ensemble. This is done by performing a harmonic normal mode transformation [180]:

$$U_{I\alpha} = \sum_{s=1}^{3M} \epsilon_{I\alpha,s} \langle A_{Is} \rangle \sqrt{-2ln\zeta_1} \sin 2\pi\zeta_2 \tag{2.23}$$

$$\dot{U}_{I\alpha} = \sum_{s=1}^{3M} \epsilon_{I\alpha,s} \omega_s \langle A_{Is} \rangle \sqrt{-2ln\zeta_1} \sin 2\pi\zeta_2 \tag{2.24}$$

where U_I is the displacement of atom I, $\dot{U}_{I\alpha}$ its instantaneous velocity, and ζ_n are uniformly distributed numbers between 0 and 1, which can be transformed to a normal distribution of random numbers using the Box-Muller transform [69]. $\langle A_{Is} \rangle$ is the thermal amplitude of the normal mode s with eigenvector ϵ_{Is} and phonon frequency ω_s [180, 181]:

$$\langle A_{Is} \rangle = \underbrace{\frac{1}{\omega_s}\sqrt{\frac{\hbar\omega_s(n_s+\frac{1}{2})}{M_I}}}_{\text{quantum limit}} \approx \underbrace{\frac{1}{\omega_s}\sqrt{\frac{k_B T}{M_I}}}_{\text{classical limit}} \tag{2.25}$$

where n_s is a Bose-Einstein occupation factor of the mode s, and k_B is a Boltzmann constant. The amplitude of the atomic displacements is taken into account both in classical and quantum limit (note that atomic mass is included into the amplitude definition).

The methodology sketched above allows to generate structures with atomic displacements consistent with the canonical ensemble [70, 182]. Pre-thermalized in such a way, geometries can be used to start aiMD simulations with negligible thermalization time [181] as discussed in the next section. In addition, the temperature influence on a property of interest can be evaluated by averaging the results over an ensemble of such distorted geometries [183, 184].

2.2 Ab initio molecular dynamics

Fully anharmonic calculations of the nuclear dynamics can be done by performing *ab initio* molecular dynamics simulations (aiMD). In this method the motion of atoms is described by Newton's laws, while it is assumed that Born-Oppenheimer approximation is valid (BO aiMD). Forces acting on the atoms are computed via electronic structure theory, for example, DFT. The Hamiltonian and equations of motion for the nuclei reads as:

$$H_n(R,p) = \sum_I \frac{p_I^2}{2M_I} + V_{\mathrm{BO}}(R) \tag{2.26}$$

$$\frac{\partial R_{I\alpha}}{\partial t} = \frac{\partial H_n}{\partial p_{I\alpha}} \tag{2.27}$$

$$\frac{\partial p_{I\alpha}}{\partial t} = -\frac{\partial H_n}{\partial R_{I\alpha}} = -\frac{\partial V_{\mathrm{BO}}(R)}{\partial R_{I\alpha}} = M_I \frac{\partial^2 R_{I\alpha}}{\partial t^2} \tag{2.28}$$

where t denotes the time, p_I and M_I are the moment and mass of the atom I, respectively.

In order to describe the position R_I of atom I at time $t + \Delta t$, we make use of a Taylor series expansion of $R_I(t + \Delta t)$:

$$R_I(t+\Delta t) = R_I(t) + \underbrace{\frac{d}{dt}R_I(t)}_{v_I(t)}\Delta t + \frac{1}{2}\underbrace{\frac{d^2}{dt^2}R_I(t)}_{F_I(t)/M_I}\Delta t^2 + \frac{1}{6}\frac{d^3}{dt^3}R_I(t)\Delta t^3 + \mathcal{O}(t^4) + \cdots \tag{2.29}$$

where $v_I(t)$, M_I, and $F_I(t)$ are the instant velocity of the atom, its mass, and force acting on it, respectively. If the expansion in Eq. (2.29) is truncated after the second-order term and the initial conditions are known (forces, positions, and velocities at $t = 0$), the nuclear dynamics can be calculated. This approach is known as the Euler algorithm [185], but it has inaccuracies, since the error is of the order $\mathcal{O}(t^3)$. In order to increase the accuracy, we can write the backward and forward Taylor expansion $R_I(t \pm \Delta t)$

$$R_I(t \pm \Delta t) = R_I(t) \pm v_I(t)\Delta t + \frac{1}{2}\frac{F_I(t)}{M_I}\Delta t^2 \pm \frac{1}{6}\frac{d^3}{dt^3}\, r(t)\Delta t^3 + \mathcal{O}(t^4) + \cdots \tag{2.30}$$

Truncating the expansions in Eq. (2.30) after the second-order term and summing the results leads to:

$$\begin{aligned} R_I(t+\Delta t) &= 2R_I(t) - R_I(t-\Delta t) + \frac{F_I(t)}{M_I}\Delta t^2 + \mathcal{O}(t^4) \\ &\approx 2R_I(t) - R_I(t-\Delta t) + \frac{F_I(t)}{M_I}\Delta t^2 \end{aligned} \tag{2.31}$$

The Verlet algorithm [186] is based on Eq. (2.31). Higher precision can be obtained by truncating the Taylor expansion in Eq. (2.30) at high-orders. However, then a simulation will become more expensive with just a modest gain in accuracy [187]. The problem of the Verlet algorithm is that the positions of atoms at $t - \Delta t$ are not known for the first time step. This problem can be resolved by utilizing the Velocity-Verlet algorithm [186], in which atomic positions are calculated as in the Euler algorithm and the velocities are obtained as:

$$v_I(t + \Delta(t)) = v_I(t) + \frac{F_I(t+\Delta t) + F_I(t)}{2M_I}\Delta t \tag{2.32}$$

During a aiMD simulation, the nuclei are treated classically at each time step and characterized by a particular nuclear configuration $\{R_1, R_2, \ldots R_M\}$. The electronic density is computed self-consistently, then the forces, acting on the atoms, are evaluated as a negative gradient of the BO PES. The time-evolution of the nuclear dynamics is simulated by propagating the classical equations of motion (Eqs. 2.31, 2.32). aiMD is a real-space method, which requires adopting supercells (periodic repetitions of the primitive cells), in the calculations. This is required by the fact that vibrational wavelenghts of the collective motion of atoms and distances, in which forces between atoms become insignificant (≈10 Å [152]), typically exceed the unit cell size.

Several technical aspects should be carefully taken into account for reliable aiMD simulations. For example, if a too large time step Δt is chosen, the crystalline or molecular structure could just fall apart during the simulation [155]. As a rule of thumb, one tenth of the smallest vibrational period should be chosen. Therefore, a system with heavier atoms can tolerate bigger integration steps, while a system with light atoms requires smaller time steps.

Furthermore, the parameters, used for the electronic structure calculation, determine how accurate the forces estimation is. Thus, the accuracy of the electronic-structure method is of particular importance. If the simulation is not accurate enough, the calculated BO PES will be incorrect and this will lead to a drift of the total energy of the system during the simulation [188]. However, a small drift of the total energy, within few meV, around the average or even slightly away from it, is acceptable, due to the numerical nature of the simulations [155].

The ergodic principle [155] states that if the system is allowed to evolve with time it will explore all possible configurations and a simulation will cover the whole phase space. Then, the ensemble average can be replaces by a time average:

$$\langle O \rangle = \lim_{N \to \infty} \sum_{t=1}^{N} O(t) \tag{2.33}$$

Then, methods of statistical mechanics allows to extract information about physical observable from the aiMD simulation. Since classical aiMD utilize Newton's laws, the energy and momentum of a system are conserved, which defines the microcanonical ensemble simulation (NVE – constant number of particles, volume of the system, and total energy). In order to simulate ensembles other than the microcanonical, the system must be brought into contact with a so-called reservoir (a thermostat or a barostat). If thermodynamical variables such as temperature or pressure are fixed, aiMD samples represent the canonical ensemble (NVT) or the isothermal-isobaric ensemble (NPT), respectively. At finite temperatures, the physical observable can be calculated by averaging over an ensemble.

Modeling of the canonical ensemble

To perform a simulation of the canonical ensemble (simulation at temperature T, where the number of particles and volume of the system are kept constant), one should have control over the temperature. The equipartition theorem is valid for the canonical ensemble, which

means that the kinetic energy is equally distributed over all degrees of freedom of the system. Thus, velocities (or momenta) of atoms obey the Maxwell-Boltzmann distribution:

$$f(p_I) = \left(\frac{1}{2\pi M_I k_B T}\right)^{\frac{3}{2}} \exp\left[-\frac{p_I^2}{2M_I k_B T}\right] \tag{2.34}$$

Since the temperature depends on the kinetic energy ($E_{kin} = \frac{3}{2}Nk_BT$) and the kinetic energy depends on the velocities of each atom, the temperature is not constant, as that would mean fixing the kinetic energy. However, the temperature of a system, averaged over the time, has a fixed value. Consequently, simulations should run for a sufficient amount of time to thermalize and equilibrate the system at a particular temperature.

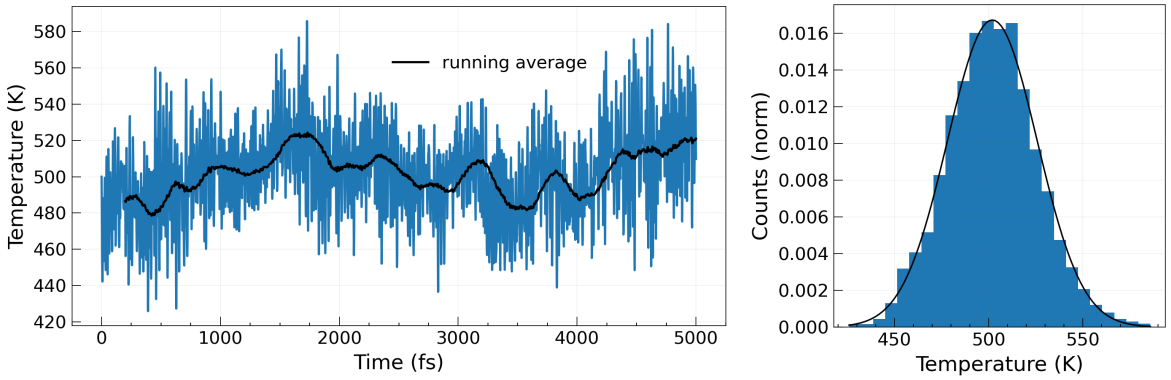

(a) (b)

Figure 2.2: The canonical ensemble aiMD (NVT) simulation of diamond at T=500 K. (a) Temperature at each time step of the simulations with its running average taken over 200 steps. (b) The temperature distribution among samples, with the Gaussian function lineshape.

Computationally, the temperature is controlled by bringing the system into contact with a heat bath – a thermostat. A variety of different thermostats exists [189]. In this thesis we utilize the Langevin thermostat, in which the temperature influence is modeled by coupling each atom to a heat bath through a fluctuating force and a friction term. The motivation behind the Langevin thermostat is based on the hypothesis that once particles move in the solvent represented by another particles, the later induce a damping force on the former, which mimics a change in temperature. The force, acting on atom I, is then:

$$\frac{dp_I}{dt} = F_I - \gamma p_I + \sqrt{2M_I k_B \gamma T}\nu(T) \tag{2.35}$$

where p_I, F_I, and M_I are the momentum of atom I, the force acting on that atom, and its mass, respectively. Two parameters – γ and $\nu(T)$ denote the friction and the white-noise terms [190].

In summary, aiMD represents an accurate way to calculate fully anharmonically the nuclear dynamics. The ensemble average for the property of interest, must be converged with respect to the trajectory length. The cost of simulations comes from (i) the simulations with relatively large supercells (hundreds of atoms), (ii) a necessity to compute the electronic ground state at every time step of simulation, and (iii) simulations should be performed for

sufficiently long time so that the aiMD trajectory will cover the phase space of the system. We should also note that in some systems, the quantum nature of the nuclei can play a significant role in the description of materials properties [191–193]. For example, simulations of ice and water require a quantum mechanical treatment of the nuclear dynamics [194, 195]. Such simulations can be performed using path-integral molecular dynamics [192, 196]. These effects are particularly important for light atoms and especially at low temperatures. At high temperature, the anharmonic nature of vibrations dominates over quantum effects. As will be shown later, this thesis is focused on temperatures, where quantum nuclear effects lose their impact. Thus, nuclear quantum effects will not be considered.

2.3 Anharmonicity quantification

Materials with substantially anharmonic lattice dynamics are not rare [11, 68]. With growing temperature, the anharmonicity of the PES becomes more and more noticeable. To inspect anharmonic contributions to the lattice dynamics, we can split the full potential energy $\mathrm{V_{BO}}$ into the harmonic contribution V^{HA} and a term that captures the anharmonicity of the PES V^{A}:

$$V_{\mathrm{BO}} = V^{HA} + V^{A} \tag{2.36}$$

Consequently, we can also split the interatomic forces. For example the total force acting on atom I is:

$$F_I = -\frac{\partial V_{\mathrm{BO}}}{\partial R_I} = F_I^{HA} + F_I^{A} \tag{2.37}$$

Therefore, information about anhamonicity is stored in the forces. To quantify the amount of anharmonicity authors of [68] introduced a so-called anharmonicity measure, which can be defined at finite temperatures as:

$$\sigma^{A}(T) = \sqrt{\frac{\sum_{I\alpha}\langle (F_{I\alpha}^{A})^2\rangle_T}{\sum_{I\alpha}\langle (F_{I\alpha})^2\rangle_T}} \tag{2.38}$$

Here, $\langle\cdot\rangle_T$ denotes the thermodynamic ensemble average evaluated at temperature T. The ability of Eq. (2.38) to distinguish harmonic and anharmonic materials is discussed in detail in [68, 197].

The evaluation of the total force F_I in Eq. (2.38) can be done by performing aiMD simulations. Alternatively, one can utilize high-order force constants obtained by truncating the Taylor series introduced in Eq. (2.1) at the terms following the harmonic term. Commonly, such an approach truncates the series at the third order term, since inclusion of higher-order force constants becomes computationally prohibitively demanding [167, 198]. Higher-order force constants can also be obtained by fitting to the anharmonic force constants obtained by sampling the anharmonic PES at finite temperatures as it is done in the self-consistent phonon theory SSCHA [166, 199–201] or temperature-dependent effective potential method TDEP [69–71].

2.4 Lattice thermal expansion

The nuclear motion also causes an increase of the dynamical pressure, which can results in the expansion of the the lattice. This effect is not accounted in the harmonic approximation. In the harmonic approximation, dynamics of a lattice is completely determined by the dynamical matrix D_{IJ} (see Eq. 2.16) and the Hamiltonian of the system does not depend on the lattice parameters. Consequently, the lattice expansion coefficient vanishes in the harmonic approximation [9, 152]. However, it is possible to calculate the lattice thermal expansion in the quasi-harmonic approximation (QHA) [152–154]. In the QHA, phonon frequencies are volume-dependent and it is assumed that for each crystalline volume, the harmonic approximation holds, i.e., the temperature dependence of the phonon frequencies is defined as the temperature dependence of the volume $\omega(V,T) \approx \omega(V(T))$. At finite temperatures, the equilibrium lattice parameters correspond to the minimum of the Gibbs free energy G, which contains the Helmholtz free energy term and pV term. The Helmholtz free energy H is determined as:

$$H(T,V) = E_{\text{lat}}(V) + E_{\text{vib}}(T,V) - TS(T,V) \tag{2.39}$$

where $E_{\text{lat}}(V)$ is the total energy of the lattice, which can be computed using the DFT framework, $E_{\text{vib}}(T,V)$ is the vibrational energy of the lattice (phonons), and $S(T,V)$ is the entropy associated with the vibrations. The vibrational energy is determined using the partition function written in Eq. (2.19) as [152]:

$$E_{\text{vib}}(T,V) = -k_{\text{B}}T \ln Z = \frac{1}{N}\sum_{lq}\left[\frac{1}{2} + n_{lq}(T,V)\right]\hbar\omega_{lq}(V) \tag{2.40}$$

where N is the number of terms in the sum, n_{lq} is the Bose-Einstein factor, and ω_{lq} is the frequency of the phonon with wave vector q in the l-th band. The entropy term can be calculated by taking the partial derivative of the Helmholtz free energy with respect to the temperature at fixed volume:

$$S = \left(\frac{\partial H}{\partial T}\right)_V = -\frac{1}{N}\sum_{lq} k_{\text{B}} \ln\left[1 - \exp\left(-\frac{\hbar\omega_{lq}(V)}{k_{\text{B}}T}\right)\right] + \frac{1}{NT}\sum_{lq}\frac{\hbar\omega_{lq}(V)}{\exp\left(-\frac{\hbar\omega_{lq}(V)}{k_{\text{B}}T}\right) - 1} \tag{2.41}$$

The temperature dependence of the volume is then computed by minimizing the Gibbs free energy for a particular finite temperature T and pressure p:

$$G(T,p) = \min_{\text{V}}\left[E_{\text{lat}}(V) + E_{\text{vib}}(T,V) - TS(T,V) + pV\right] \tag{2.42}$$

Fitting of $G(V)$ (or equivalently $H(V)$ at zero pressure) with the Birch-Murnaghan equation of state [202, 203] allows to obtain the temperature-dependent equilibrium lattice parameters [204]. As an example, Fig. 2.3(a) shows the Helmholtz free energy for different volumes and different temperatures in GaAs. Fig. 2.3(b) shows the temperature dependence of the volume in GaAs.

In the case of aiMD simulations of the canonical ensemble (NVT) the LTE can be taken into account by computing the thermodynamic average of the stress tensor observed along

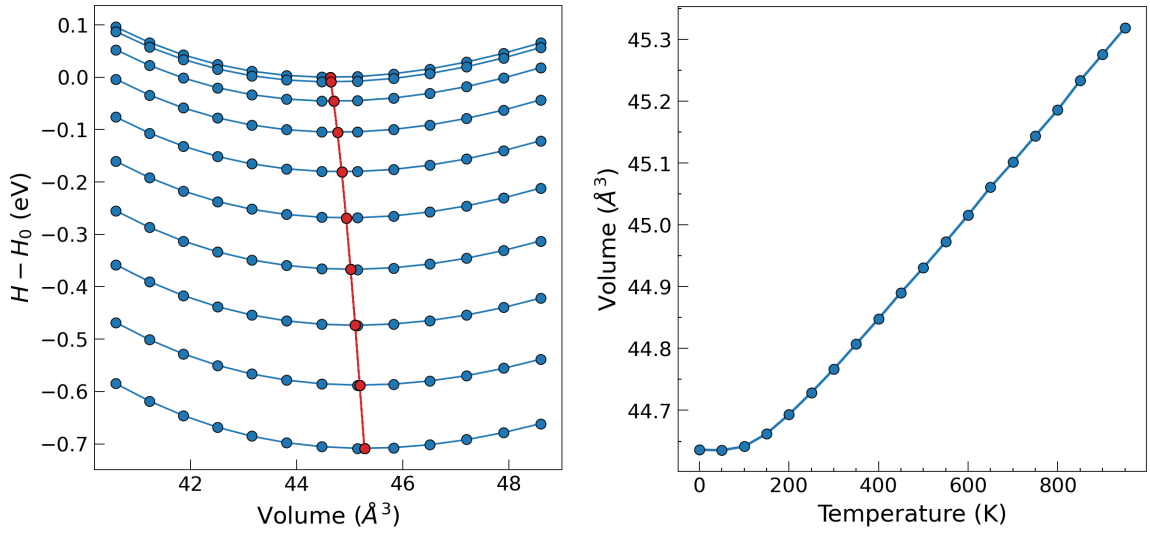

(a) (b)

Figure 2.3: (a) Helmholtz free energy H for GaAs as a function of volume at different temperatures (from 0 K to 1000 K). (b) Temperature dependence of the unit cell volume of GaAs.

the aiMD trajectory [68, 85]. This stress tensor allows to estimate the internal pressure and then re-optimize the structure under this internal pressure to obtain thermally expanded geometries.

The thermodynamic pressure at a given crystal volume V and temperature T is:

$$p(V,T) = \frac{Nk_{\mathrm{B}}T}{V} + p_{\mathrm{pot}}(V_0,T) + p_{\mathrm{int}}(V) \tag{2.43}$$

Here V_0 denotes the volume at static equilibrium. The first term in Eq. (2.43) represents a kinetic pressure, the second one is a potential pressure, and the last term is the internal pressure, which is induced by the lattice renormalization at finite temperatures in the NVT simulations. Thus, aiMD simulations at the equilibrium volume and the temperature of interest should be performed for sufficiently long time, so that the potential pressure is converged. The internal pressure is then calculated based on the assumption that it is not dependent on the temperature and can be obtained from the mechanical characteristics of the lattice at zero temperature. This is achieved by calculating the $p(V)$ dependence, which is then parameterized by the Vinet equation of state [205]:

$$p_{int} = \frac{3B_0}{X^2}(1-X)e^{\nu(1-X)} \text{ with } X = \left[\frac{V}{V_0}\right]^{1/3} \text{ and } \nu = \frac{3}{2}\left(B_0' - 1\right) \tag{2.44}$$

where B_0 is the bulk modulus, and $B_0' = \partial B_0/\partial p$ is the isothermal pressure derivative of the bulk modulus. As it was mentioned above, we assume that these parameters are obtained for the static lattice in equilibrium and any temperature dependence in neglected.

Once we obtained the parameterization (V_0, B_0, B_0') by fitting the Vinet equation of state, the temperature-dependent volume $V_{\mathrm{min}}(T)$ is found by asserting zero pressure at equilibrium. The resulting internal pressure p_{int} can be used to find the static reference lattice at finite

temperature $L(T)$ by optimizing the geometry with applied external pressure during relaxation $p_{\text{relaxation}} = -p_{\text{int}}(V_{\text{min}})$. The static lattice obtained in this way will then generate a static pressure contribution, which will compensate the pressure appearing in the aiMD NVT simulation. Once the new lattice is obtained, it should be verified that it indeed leads to a negligible pressure during NVT simulations. If a significant deviation still exists, the procedure should be repeated until self-consistency is achieved.

Summary of the chapter

In this chapter, we introduced essentials of the lattice dynamics theory. We discussed the harmonic approximation, the phonons formalism, and showed how to account for polar effects using NAC. We also introduced the stochastic sampling approach, which can be used to describe the atomic movement in the harmonic approximation. We established the essentials of the aiMD, which allows to perform fully anharmonic calculations of the nuclear motion. Finally, we showed how to calculate LTE in the QHA and in aiMD simulations.

Chapter 3

The temperature dependence of electronic states

In this chapter, we will discuss how electron-phonon interactions (EPI) influence the band gap of semiconductors and insulators at finite temperatures [7–9,56]. We will evaluate two distinct contributions: the role of the nuclear motion and the role of the lattice thermal expansion (LTE) [12, 206, 207]. The nuclear motions influence on the band structure renormalization can be observed already at zero temperature. The zero-point motion of atoms, governed by the uncertainty principle, leads to a zero-point shift of the band structure. The zero-point renormalization (ZPR) of the band gap can be substantial, for example, in diamond it is ≈370 meV [12, 207], while the total band gap of diamond is 5.47 [208] eV.

Nowadays, the Allen-Heine-Cardona (AHC) formalism [57, 58] is the most widely used method to investigate the band gap renormalization [17, 18, 22, 41, 52]. In this chapter, we will review the main aspects of the AHC formalism with its benefits and limitations. Then, we will discuss how to overcome some of these limitations by means of aiMD simulations and the band structure unfolding technique [85]. We will also discuss how to calculate the influence of LTE on band structure changes and how to account for the influence of long-range electrostatic effects [40, 42, 43, 93, 209].

3.1 Influence of the nuclear motion

The influence of atomic motion on electronic eigenstates can be demonstrated using diatomic molecules such as H_2 or CO.[1] These diatomic molecules have six vibrational modes, which can be divided into three translational, two rotational, and one stretch mode. Only the stretch mode affects the renormalization of electronic eigenstates. For demonstration purposes, we calculated the highest occupied molecular orbital (HOMO) of both molecules as a function of the interatomic distance. The dependence of HOMO on bond length is shown in Fig. 3.1.

A theoretical formulation of the band gap renormalization under finite temperatures can be started assuming that the Born-Oppenheimer approximation is valid. Then, for a given set of atomic coordinates $R = \{R_1, R_2, \cdots, R_M\}$, the electronic Scrödinger equation $\hat{H}_e^R |\Psi_n^R\rangle =$

[1] This demonstration is inspired by a study on the effect of zero-point motion on the valence band bandwidth in ^{3}He [210] and the lecture of X. Gonze, given in the EPW school in 2018.

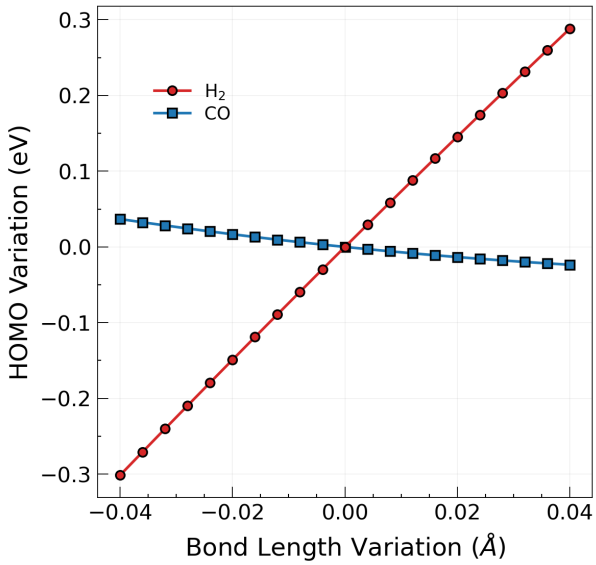

Figure 3.1: Variation of the highest occupied molecular orbital (HOMO) with the distance between atoms in the hydrogen molecule H_2 (red disks) and the carbon monoxide CO (blue squares).

$\epsilon_n^R |\Psi_n^R\rangle$ is solved to obtain the energies ϵ_n^R of the electronic states $|\Psi_n^R\rangle$. Subscript n denotes simultaneously the band index and the crystal-momentum. The temperature dependence of ϵ_n^R is evaluated using the canonical ensemble average at temperature T:

$$\langle \epsilon_n^R \rangle_T = \frac{1}{Z} \int dR d\mathbf{p} \exp\left(\frac{-E(R,\mathbf{p})}{k_B T}\right) \epsilon_n^R \tag{3.1}$$

where R and $\mathbf{p}$ are positions and momenta of the nuclei, k_B is the Boltzmann constant, $Z = \int dR d\mathbf{p} \exp\left[-E(R,\mathbf{p})/k_B T\right]$ is the canonical partition function, and $E(R,\mathbf{p})$ is the total energy. Vibrations in crystals consist of a combination of different normal modes, leading to fluctuations in electronic eigenstates around their equilibrium positions. At finite temperatures, electronic states shift and spread due to the scattering, which determines finite lifetime of the electrons and holes at finite temperatures [8].

Allen-Heine-Cardona formalism

In practice, the most widely adopted approach to evaluate Eq. (3.1), in the scope of first principles calculations, is the AHC formalism [57, 58]. This formalism allows to find an approximate solution to Eq. (3.1) by utilizing two approximations based on the perturbation theory, namely: (i) the dependence of the electronic eigenstates on the nuclear motion is truncated up to the second order in the atomic displacements and (ii) the harmonic approximation is used for the lattice dynamics description. The latter approximation allows to simplify the problem introduced in Eq. (3.1) as $\langle \epsilon_{nk}^R \rangle_T \approx \langle \epsilon_{nk}^R \rangle_T^{\text{ha}}$:

$$\langle \epsilon_n^R \rangle_T^{\text{ha}} = \frac{1}{Z^{\text{ha}}} \int dR^{\text{ha}} d\mathbf{p}^{\text{ha}} \exp\left(\frac{-E^{\text{ha}}(R^{\text{ha}},\mathbf{p}^{\text{ha}})}{k_B T}\right) \epsilon_n^R \tag{3.2}$$

Once the dependence of the electronic states on the nuclear motion is truncated up to the second order in nuclear displacements $\mathbf{U} = R - R^0$ from the equilibrium positions R^0, one obtains further simplification $\langle \epsilon_{nk}^{R} \rangle_T^{\mathrm{ha}} \approx \langle \epsilon_{nk}^{\mathrm{pt},R} \rangle_T^{\mathrm{ha}}$. Consequently, the T-dependence of the electronic states in the AHC formalism reads as:

$$\langle \epsilon_{n}^{\mathrm{pt},R} \rangle_T^{\mathrm{ha}} = \frac{1}{Z^{\mathrm{ha}}} \int dR^{\mathrm{ha}} d\mathbf{p}^{\mathrm{ha}} \exp\left(\frac{-E^{\mathrm{ha}}(R^{\mathrm{ha}}, \mathbf{p}^{\mathrm{ha}})}{k_{\mathrm{B}} T} \right) \epsilon_{n}^{\mathrm{pt},R} \tag{3.3}$$

The combination of the two approximations mentioned above leads to the evaluation of Eq. (3.3) in the AHC formalism [57, 58] as:

$$\begin{aligned} \langle \epsilon_{n}^{\mathrm{pt},R} \rangle_T &= \epsilon_{nk}^{\mathrm{eq}} + \\ &+ \underbrace{\frac{1}{2} \sum_{IJ} \langle \Psi_n^{\mathrm{eq}} | \partial_{IJ}^2 \hat{H}_e^{\mathrm{eq}} | \Psi_n^{\mathrm{eq}} \rangle \, U_I U_J}_{\text{Debye-Waller term}} + \underbrace{\sum_{IJ} \sum_{n'}{}' \frac{\langle \Psi_n^{\mathrm{eq}} | \partial_I \hat{H}_e^{\mathrm{eq}} | \Psi_{n'}^{\mathrm{eq}} \rangle \, \langle \Psi_{n'}^{\mathrm{eq}} | \partial_J \hat{H}_e^{\mathrm{eq}} | \Psi_n^{\mathrm{eq}} \rangle}{\epsilon_n - \epsilon_{n'}} U_I U_J}_{\text{Fan-Migdal term}} \end{aligned} \tag{3.4}$$

where the prime on the summation indicates that the index $(n') = (n)$ is omitted, and superscript "eq" indicates that the electronic states $|\Psi_n^{\mathrm{eq}}\rangle$ and $|\Psi_{n'}^{\mathrm{eq}}\rangle$ are evaluated for the structure in equilibrium geometry. The second and third terms in the Eq. 3.4 are called the Debye-Waller term and Fan-Migdal term, respectively [53–55,57]. The AHC formalism allows to perform evaluation of the phase-space integrals in Eq. (3.1) as shown in [15,39,52,211,212]. It should be also noted that derivations above are done in the adiabatic approximation, while the non-adiabatic derivation was presented and benchmarked only recently [213].

Methodology and technical details of the calculations based on the AHC formalism are widely described in literature [10, 60, 61] and the method is widely and successfully applied [12–19,21,22,52,94,182,207,213–216]. We also note that for strongly correlated materials calculations of EPI can be done using DFT+U formalism [217–219] (and its linear-response extension DFPT+U [220]). Furthermore, the inclusion of the many-body effects can be done using post-DFT methods such as GW [221, 222] as was shown, for example, in [223–225].

Despite the success of the AHC formalism, the methodology is not suited to straightforwardly treat highly anharmonic materials, because in such systems nuclear movement cannot be accurately approximated by a harmonic potential. Typically, soft modes presented in highly-anharmonic materials are either removed from the calculations or anharmonicity can be treated using approaches such as SSCHA [72] or TDEP [69, 70]. Usage of the anharmonic phonon modes were shown to be vital to describe the temperature-dependent band gap renormalization in $SrTiO_3$ [76].

Fully anharmonic non-perturbative approach to the band gap renormalization evaluation due to the nuclear motion

An alternative approach, which allows to treat both harmonic and anharmonic materials on equal footing, was recently introduced in [85]. In principle, Eq. (3.1) can be evaluated based on aiMD simulations [79, 85, 91, 226–229], which allows to completely account for the anharmonicity of the BO PES. In this approach, aiMD trajectories with length τ are used to evaluate the canonical ensemble average in Eq. (3.1) as a time t average:

$$\langle \epsilon^R_{nk} \rangle_T = \langle \epsilon^R_{nk} \rangle^{\mathrm{aiMD}}_T = \lim_{\tau\to\infty} \frac{1}{\tau} \int_0^\tau \epsilon^{\mathbf{R(t)}}_{nk} dt \tag{3.5}$$

The evaluation of Eq. (3.5) is assumed to be accurate above the Debye temperature. For the materials in which the nuclear quantum effects are important [191–193, 230], one can utilize *ab initio* path-integral MD [196]. Though aiMD can be used to evaluate the canonical ensemble average in Eq. (3.1), it also limits the straightforward analysis of the state and momentum resolved properties. This problem is related to the usage of the supercells during aiMD calculations, which cause mixing of electronic states, since the supercell BZ (SCBZ) is smaller than the primitive cell BZ (PCBZ) and folding of states occurs [80, 81, 83]. Because of the band-folding the evaluation of the band gap renormalization was usually done by calculating the electronic density of states, with subsequent estimation of the edge gap [182, 228]. Recently, it was demonstrated [85] that the combination of aiMD simulations can be used with band-unfolding technique [80, 81, 83, 231] to obtain the temperature-dependent momentum-resolved spectral functions. Thus, band-unfolding allows to identify state- and momentum-resolved band structures quantities such as band gaps and lifetimes of electrons and holes.

In practice, the workflow starts with the calculation of the electronic energies $\epsilon^{R(\mathrm{t})}_n$ and the electronic states $\Psi^{R(\mathrm{t})}_n$ at each aiMD step characterized by particular nuclear configuration $\{R(\mathrm{t})\}$. Then the electronic states $\Psi^{R(\mathrm{t})}_n$ are expanded in terms of the equilibrium states $|\Psi^{\mathrm{eq}}_l\rangle$ obtained for the equilibrium nuclear configuration (R^0):

$$|\Psi^{R(\mathrm{t})}_n\rangle = \sum_m p^{\mathrm{R(t)}}_{mn} |\Psi^{\mathrm{eq}}_l\rangle\,,\ p^{\mathrm{R(t)}}_{mn} = \langle \Psi^{\mathrm{eq}}_l | \Psi^{R(\mathrm{t})}_n \rangle \tag{3.6}$$

Disentangling of the eigenenergies calculated during the aiMD simulation with the supercell requires unfolding the states from the SZBZ to the PCBZ. This is done based on the unfolding technique [80, 83, 231–236]. As was shown in [81, 85], the expansion coefficients introduced in Eq. (3.6) can be used to recover the band structure in the PCBZ. This is done by calculating the spectral function expressed in the Lehman representation [81]:

$$A^{R(\mathrm{t})}_{nk}(\epsilon) = \sum_{NK} |p^{R(\mathrm{t})}_{nk,NK}|^2 \delta(\epsilon - \epsilon^{R(\mathrm{t})}_{NK}) \tag{3.7}$$

If Eq. (3.7) is evaluated for each nuclear configuration $\{R(\mathrm{t})\}$ of the aiMD simulation, one can obtain the momentum-resolved spectral function by summing over band indices n:

$$A^{R(\mathrm{t})}_{k}(\epsilon) = \sum_{NK} \sum_n |p^{R(\mathrm{t})}_{nk,NK}|^2 \delta(\epsilon - \epsilon^{R(\mathrm{t})}_{NK}) \tag{3.8}$$

Then the momentum-resolved spectral function at finite temperature $\langle A^{R(\mathrm{t})}_k(\epsilon)\rangle_{\mathrm{T}}$ is obtained by performing thermodynamic averaging of $A^{R(\mathrm{t})}_k(\epsilon)$ along the aiMD trajectory. Therefore, combination of the canonical ensemble sampling technique,(it can be either aiMD or stochastic sampling [180]) allows to compare calculated $\langle A^{R(\mathrm{t})}_k(\epsilon)\rangle_{\mathrm{T}}$ with angle-resolved photoemission spectroscopy experiments [237]. A

Brillouin Zone folding and unfolding

In order to account for all vibrational modes which contribute to the specific quantity of interest aiMD simulations require utilization of a supercell (SC). A SC represents a simulation cell which is constructed from multiple numbers of primitive cells (PC). The lattice vectors A of the SC are related to the PC lattice vectors a through the transformation matrix:

$$\begin{pmatrix} A_x \\ A_y \\ A_z \end{pmatrix} = \begin{pmatrix} M_{11} & M_{12} & M_{13} \\ M_{21} & M_{22} & M_{23} \\ M_{31} & M_{32} & M_{33} \end{pmatrix} \begin{pmatrix} a_x \\ a_y \\ a_z \end{pmatrix} \tag{3.9}$$

or in shorter form:

$$A_i = \sum_j M_{ij} a_j \tag{3.10}$$

where M_{ij} are the integer elements of the transformation matrix M. Since the SC is an exact repetition of the reference PC and taken into account that no defects were introduced in the SC, the positions of atoms in the SC and PC are mapped to each other unambiguously by the transformation matrix M.

The reciprocal lattice is generated by the reciprocal lattice vectors b, in a way that $a_i \cdot b_i = 2\pi\delta_{ij}$:

$$\begin{pmatrix} b_x \\ b_y \\ b_z \end{pmatrix} = 2\pi \begin{pmatrix} a_x \\ a_y \\ a_z \end{pmatrix}^{-T} \tag{3.11}$$

and the reciprocal lattice of the SC is simulated similarly by utilizing reciprocal lattice vectors of the SC B. Taken into account the connection between SC and PC Eq. (3.10), the reciprocal lattice vectors of the SC are related to the reciprocal lattice vectors of the PC via:

$$\begin{pmatrix} B_x \\ B_y \\ B_z \end{pmatrix} = \begin{pmatrix} \bar{M}_{11} & \bar{M}_{12} & \bar{M}_{13} \\ \bar{M}_{21} & \bar{M}_{22} & \bar{M}_{23} \\ \bar{M}_{31} & \bar{M}_{32} & \bar{M}_{33} \end{pmatrix} \begin{pmatrix} b_x \\ b_y \\ b_z \end{pmatrix} \tag{3.12}$$

or in a shorter form:

$$B_i = \sum_j (M^T)^{-1}_{ij} b_j \tag{3.13}$$

where M^T is the transposed matrix M and $(M^T)^{-1}$ its inverse.

Consequently, an arbitrary K point of the SC reciprocal lattice is related to the PC k point through the transformation matrix M:

$$\begin{pmatrix} K_x \\ K_y \\ K_z \end{pmatrix} = \begin{pmatrix} M_{11} & M_{12} & M_{13} \\ M_{21} & M_{22} & M_{23} \\ M_{31} & M_{32} & M_{33} \end{pmatrix} \begin{pmatrix} k_x \\ k_y \\ k_z \end{pmatrix} \tag{3.14}$$

The reciprocal lattice vectors have the form $G = \sum_i m_i B_i$ for the SC and $g = \sum_i n_i b_i$ for the PC. There are exactly $N = \det(M) = V_{SC}/V_{PC}$ (V_{SC} and V_{PC} are volumes of the SC and PC) distinct PC translations that generate the SC from the PC. If SC is constructed

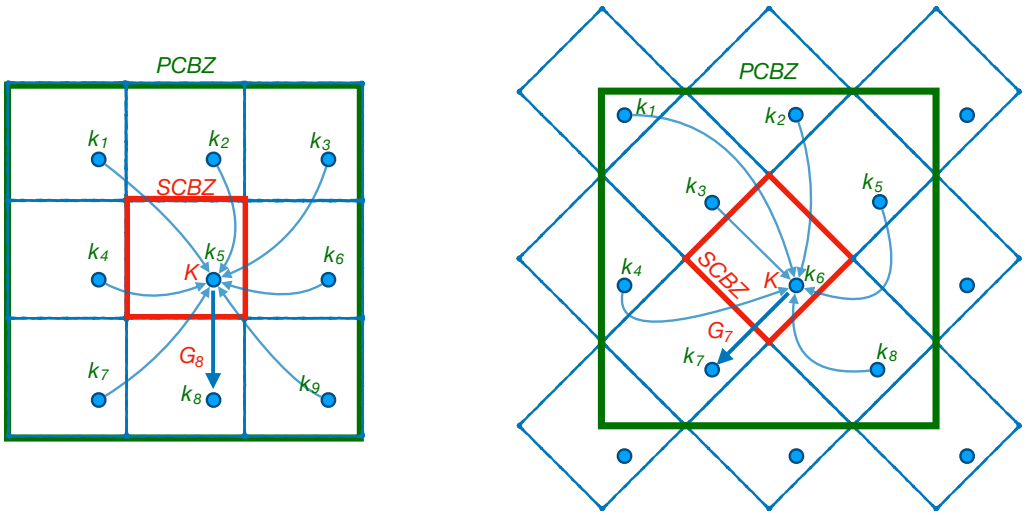

(a) (b)

Figure 3.2: Schematic presentation of the BZ folding, which demonstrates the relations between k vectors of the PC, K vector of the SC and reciprocal lattice vectors of the SC G for a two-dimensional (a) 3×3 and (b) $2\sqrt{2} \times 2\sqrt{2}$ SC. PCBZ is drawn in green, SCBZ is drawn in red. Arrows represent the folding of different k_i of the PCBZ into one K of the SCBZ. The reciprocal lattice vector G_i shows the unfolding of K into k_i.

from the N PCs there are exactly N reciprocal lattice vectors G_i. For a given vector k in the PCBZ there is only one K in the SCBZ to which it folds and two vectors are connected by a reciprocal lattice vector G_i of the SCBZ, such as $k_i = K + G_i$. For each K from the SCBZ there are exactly N PCBZ vectors k as demonstrated in Fig. 3.2(a, b).

Let $O^{PC}(k)$ and $O^{SC}(K)$ denote expectation values of some k-sensitive observable $\hat{O}$ in the PC and SC, respectively. Then for the PC and SC we can write:

$$O^{PC}(k+g) = \langle \Psi^{PC}_{k+g} | O | \Psi^{PC}_{k+g} \rangle = \langle \Psi^{PC}_{k} | O | \Psi^{PC}_{k} \rangle = O^{PC}(k) \tag{3.15}$$

$$O^{SC}(K+G) = \langle \Psi^{SC}_{K+G} | O | \Psi^{SC}_{K+G} \rangle = \langle \Psi^{SC}_{K} | O | \Psi^{PC}_{K} \rangle = O^{SC}(K) \tag{3.16}$$

where g and G are PC and SC reciprocal lattice vectors and we have used the periodicity of the wave functions Ψ^{PC} and Ψ^{SC} defined for the PC and SC. The connection between SC and BC established in Eq. (3.10) states that any translation of the PCBZ is also a valid translation of the SCBZ. Which leads to:

$$O^{SC}(K+g) = O^{SC}(K) \tag{3.17}$$

Consequently, expectation values $O^{PC}(k)$ and $O^{SC}(K)$ are periodic in the PC reciprocal lattice and in addition, the usage of the SC introduces an additional periodicity [238]. If $\hat{O}$ is a Kohn-Sham Hamiltonian, one can illustrate the folding of the electronic eigenstates (see Fig. 3.3). Obviously, the folding of the electronic eigenstates limits the analysis of the band structure-related properties.

Another important observation we have to discuss before we progress to the actual unfolding procedure is related to the connection between the supercell wave functions and the

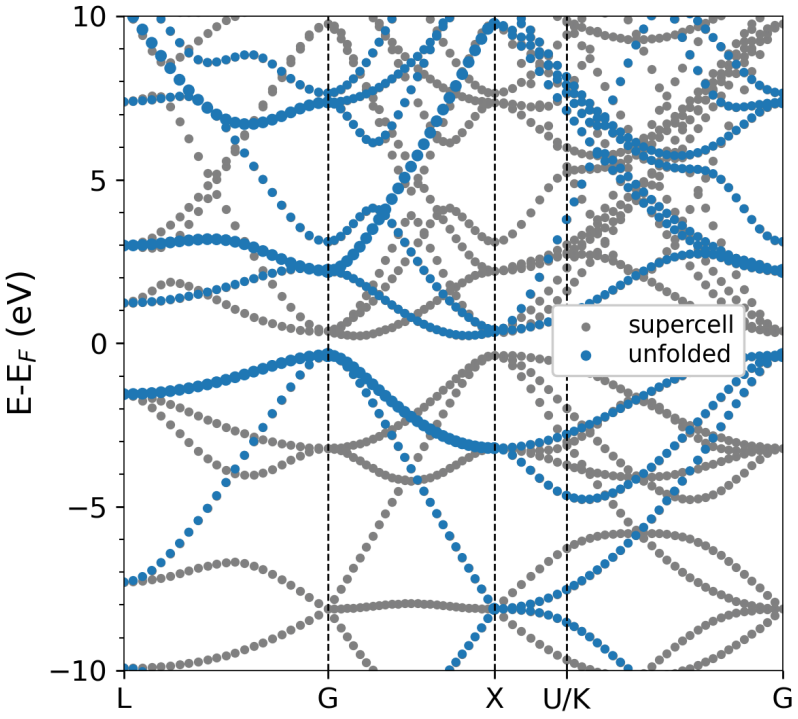

Figure 3.3: Folded (grey) and unfolded (blue) band structures of silicon calculated using conventional cubic cell with 8 atoms. The unfolded bands reproduce the band structure of the primitive unit cell of silicon. High-symmetry BZ path is used for demonstration.

unit cell wave functions. Suppose we have a wave function of the supercell Ψ_K with Block symmetry of the supercell: $\Psi_K(x+R) = e^{iKR}\Psi_K(x)$. Then we define a projection operator $\hat{P}(K)$ as [83, 239]:

$$\hat{P}(K \to +G) = \frac{1}{N}\sum_{i=1}^{N} \hat{T}(r_i) e^{-i(K+G)r_i} \tag{3.18}$$

where $\hat{T}(r_i)$ is the translation operator $\hat{T}(r_i)f(x) = f(x+r_i)$. The projection operator is periodic and idempotent.

Once $\hat{T}(R_i)$ acts on the SC wave function Ψ_{KJ} it determines its Bloch property, $\hat{T}(R_i)\Psi_{KJ} = e^{iKR}\Psi_{KJ}$. The similar expression is obtained when $\hat{T}(r_i)$ acts on the PC wave function. In the unfolding procedure the projection operator $\hat{P}(K \to K+G)$ operates on the SC Bloch function Ψ_K and "projects out" the component that has the Bloch symmetry of the PC. The ability of the projection operator to extract PC Bloch character from the SC wave function can be demonstrated by first applying the projection operator on the test supercell wave-function Ψ_K and by then using the translation operator $\hat{T}(r_i)$ to examine the PC Bloch character:

$$\hat{T}(r_i)\hat{P}(K \to K+G)\Phi_K = \\ \frac{e^{i(K+G)r_j}}{N}\sum_{j=1}^{N} \hat{T}(r_i+r_j)e^{-i(K+G)(r_i+r_j)}\Phi_K = e^{i(K+G)r_j}\hat{P}(K \to K+G)\Phi_K \tag{3.19}$$

Thus, the projected function has an appropriate PC Bloch symmetry. This projection shows the amount of the PC states Bloch character in the SC states [83, 231, 239]. The unfolding technique is a method that allows to recover the PC Bloch character hidden in the eigenfunctions and eigenvalues of the observable calculated using SC. Unfolding of the electronic band structure is a well defined approach [80,83,231–236,240,241], which is widely used [81, 239, 242–250]. As summarized in [83], unfolding of the SC states from the SCBZ into the PCBZ can be done by projecting SC eigestates on the PC eigenstates:

$$P_{KJ}(k_i) = \langle \Psi_{mK} | \hat{P}(K \to K+G) | \Psi_{mK} \rangle = \sum_j | \langle \Psi_{KJ} | \psi_{k_i j} \rangle |^2 \tag{3.20}$$

where J and j denote energy band indices of the SC and PC at wave vectors K and k_i. Note the similarity between Eq. (3.20) and Eq. (3.6). In fact, the linear expansion coefficients defined in Eq. (3.6) are exactly the spectral weights defined in Eq. (3.20). Therefore, spectral weights contain information about the EPI at finite temperatures.

In the case of equilibrium structures, unfolding spectral weights defined in Eq. (3.20) can be used to recover primitive unit cell band structure exactly, as shown in Fig. 3.3. Moreover, these unfolding weights can be used to calculate the spectral function [82]. However, the usage of the different basis sets lead to different formulations of the unfolding method [251]. Unfolding spinor wave function requires additional formulation. However, here we perform only spin-unpolarized calculations and thus, do not discuss how to treat spinor wave functions in the unfolding procedure. The details of such calculations are discussed in [84].

3.2 Spectral weights formalism in NAO basis

The band-unfolding formalism is well described for DFT codes, utilizing plane waves as basis [81, 84, 239, 248, 249] and codes, which use localized basis functions [85, 232]. We use FHI-aims package, which requires an adaptation of the equations, since the electronic states of the SC Ψ_{NK} and PC ψ_{nk} are expanded as a linear combination of Block-like functions [5] with expansion coefficients $c_{j,nk}$ and $C_{J,NK}$:

$$\psi_{nk} = \sum_j c_{j,nk} \chi_j(k) \tag{3.21}$$

$$\Psi_{NK} = \sum_J C_{J,NK} \chi_J(K) \tag{3.22}$$

Here, the Bloch-type functions were introduced to enforce periodic boundary conditions in FHI-aims [5]. These functions were introduced in Eqs. (1.52, 1.53), but for convenience we will write them again here:

$$\chi_j(k) = \sum_l e^{-ikl} \phi_j \tag{3.23}$$

$$\chi_J(K) = \sum_L e^{-iKL} \Phi_J \tag{3.24}$$

Here, $\phi_j(r)$ and $\Phi_J(R)$ denote atomic orbitals defined in Eq. (1.42) and the sums are taken over all lattice vectors l and L.

The overlap matrix elements $p_{nk,NK}$ are then:

$$p_{nk,NK} = \langle \psi_{nk} | \Psi_{NK} \rangle = \sqrt{\frac{L}{l}} \sum_{jJ} c^*_{j,nk} C_{J,NK} \sum_{l} e^{-ikl} \langle \phi_{j,l} | \Phi_{J,0} \rangle \, \delta_{k-G,K} \tag{3.25}$$

where the first summation runs over all real basis functions $\phi_{i,l}$ and $\Phi_{J,0}$ of the reference primitive cell and perturbed supercell, respectively. The corresponding Born-von Karman supercells contain l and L periodic replicas of the original cell, set at 0, along each Cartesian direction. The presence of the Kronecker delta $\delta_{k-G,K}$ ensures that K is mapped onto k via a reciprocal lattice vector G.

Taking the summation over all n bands in Eq. (3.25) yields the spectral weights defined in Eq. (3.8):

$$P_{k,NK} = \frac{L}{l} \sum_{jJl} C^*_{J,NK} C_{j,NK} e^{-ikl} \langle \Phi_{j,l} | \Phi_{J,0} \rangle \, \delta_{k-G,K} \tag{3.26}$$

where the quantity in the brakets is the overlap matrix, which is present due to the non-orthogonality of NAOs. In the case of calculations with orthogonal basis functions, e.g., plane waves, this quantity vanishes [239, 248]. Eq. (3.26) shows that in order to obtain the spectral weights we only need to calculate band structures for the SC and have a mapping between SC and PC atoms. The methodology to perform band structure unfolding using Eq. (3.26) was described in [85].

In this thesis, we used a slightly different approach to calculate Eq. (3.25). In particular, translation operator $\hat{T}$ commutes with the Hamiltonian and thus, eigenstates of the translation operator can be chosen as eigenstates of the Hamiltonian. Consequently, spectral weights can be calculated by projecting supercell electronic eigenstates on the eigenstates of the projection operator. However, the basis set utilized in FHI-aims is non-orthogonal, which leads to the generalized eigenvalue problem written in Eq. (1.45). In principle, we can perform Löwedin orthogonalization [101] in order to transfer Eq. (1.45) to eigenvalue problem. This is done by defining new basis set $|\Psi'_N\rangle = S^{1/2} |\Psi_N\rangle$, where S is the overlap matrix and Ψ_N is the wave functions obtained in the calculation with supercell. Transformed eigenvalue problem then will have the form $\hat{H}' |\Psi'_N\rangle = E_N |\Psi'_N\rangle$, where $\hat{H}' = S^{-1/2} H S^{-1/2}$. Similarly, to the generalized eigenvalue problem for electronic states, the translation matrix in non-orthogonal basis satisfies a generalized eigenvalue problem:

$$T |u_\alpha\rangle = \lambda_\alpha S |u_\alpha\rangle \tag{3.27}$$

where λ_α and u_α are translation operator eigenvalues and eigenvectors. We note that $T = T'S$, where T' is a permutation matrix, which corresponds to the same orbital translation as T in orthogonal basis. Note that in the orthogonal basis, i.e. when S is an identity matrix, $T' = T$. When Eq. (3.27) is multiplied by $\langle u_\alpha|$, we obtain:

$$\langle u_\alpha | T | u_\alpha \rangle = \lambda_\alpha \langle u_\alpha | S | u_\alpha \rangle \tag{3.28}$$

Next we perform Löwedin transformation for the basis $|u_\alpha\rangle$, by defining $|u'_\alpha\rangle = S^{1/2} u_\alpha$:

$$\langle u'_\alpha | S^{-1/2} T' S^{1/2} | u'_\alpha \rangle = \lambda_\alpha \langle u'_\alpha | S^{-1/2} S S^{1/2} | u'_\alpha \rangle \tag{3.29}$$

Then, we note that due to the symmetry $[T', S] = 0$, which leads to:

$$\langle u'_\alpha | T' | u'_\alpha \rangle = \lambda_\alpha \langle u'_\alpha | u'_\alpha \rangle \tag{3.30}$$

Eq. (3.30) is a standard eigenvalue problem for translation operator in orthogonal basis. Therefore, spectral weights defined in Eq. (3.20) can be calculated as the projection of eigenvectors of the translation operator u'_α in the orthogonal basis on the symmetrically orthogonalized basis functions of the supercell $S^{1/2}\Psi_N$. As an example, Fig. 3.4(a) shows the spectral function of Si calculated using Eq. (3.8) at T=500 K in the harmonic approximation [180]. The temperature-dependence of the band gap of Si is shown in Fig. 3.4(b). The results are in agreement with previous calculations [16, 17, 211] and experimental data [207, 252].

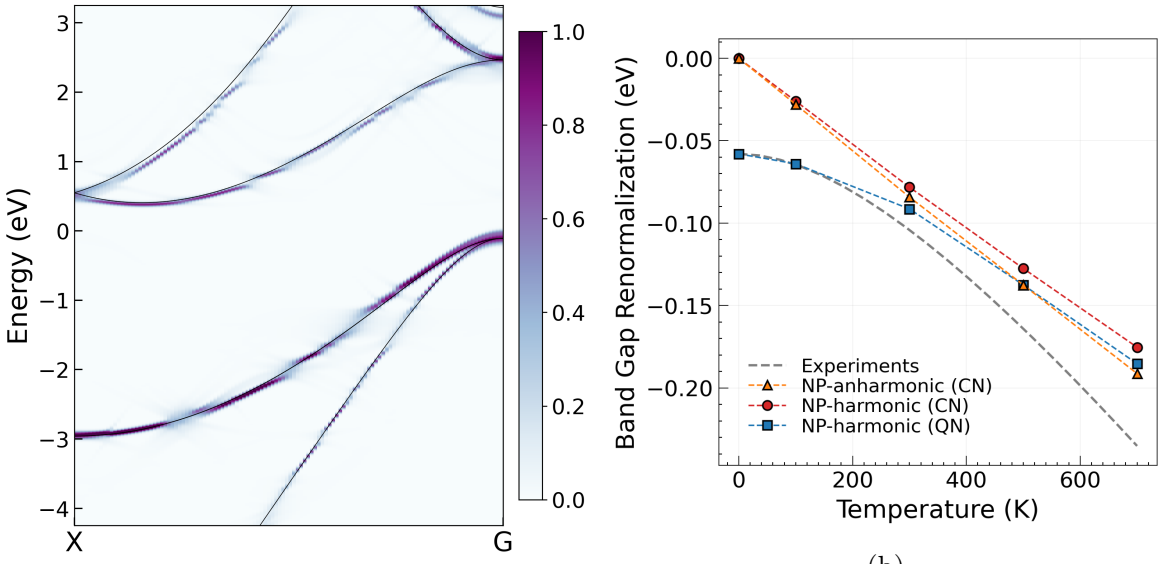

(a) (b)

Figure 3.4: (a) Thermodynamically averaged spectral function of silicon at 500 K, computed along the X-G BZ path. Band structure at zero temperature is shown as black lines. (b) Temperature-dependent band gap renormalization in Silicon. Calculations were performed with LDA xc-functional and the cubic supercell with 216 atoms, using a non-perturbative (NP) treatment of the electron-phonon interaction. Nuclear motion is considered in the classical (CN) and the quantum (QN) limits. The experimental data is taken from [252].

3.3 Influence of lattice thermal expansion and polar corrections on the band gap renormalization

Anharmonic effects can significantly alter the phonon spectrum of materials with weak bonding and large amplitude of the nuclear oscillations [68, 181, 214]. For such systems usually the harmonic approximation is not valid. Inclusion of anharmonicity leads to renormalization of the normal modes that affects phonon-phonon scattering and electron-phonon interaction in these materials [68].

The lattice thermal expansion – purely anharmonic effect, can be accounted by using the quasi-harmonic approximation (QHA), which predicts equilibrium volumes of crystals at finite temperatures [198, 253, 254]. For demonstration purposes, we computed the band gap renormalization caused by the LTE for silicon and GaAs using the QHA as shown in Fig. 3.5(a). In silicon, the LTE causes a small band gap opening (around 10 meV at T=700 K), while in GaAs the band gap at T=700 K is decreased by approximately 50 meV because of the LTE. Considering that at T=700 K, the total band gap renormalization in silicon is around -240 meV and in GaAs it is around -300 meV, the contribution from the LTE cannot be neglected. We should also note that phonon zero-point energy changes the equilibrium lattice parameters at T=0 K. For Si the zero-point lattice expansion is around 9 meV, whereas for GaAs it is -31 meV [255].

The QHA can provide qualitatively reasonable and sometimes even quantitatively accurate results [152,154]. For example, aforementioned Si has negative LTE at low temperatures and this effect is can be described using the QHA [256]. However, one should always remember that the QHA accounts for LTE in the leading order and does not capture anharmonicity completely [254]. Recently, it was shown that only fully anharmonic calculations of the lattice dynamics of silicon allow to obtain quantitatively accurate agreement with the experimental measurements of the lattice expansion in Si [257].

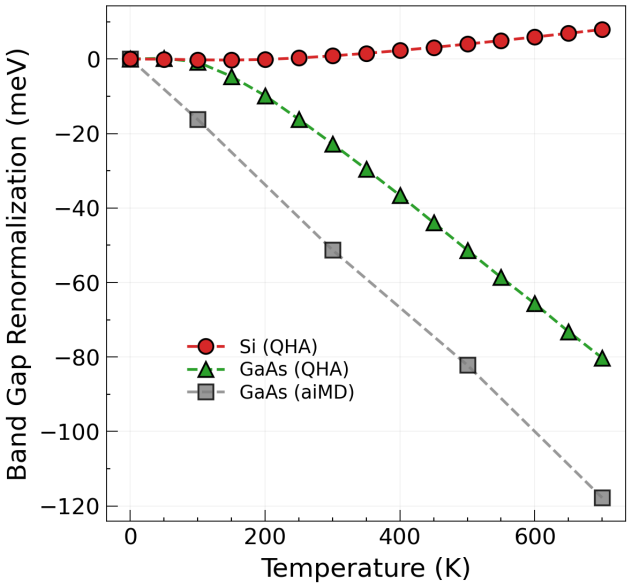

Figure 3.5: Band gap renormalization caused by the LTE in silicon and GaAs. The LTE is calculated using the QHA and by aiMD.

As was shown in the previous chapter, the LTE can be evaluated in aiMD simulations of the canonical ensemble by computing the average stress tensor along the aiMD trajectory. In this approach one computes the internal pressure at finite temperatures, which is them used to reoptimize the structure until the stress tensor becomes negligible (see Sec. 2.4). Results of the LTE influence on the band gap renormalization calculated from the aiMD for GaAs are presented in Fig. 3.5. At T=700 K, the LTE calculated fully anharmonically leads to a larger renormalization of the gap than in the calculations done with the QHA.

Before we move to the next chapter we would like to highlight that consideration of long-range electrostatic effects is also important for computations of the band gap renormalization. In ionic solids such as GaAs or NaCl, the displacement of atoms along the longitudinal optical (LO) modes induce macroscopic electric fields, which have long-range nature and are created by the opposite movement of the atoms with different charges. These fields induce additional scattering of electrons and thus, additional renormalization of electronic states. In literature, this phenomenon is called Fröhlich electron-phonon coupling or polar coupling [16, 40, 42, 53, 54, 93]. The inclusion of polar coupling effects was shown to be crucial to accurately determine band gap renormalization, for example, for polar materials as GaAs [209], GaN [93], and $SrTiO_3$ [85]. Rigorous determination of the correction caused by polar coupling and methodology to compute it from the first principles was recently introduced [43]. Such calculations are quite complex and since polar effects are not the main topic of this thesis we utilize a simplified methodology presented in [93]. In this method an analytical expression for the Fröhlich correction in the adiabatic case is derived:

$$\langle \Delta E_n^{\mathrm{Fr}} \rangle_{\mathrm{T}}^{\mathrm{HA}} = \frac{-\alpha \hbar \omega_{\mathrm{LO}}}{\pi} \cdot \left[2 \tan^{-1} \left(q_{\mathrm{F}} a_{\mathrm{LO}} \right) \left[n_T + 1 \right] + \ln \left| \frac{q_{\mathrm{F}} - a_{\mathrm{LO}}^{-1}}{q_{\mathrm{F}} + a_{\mathrm{LO}}^{-1}} \right| n_T \right] \tag{3.31}$$

where $\hbar$ is Plank's constant, ω_{LO} is a frequency of the LO phonon, n_T is a Bose-Einstein occupation factor $\left[\exp \left(\hbar \omega_{\mathrm{LO}} / k_B T \right) - 1 \right]^{-1}$, q_{F} is a truncation parameter, which could be chosen to be equal to the radius of the Debye sphere – the sphere with the volume equal to the volume of the BZ of the supercell used for simulations and q_{LO} is $\sqrt{\hbar^2 / 2 m^* \hbar \omega_{\mathrm{LO}}}$, where m^* is an effective mass of electrons or holes. α in Eq. (3.31) is a dimensionless polaron constant, which determines the strength of the polar coupling:

$$\alpha = \frac{e^2}{4 \pi \epsilon_0 \hbar} \left(\frac{1}{\epsilon_\infty} - \frac{1}{\epsilon_0} \right) \left(\frac{m^*}{2 \hbar \omega_{\mathrm{LO}}} \right)^{1/2} \tag{3.32}$$

where e is a charge of electron, ϵ is vacuum permittivity, ϵ_∞ and ϵ_0 are high-frequency dielectric constant and static permittivity, respectively. In the limit $\mathrm{q_F} \to \infty$ and at T=0 K, Eq. (3.31) reduces to $\Delta E_n^{\mathrm{Fr}} = -\alpha \hbar \omega_{\mathrm{LO}}$ [258].

Practically, relatively small differences in parameters can cause substantial differences in the polar correction estimation, for example, the difference between the high-frequency dielectric constant and static permittivity has a substantial effect on the polaron constant α. Sensitivity can be demonstrated, for example, using GaAs, which has a small difference between the static permittivity (12.5) and the high-frequency dielectric constants (10.9). Consequently, the Fröhlich correction calculated for GaAs is relatively small. At zero temperature, the polar coupling cause a shift of the valence band maximum of GaAs by 2 meV, while the conduction band maximum shifts by -4.5 meV. Thus, the band gap renormalization caused by Fröhlich polar coupling in GaAs is rather negligible (-6.5 meV at T=0 K and -7.5 meV at T=300 K). However, as was recently demonstrated in [259] the case of GaAs is rather an exception and for some materials inclusion of polar correction can cause substantial (of the order of 100 meV) gap renormalization. We will demonstrate the substantial importance of the polar correction for GaN in the next chapter.

Summary of the chapter

In this chapter, we demonstrated how the nuclear motion and the LTE cause the renormalization of electronic eigenstates at finite temperatures. We reviewed the AHC formalism and showed how to overcome its limitations. The methodology used in this thesis was established in the study [85] and allows to calculate materials with any degree of anharmonicity on equal footing. We also discussed improvements made to the initial implementation [85], such as the analytical treatment of the eigenvectors of the translation operator and the incorporation of diagonal and non-diagonal transformation matrices. The benchmark of the novel implementation is presented in the next chapter. Evaluation of the total band gap renormalization at finite temperature also requires calculation of the contribution from the LTE and evaluation of the polar correction. We discussed how the LTE can be taken into account in the QHA and aiMD simulations. The polar correction in this thesis is estimated using the formulation presented in [93].

Chapter 4

Temperature-dependent band gap renormalization in diamond and zinc blende GaN

In this chapter, we systematically discuss the benchmark of the fully anharmonic non-perturbative methodology for temperature-dependent band gap renormalization calculations. We will discuss numerical aspects such as thermodynamic averaging, estimation of the error bars, and the influence of the supercell size used in simulations. Diamond and zinc blende gallium nitride (GaN) are employed as test systems due to the large amount of reference literature data [16, 17, 52, 86–94]. All calculations are performed at the DFT-LDA level of theory with the FHI-aims code [5]. Computational details are shown in Appendix B.

4.1 Temperature-dependent spectral functions

Prior to presenting the benchmark, it is necessary to establish a protocol for calculating the temperature-dependent spectral function and band gap renormalization. The distorted structural configurations, which give access to the influence of temperature on the nuclear movement, can be generated either in the harmonic approximation [180] or by conducting aiMD simulations. For each of the atomic configurations (in the following referred to as a sample) considered, a band structure calculation is performed, followed by the computation of spectral weights utilizing Eq. (3.26). These weights are then used to calculate the momentum-resolved spectral function A(k,E) for each sample within the set, as outlined in Eq. (3.8). The thermodynamically averaged spectral function $\langle \mathrm{A(k,E)} \rangle_{\mathrm{T}}$ is obtained by averaging the results over the entirety of the set. The delta function $\delta(x)$ in Eq. (3.8) in practical calculations is replaced by a Gaussian function $G(x)$[1]:

$$G(x; A, \mu, \sigma) = \frac{A}{\sigma\sqrt{2\pi}} \exp\left(-\frac{(x-\mu)^2}{2\sigma^2}\right) \tag{4.1}$$

where the parameters denote the amplitude A and the center μ of the Gaussian, and the characteristic width of the Gaussian σ. The full width at half maximum of the Gaussian

[1] It can be shown by considering Poisson's integral that the delta function $\delta(x)$ can be represented as the Gaussian function with very tiny width, i.e., $\delta(x) = \lim_{\sigma \to 0} G(x)$

peak is $2\sigma\sqrt{2\ln 2}$.

Fig. 4.1(a) shows the thermodynamically averaged momentum-resolved spectral function of GaN at T=700 K. The electronic states experience a shift and obtain a finite width under the influence of temperature. The renormalization of electronic states, at some finite temperature T, is defined as the difference between the electronic state energy at temperature T and its energy calculated at zero temperature. The energetic spreading of the electronic states is related to the scattering at finite temperatures and manifests the finite lifetime of the quasiparticles [8].

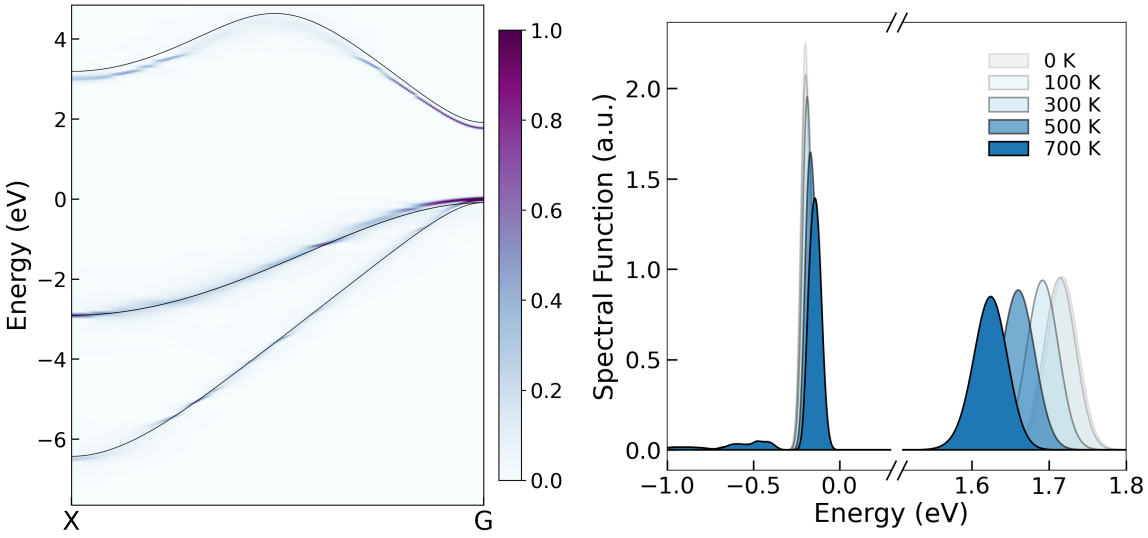

(a) (b)

Figure 4.1: (a) Thermodynamically averaged spectral function $\langle A(k,E)\rangle_T$ of GaN at T=700 K, calculated along X-G BZ path. The band structure in static equilibrium is shown using black lines. Averaging is done over 50 samples. The supercell contains 216 atoms. (b) Spectral function at the G-point at different temperatures. Note that DFT-LDA calculations underestimate [124–126] the experimental band gap value of GaN, which equals 3.28 eV [90]. The spectral function scale on both plots has arbitrary units, but we normalized it in plot (a).

To determine the gap between valence and conduction bands at a specific crystal momentum, a cut of the spectral function at this momentum is done. For example, the spectral function of GaN resolved at the G-point and calculated at different temperatures, is shown in Fig. 4.1(b). The temperature-dependent band structure can be obtained by connecting the locations of the peaks of the spectral function. The connection of the peaks between neighboring k-points of the BZ should be done accurately, considering (anti)crossing effects [260]. The band gap is measured as the distance between the positions of the Lorentzian functions fitted to spectral function peaks, which represent valence band maximum and conduction

band minimum.[2] The Lorentzian function is the singly peaked function defined as:

$$L(x; A, \mu, \sigma) = \frac{A}{\pi}\left[\frac{\sigma}{(x-\mu)^2 + \sigma^2}\right] \tag{4.2}$$

where the parameters denote the amplitude A and the center μ of the Lorentzian, and the characteristic width of the Lorentzian σ. The full width at half maximum of the Lorentzian peak is 2σ. In practice, we chose a certain energy window, which covers a region near the band gap, and fit as many Lorentzian functions, as there are electronic energy states inside this energy window. The adjustment of the numerical parameters of Lorentzians to the spectral function peaks is done based on the least-squares minimization. Band structure, calculated for the primitive cell in the equilibrium, is used to initialize positions of the Lorentzians. The parameters of those Lorentzians, which are fitted to the degenerate states, are enforced to be equal to each other.

4.2 Numerical aspects of calculations

Thermodynamic averages

The number of samples, used for thermodynamic averaging during the calculations of the spectral function at finite temperatures should be carefully converged. In this section, we will discuss the numerical aspects of this convergence process. The utilization of the harmonic sampling methodology [180] was employed in order to generate uncorrelated geometries and to investigate the impact of the ensemble size on the band gap's renormalization convergence.

The convergence of the band gap renormalization with respect to the number of samples used for averaging for GaN at T=300 K is presented in Fig. 4.2(a). The calculations were performed utilizing both diagonal and non-diagonal transformation matrices, as defined by Eq. (3.9), to generate supercells from a primitive cell. It was found that calculations with larger supercells exhibit smaller variations of the band gap renormalization value with respect to the number of samples in a set. The standard error of the mean[3] of the band gap renormalization for the simulation cells of any shape and size did not exceed 1 meV, as shown in Fig. 4.2(b). Similar trends were observed for diamond as demonstrated in Fig. 4.3(a, b), where the calculations were conducted at T=250 K. It is noteworthy that these results are similar across a range of temperatures as shown in Fig. 4.4(a, b).

Temporal averages

Starting aiMD simulations with different initial conditions (atomic positions and velocities) may result in diverse outcomes due to the inherent limitations of simulation time and consequent potential undersampling of phase space. In order to determine the dependence of the results on a particular aiMD trajectory, we employed forces obtained in the harmonic

[2] We assume that the spectral function peaks have Lorentzian lineshape, as discussed in [8]. Fitting can be also performed with Gaussian or Voigt functions.

[3] The standard error of the mean $\sigma_{\bar{x}}$ is calculated for n statistically independent samples $\{x_1, x_2, \ldots, x_n\}$ taken from a statistical population with a standard deviation of σ as $\sigma_{\bar{x}} = \sigma/\sqrt{n}$. The discussion of difference between the standard error and the standard deviation is presented in [261].

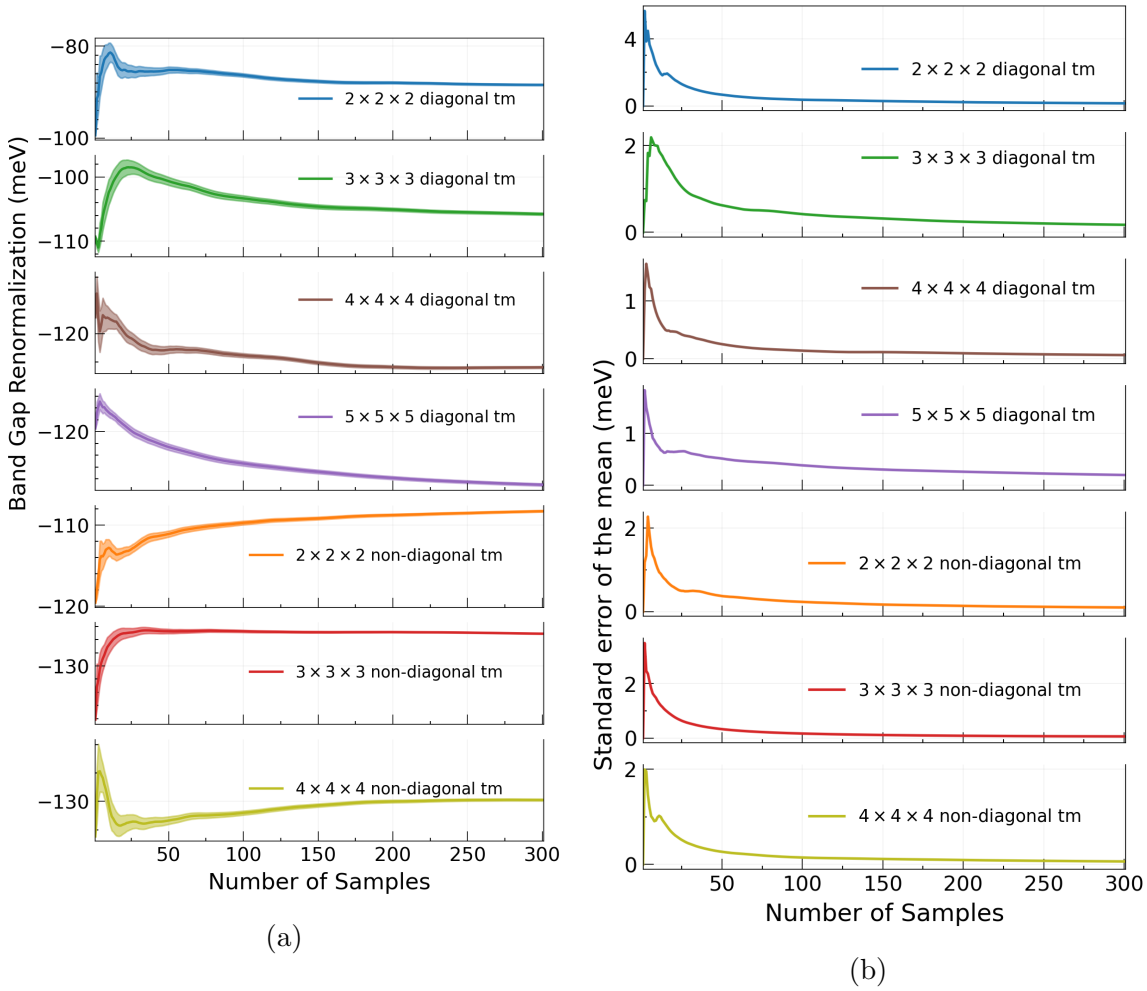

Figure 4.2: (a) Convergence of the band gap renormalization for GaN at T=300 K with respect to the number of samples used for averaging. (b) Standard error of the mean of band gap renormalization with respect to the number of samples used for averaging. The shadowed region on plot (a) also represents standard error of the mean. Diagonal and non-diagonal transformation matrices (tm) are used to generate supercells.

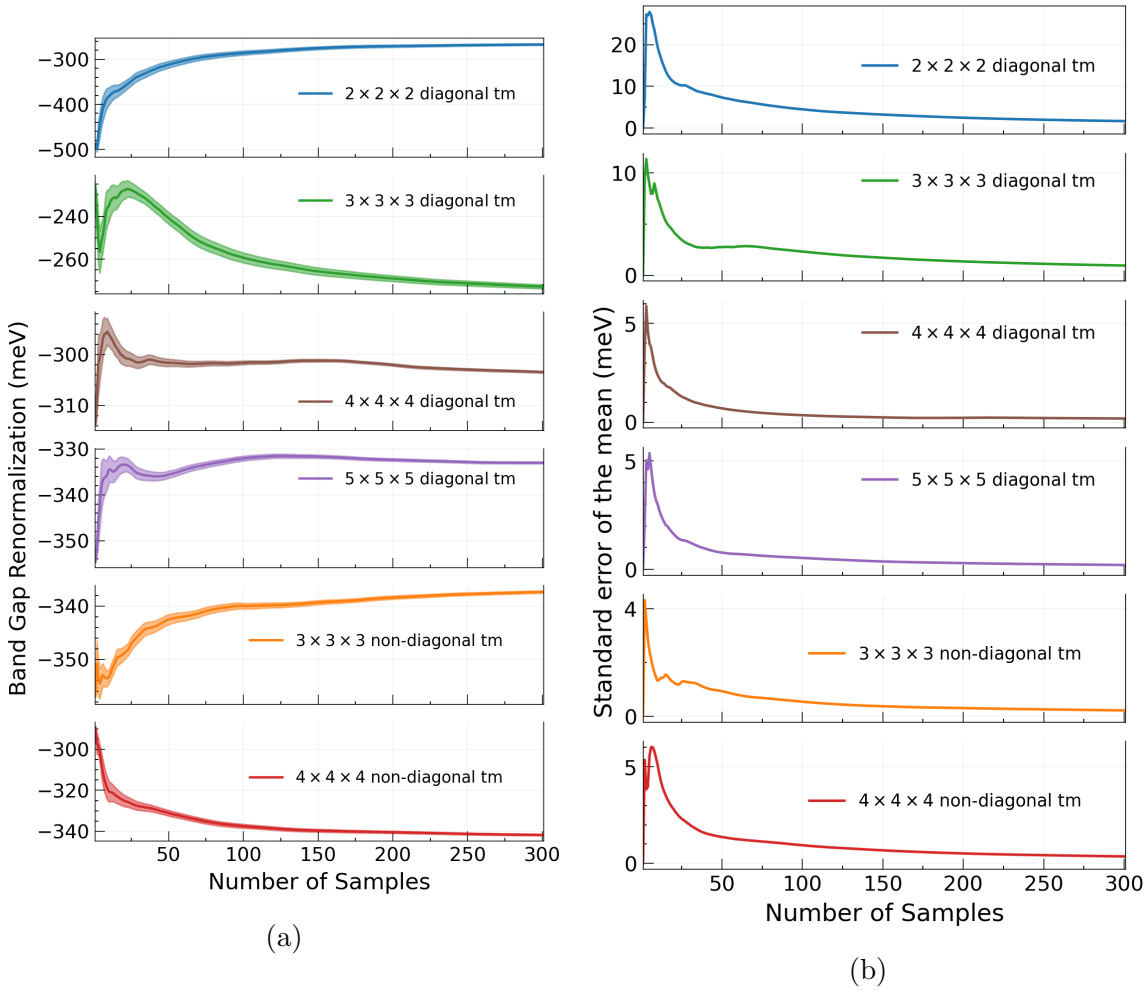

Figure 4.3: (a) Convergence of the band gap renormalization for diamond at T=250 K with respect to the number of samples used for averaging. (b) Standard error of the mean of band gap renormalization with respect to the number of samples used for averaging. The shadowed region on plot (a) also represents the standard error of the mean. Diagonal and non-diagonal transformation matrices (tm) are used to generate supercells.

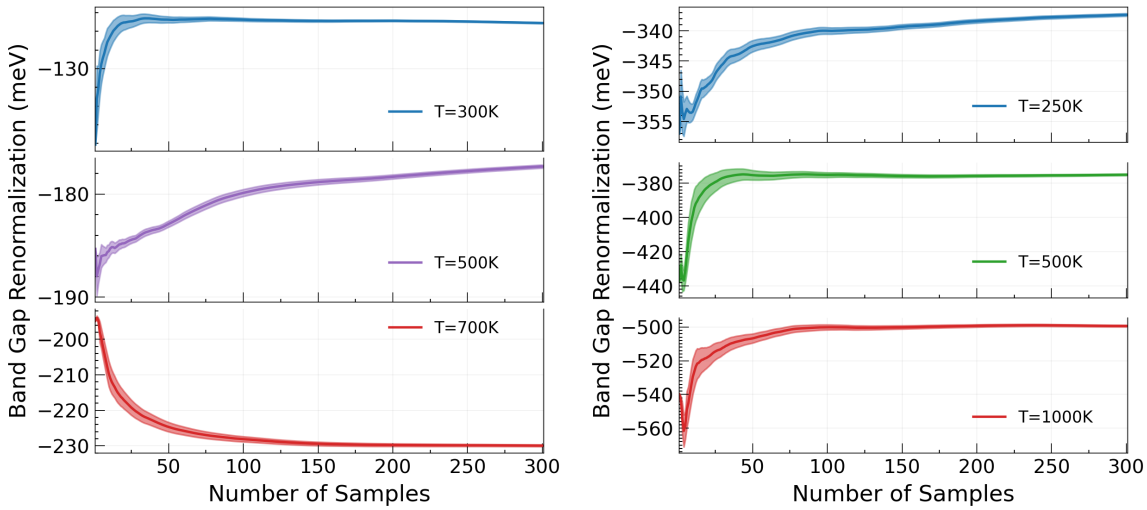

Figure 4.4: Convergence of the band gap renormalization with respect to the number of samples for (a) GaN and (b) diamond at different T. The shadowed region represents the standard error of the mean. In both cases the supercells are cubic (generated using non-diagonal transformation matrix) and contain 216 atoms.

approximation and generated a series of aiMD trajectories for GaN at T=300 K. Each harmonic aiMD trajectory has 10 ps length, calculated with a timestep of 1 fs. For band gap renormalization calculations, we randomly extracted 100 samples from each trajectory. The temporal average for the renormalization of the band gap in GaN at T=300 K is illustrated in Fig. 4.5. The value of the band gap renormalization has a negligible change once more than a single aiMD trajectory is used.

Supercell size and shape

The band gap renormalization decays inversely proportional to the supercell size, as shown in Fig. 4.6(a) and Fig. 4.6(b) for diamond and GaN, respectively. Usage of supercells with 216 atoms, generated through the application of a non-diagonal transformation matrix, is deemed sufficient for evaluation of temperature-dependent renormalization of the band gaps in both materials. The utilization of a non-diagonal transformation matrix may be beneficial, as it allows for the attainment of converged results with smaller supercells, as has been discussed in detail for phonon spectrum calculations [262].

It is important to note how the band gap estimation is done in the case of diamond. At zero temperature, the VBM of diamond is degenerate. However, recent computational studies have reported that at finite temperatures, this degeneracy is lifted [182, 212, 228]. This phenomenon has also been observed in silicon [85, 212]. Several authors have proposed explanations for the lifting of this degeneracy. Some suggest that it is a finite size effect caused by zone-center phonons, which should disappear in the limit of large supercells [212]. Others argue that it can be attributed to quantum nuclear effects [228]. Our calculations shows that

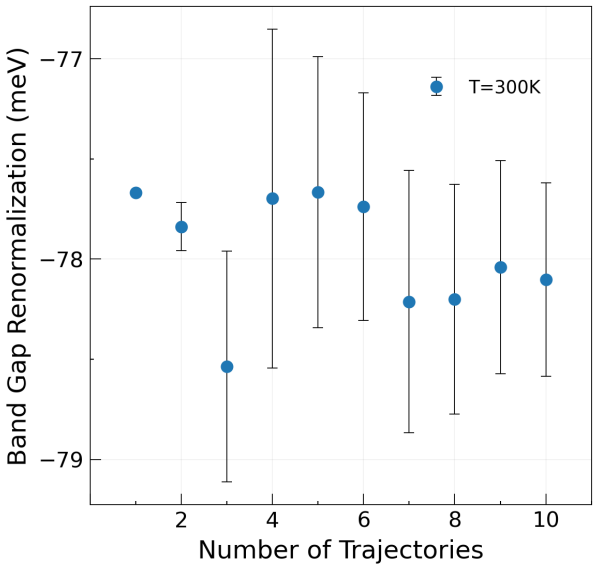

Figure 4.5: Temporal average of the band gap renomalization in GaN at T=300 K. A non-diagonal transformation matrix is used to create supercells with 64 atoms. 100 samples were chosen randomly from each trajectory for averaging.

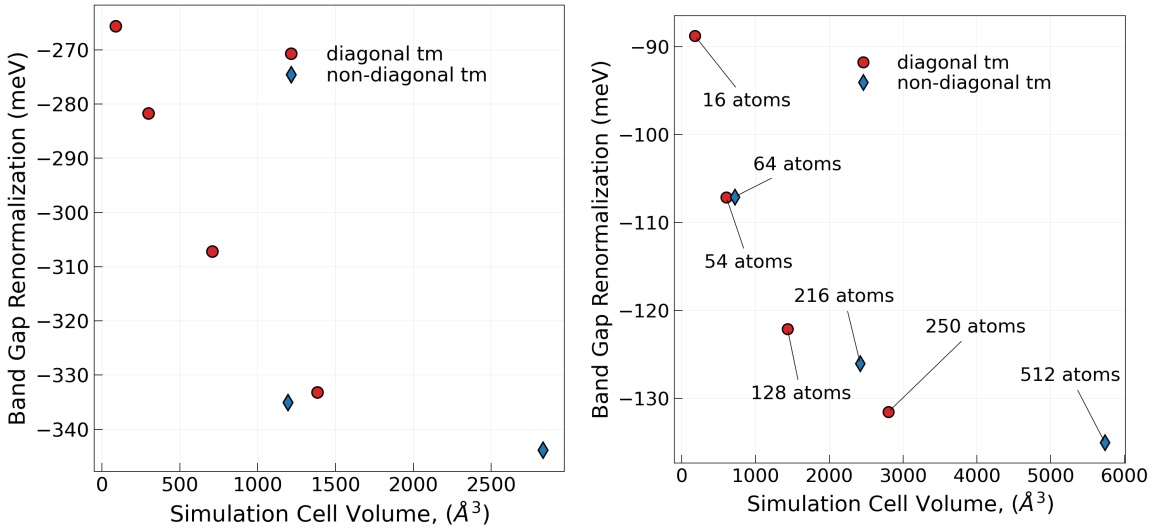

Figure 4.6: Band gap renomalization in (a) diamond at T=250 K and (b) GaN at T=300 K with respect to the supercell size. Diagonal and non-diagonal transformation matrices (tm) are used to generate supercells.

if diagonal transformation matrices are used to create supercells, the degeneracy splitting is indeed observed, as depicted in Fig. 4.7 (a). In these cases, the band gap renormalization is calculated as the difference between the average positions of all bands that form the VBM and all bands that form the CBM [85, 182, 212]. However, when a non-diagonal transformation matrix is used to create a supercell, the degeneracy splitting does not occur, as shown in Fig. 4.7(b).

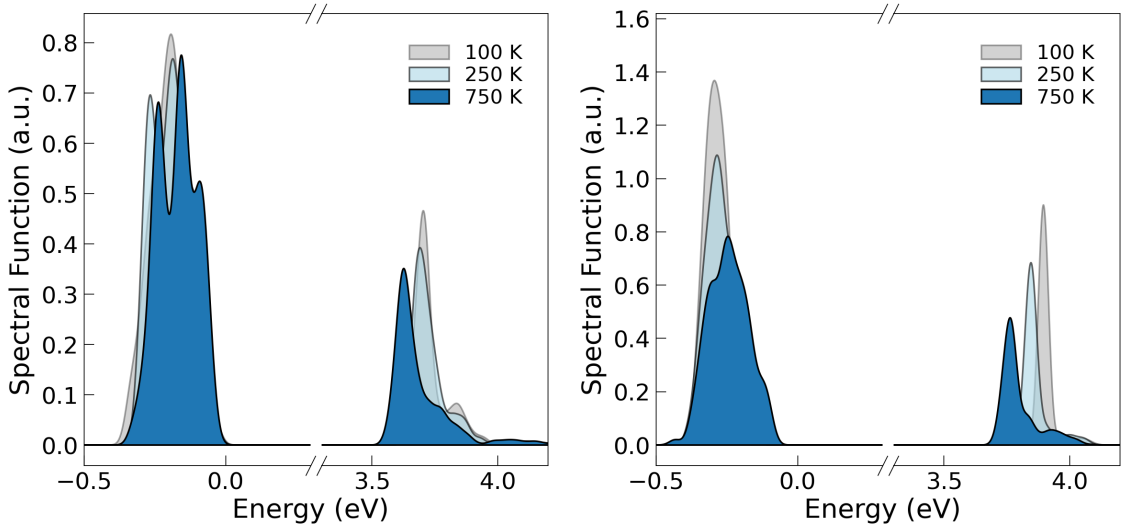

(a) (b)

Figure 4.7: The valence band maximum and conduction band minimum of diamond at different temperatures. Calculations were performed utilizing a supercell (a) generated through the application of a diagonal transformation matrix, resulting in a supercell containing 250 atoms and (b) utilizing a supercell with 216 atoms generated employing the non-diagonal transformation matrix.

4.3 Influence of the nuclear motion and polar corrections

We start the discussion of the temperature-dependent band gap renormalization in diamond and GaN within the harmonic approximation. Fig. 4.8(a, b) shows that the classical treatment of the nuclear dynamics results in a linear dependence between the band gap renormalization and temperature, whereas a quantum treatment of the nuclear dynamics results in a non-linear temperature dependence for both materials. In the case of GaN, calculations in the classical limit yield -135 meV gap renormalization at T=700 K, which is lower than in the case of calculations with a quantum treatment of the nuclear motion. This highlights the magnitude of the correction associated with the zero-point motion. Zero-point renormalization of the band gap (ZPR) is evaluated as a difference between the classical zero-temperature gap and the gap calculated using quantum limit for the nuclear motion. The ZPR calculated for GaN is -89 meV, which is in agreement with the -94 meV previously reported in [182]. For the indirect band gap of diamond we obtain the ZPR=-348 meV (-345 meV with *tight* settings), which is also in good agreement with previous theoretical works [16,211] and experiments [89,207]. We also calculated the ZPR of the direct band gap of diamond and obtained results are in agreement with previous publications as shown in Tab. 4.2.

GaN is a polar material. Thus, it is necessary to consider the impact of the Fröhlich polar correction to the band gap renormalization. To accomplish this and quantify the role of the polar correction in GaN, we utilized Eq. (3.31), which necessitates information about the static permittivity ϵ_0, high-frequency dielectric tensor ϵ_∞, effective mass of electrons m_e^* and holes m_h^*, and the energy of LO-phonon $\hbar\omega_{\mathrm{LO}}$. In order to accurately determine $\hbar\omega_{\mathrm{LO}}$, it is essential to take into account LO-TO splitting through the utilization of NAC [171]. The

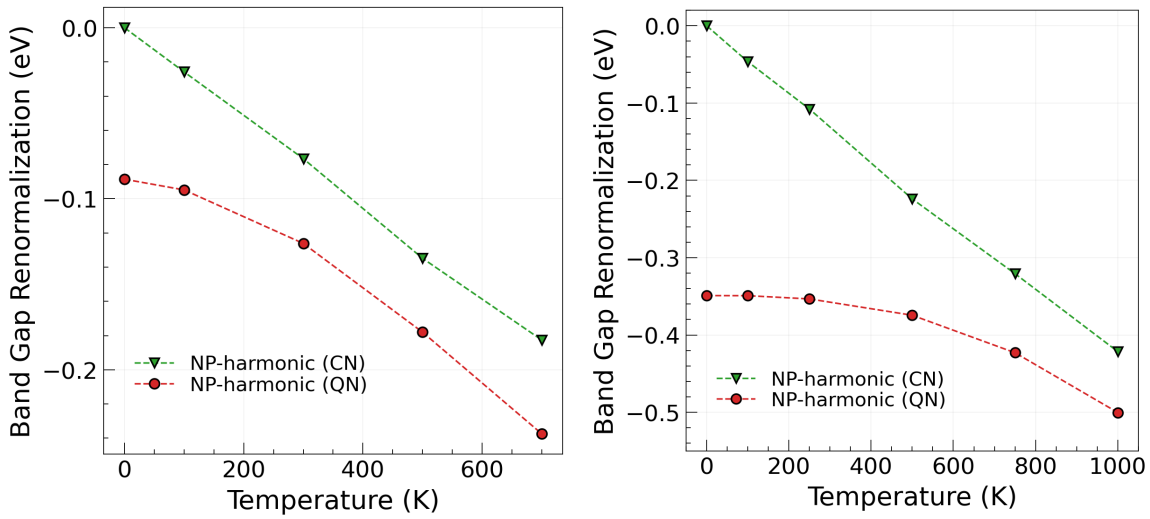

Figure 4.8: Temperature dependence of the band gap renormalization in (a) GaN and (b) diamond due to the nuclear motion. Calculations are done with LDA functional and cubic supercell containing 216 atoms. Thermodynamic averaging is done using 50 samples for GaN and 100 samples for diamond. Non-perturbative (NP) harmonic treatment is applied taken into account classical (CN) and quantum (QN) statistics for the nuclear motion.

NAC requires to know the Born effective charges Z^* and the high-frequency dielectic constant ϵ_∞, as discussed in Sec. (2.1). We carried out the calculation of ϵ_∞ in accordance with the formalism presented in [175], yielding a value of ϵ_∞=5.56. The Z* tensor was computed based on the method outlined in Sec. (2.1) and found to be isotropic (Z^*_{Ga}=2.66 and Z^*_{N}=-2.66). After the application of NAC we obtained the energy of LO phonon $\hbar\omega_{\mathrm{LO}} = 91$ meV. The conduction band of GaN is isotropic, as evidenced by the nearly equal effective mass of electrons in all directions, which has been calculated to be m^*_e=0.17 m_e, where m_e is the free electron mass.

The VBM of GaN is triply degenerate. [4] The effective masses of heavy and light holes display anisotropy. To estimate the polar correction for the valence band, we averaged effective masses of heavy and light holes calculated along the G-X BZ path. This was shown to be legitimate for the estimation of the conduction band renormalization due to the polar correction [93]. The obtained effective mass for heavy holes is m^*_{hh}=-0.84 m_e, and for light holes m^*_{lh}=-0.18 m_e. We utilized the experimental value of the static permittivity, ϵ_0=9.7 taken from [90]. It should be noted that the values of both ϵ_∞ and ϵ_0 in the work [93] were taken from literature data [90].[5] The parameters employed in calculation of Eq. (3.31) and the values used in other studies are summarized in Tab. 4.1. A consistency check with literature data can be performed by comparing the polaron constant α_c, calculated for the conduction band and polar correction to the conduction band in terms of the relation $\Delta E_c^{\mathrm{Fr}} = -\alpha\hbar\omega_{\mathrm{LO}}$ (see Sec. (3.3)). It can be then concluded that the results obtained in this study are consistent

[4] We performed calculations without spin-orbit coupling, thus the spin-off band is degenerate as well. The influence of SOC on the band structure is discussed in detail in [263].

[5] As was told to the author of the thesis by the first author of the paper [93] in the private correspondence.

with published data as shown in Tab. 4.1. The slight discrepancy can be attributed to variations in the longitudinal optical phonon energy, effective masses, high-frequency dielectric constant, and static permittivity utilized in the respective studies.

Table 4.1: Parameters of GaN used to compute the polar correction to the CBM in our work and in the literature. (a) is this work, (b) is [93], (c) is [213], (d) is the experimental data measured at T=300 K [90].

Approach	a, (Å)	ϵ_∞	ϵ_0	m_e^*	$\hbar\omega_{\mathrm{LO}}$ (meV)	α_c	ΔE_c^{Fr} (meV)
LDA[a]	4.475	5.56	9.7	0.17	91.3	0.39	-35
LDA[b]	4.499	5.3	9.7	0.16	89.0	0.42	-37
GGA[c]	4.545	6.13	11.0	0.144	86.0	0.34	-29
Exp[d] (300 K)	4.52	5.3	9.7	0.13	87.3	0.38	-33

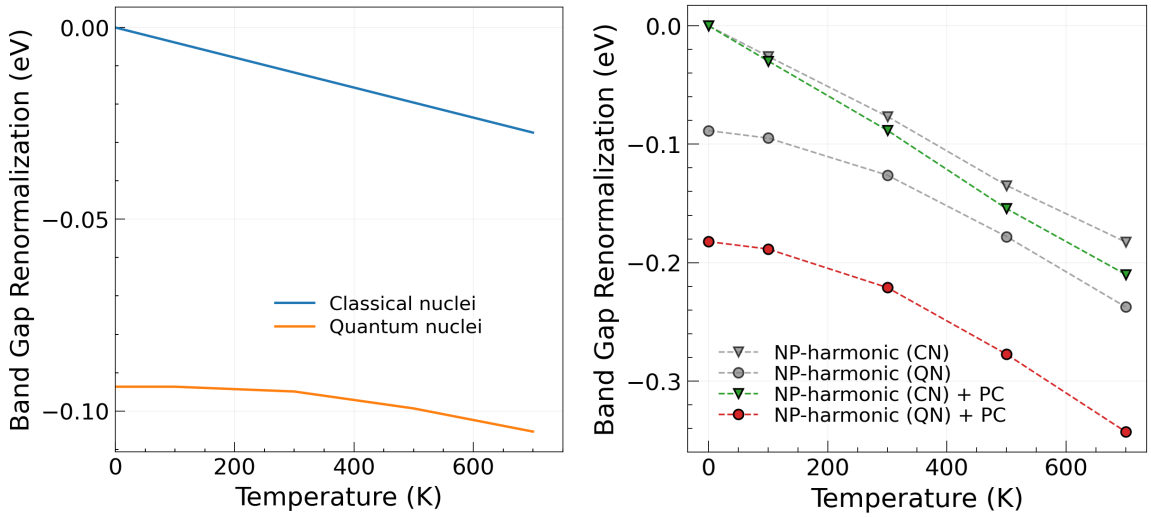

(a) (b)

Figure 4.9: (a) Temperature dependence of the Fröhlich polar correction to the band gap renormalization in GaN, calculated using Eq. (3.31). In the case of classical nuclei, the Bose-Einstein factor is replaced by its classical limit $k_{\mathrm{B}}T/\hbar\omega_{\mathrm{LO}}$ and zero point vibrations are excluded. (b) Nuclear motion influence on the band gap renormalization at finite temperatures, with and without the inclusion of the polar correction (PC).

Fig. 4.9(a) demonstrates the temperature dependence of the Fröhlich polar correction to the band gap in GaN. We found that the polar correction to the ZPR equals -93 meV, which reflects a considerable role of the Fröhlich interaction in GaN. Polar correction calculated in the quantum limit does not grow that much with temperature and equals -105 meV at T=700 K. Calculations in the classical limit lead to the polar correction of -28 meV at T=700 K. Inclusion of the polar correction to the temperature dependence of the band gap renormalization caused by the nuclear motion is shown in Fig. 4.9(b). Consequently, the ZPR for GaN is obtained by summing contributions from the zero-point motion (-89 meV) and the polar correction (-93 meV), which results in the band gap ZPR of -182 meV. These

Table 4.2: The ZPR of the band gap of diamond and GaN. Values in curvy brakets represent calculations in which *tight* numerical settings and basis set of FHI-aims was used for calculations. Experimental value of the ZPR for GaN is reported for the wurtzite polymorh [264]. References are given in square brakets. All values are reported in meV units.

	This Work	Previous	Experiment
C-indirect	-348 (-345)	-330 [16], -344 [211], -334 [17], -345 [212]	370 [207], -410 [89]
C-direct	-429 (-433)	-409 [265], -410 [17], -450 [212] -416 [16], -430 [211]	-180±150 [89] -450±370 [89]
GaN	-182 (-180)	-175 [94], -150 [93], -176 [213] -127 [92], -94 [182]	-180 [264]

results are in agreement with previous works, as summarized in Tab. (4.2). Some discrepancy between our results and literature data could come from the different lattice parameters used in the calculations, basis sets, and the used frameworks. Experimental value for the ZPR of zinc blende GaN is not known to the best of our knowledge. However, we assume that wurtzite GaN has at least comparable ZPR as zinc blende GaN. Thus, for comparison, we added experimentally measured value for the wurtzite polymorph of GaN [264] to Tab. 4.2.

4.4 Anharmonicity and lattice thermal expansion

A fully-anharmonic, non-perturbative treatment of the band gap renormalization in GaN and diamond was performed by sampling the phase space of these materials via aiMD simulations. The results indicate that the anharmonic treatment of the nuclear movement do cause detectable, but not massive changes in band gap renormalization for both materials as shown in Fig. 4.10(a, b). Specifically, for GaN at T=700 K, the anharmonicity contribution to the nuclear movement results in an extra -34 meV renormalization of the band gap. Similarly, at T=1000 K in diamond, the anharmonic treatment of nuclear movement causes an extra -18 meV renormalization of the band gap, in agreement with the results reported in [228].

The LTE result in additional change of the band gap with temperature. We have calculated the band gap renormalization caused by the LTE for both materials in the QHA and fully anharmonically using aiMD simulations as discussed in Sec. 2.4. The results of these calculations are presented in Fig. 4.11(a, b). In the case of diamond, the band gap renormalization caused by the LTE, as calculated using the QHA, was determined to be -34 meV at a temperature of T=1000 K. The band gap renormalization caused by LTE, which is calculated via aiMD, was found to be -37 meV at T=1000 K. These values are consistent with the previously estimated value of -30 meV reported in [228]. The small influence of the LTE in diamond can be attributed to the relatively low LTE of this material [266], e.g., the volume of the crystal expands by just 1.5% at T=1000 K. In contrast to diamond, the LTE has been found to have a tangible impact on the band gap renormalization in GaN, as demonstrated in Fig. 4.13(a). Furthermore, the LTE calculated via aiMD is found to be larger than calculated using the QHA, which cause a larger band gap closing in the former case. Specifically, at

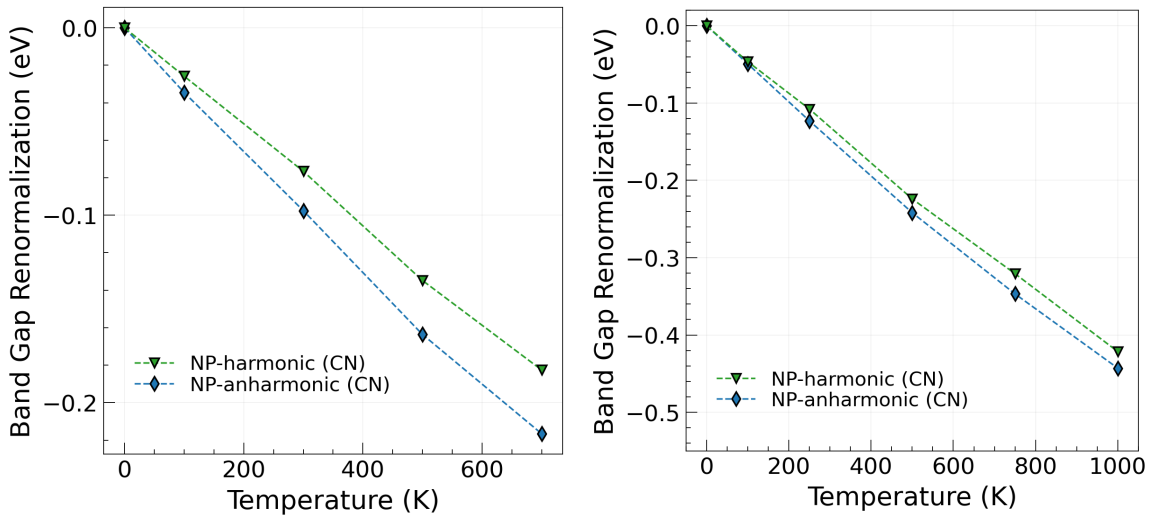

Figure 4.10: Temperature dependence of the band gap renormalization in (a) GaN and (b) diamond due to the nuclear motion calculated in the harmonic approximation and fully anharmonically using aiMD. Calculations are done with LDA xc-functional and cubic supercell containing 216 atoms.

T=700 K, the renormalization calculated using aiMD (approximately -120 meV) is twice as large as the one calculated in the QHA. The volume of GaN crystal expands by 1.5% once LTE is calculated using aiMD and only by 0.7% in the case of calculations in the QHA.

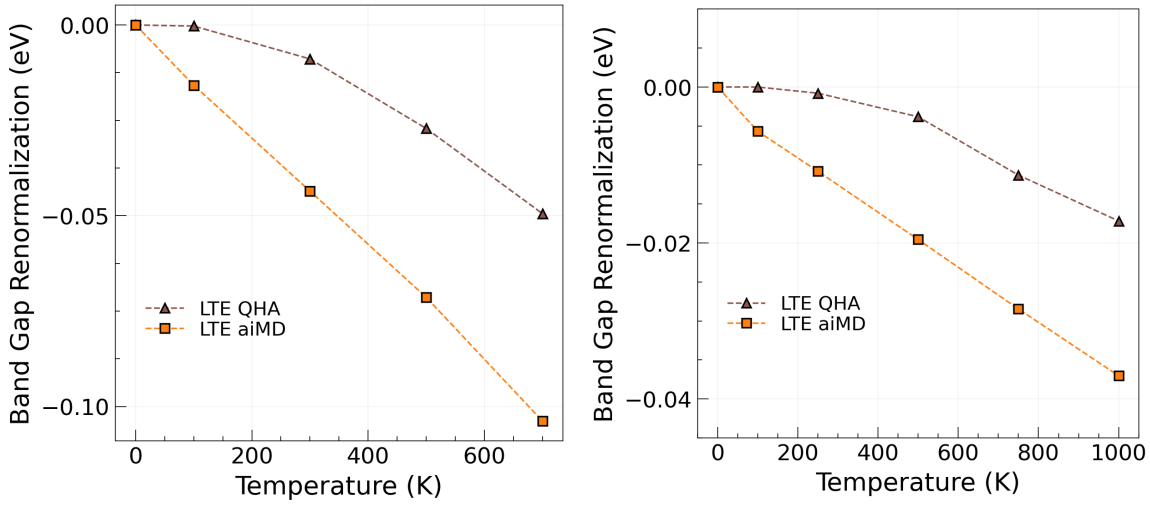

Figure 4.11: Lattice thermal expansion influence on band gap renormalization in (a) GaN and (b) indirect band gap of diamond. LTE is calculated in the QHA and via aiMD simulations, by estimating internal pressure appeared in the NVT simulations.

The quantitative estimation of the anharmonicity can be done by computing the anharmonicity measure $\sigma^A(T)$ defined in Eq. (2.38). As shown in Fig. 4.12, both compounds

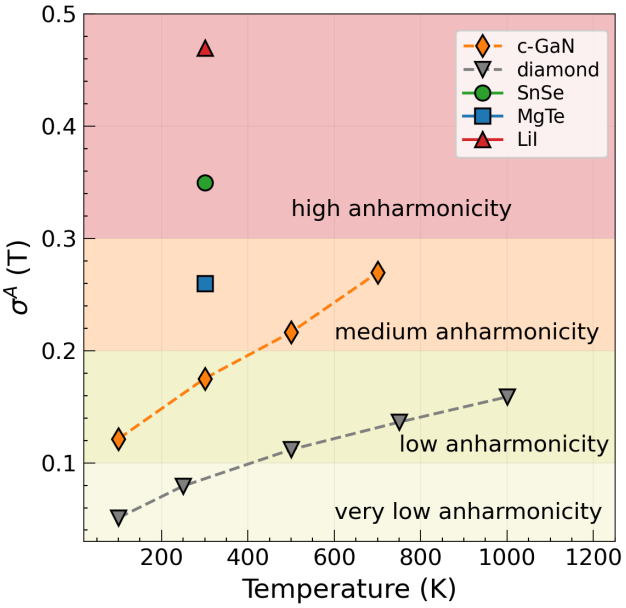

Figure 4.12: Temperature dependence of the anharmonicity measure $\sigma^A(T)$ of diamond and GaN. The comparison is done to the $\sigma^A_{T=300K}$ values for SnSe, MgTe, and LiI reported in [68].

exhibit nearly linear growth of $\sigma^A(T)$ within the temperature range of the study. Utilizing values of $\sigma^A_{T=300K}$ for SnSe, MgTe, and LiI calculated in [68], allows for the conclusion that both materials under our examination exhibit a quite harmonic lattice dynamics. Specifically, diamond is found to be the most harmonic crystal yet investigated, with $\sigma^A_{T=100K}$(C)=0.05 and $\sigma^A_{T=1000K}$(C)=0.15. GaN is characterized by low anharmonicity up to approximately T=400 K, where σ^A_T(GaN) approaches 0.2 value. However, at high temperatures, GaN becomes slightly anharmonic, as evidenced by $\sigma^A_{T=700K}$(GaN)=0.27. In light of these findings, it can be inferred that diamond experiences harmonic lattice dynamics in the whole temperature range of our study, while treatment of anharmonicity in GaN is only necessary at high temperatures. It remains an open question as to whether or not the anharmonicity measure can be utilized as a fingerprint to infer the magnitude of the band gap renormalization – a conclusion that cannot be drawn based solely on the data related to just two materials.

4.5 Comparison with the experimental data

In this section, we compare our results with experimental data. For this comparison, we also collected results for the direct band gap renormalization in diamond. All conclusion related to the indirect band gap renormalization in diamond are also applicable to the direct band gap. Temperature dependencies of the band gap renormalization for GaN and diamond are presented in Fig. 4.13(a) and Fig. 4.13(b, c), respectively. Experimental results are usually fitted using the semi-empirical Varshni formula [267]:

$$E_g(T) = E_g(0) - \frac{\alpha T^2}{T + \beta}. \tag{4.3}$$

where $E_g(0)$ is the energy gap at zero temperature, which can be either direct or indirect, and α and β are constants that are fitted to experimental data. Sometimes other semi-empirical formulas are used [268–271]. We took experimental data for zinc blende GaN from [90]. Experimental data for the direct band gap of diamond is taken from [89]. The data for indirect gap is taken from [271, 272]. Two samples were used for measurements of the direct band gap renormalization in the work [90], thus two dependencies were reported. We note that our results are in agreement with previous theoretical calculations for diamond [52, 182] and GaN [89, 90, 272].

We expect that the inclusion of many-body effects can lead to even better agreement with experimental results. In the case of diamond it was recently demonstrated that the temperature dependence of the band gap renormalization obtained with $G_0 W_0$ is substantially (by 50%) different than the one calculated at the DFT-PBE level of theory [273]. It was also shown for GaAs [223] that inclusion of many-body effects through GW [221, 222] causes an additional 40% increase in the electron-phonon interaction and a subsequent increase in the high-temperature slope of the band gap renormalization. Thus, we assume that the inclusion of many-body correlation effects could lead to slightly steeper temperature dependence of the band gap renormalization in GaN at high temperatures.

Summary of the chapter

In this chapter, we benchmarked the harmonic and fully anharmonic non-perturbative treatment of the band gap renormalization using diamond and zinc blende GaN as test systems. We discussed the computational workflow of the temperature-dependent band gap renormalization calculations. By utilizing the harmonic approximation we inspected numerical aspects of the convergence with respect to the thermodynamic averaging and supercell size. Harmonic forces were used to perform harmonic aiMD in order to test temporal averages. We disentangled nuclear motion and LTE contributions to the band gap renormalization, and discussed both effects separately. The former effect was considered here both in the classical and the quantum limit in the harmonic approximation. The latter effect was shown to have negligible influence in diamond, but tangible contribution to the band gap renormalization in GaN. Eventually, we demonstrated the influence of the anharmonic nuclear dynamics at different temperatures and connected observed trends to the anharmonicity measure. This lead to the formulation of the hypothesis that materials characterized by low anharmonicity measure, i.e., those in which potential energy surface can be described well in the harmonic approximation, feature smaller renormalization caused by the anharmonic contribution. This hypothesis will be tested in the next chapter. Eventually, we noted that obtained results are in agreement with previously published theoretical and experimental data.

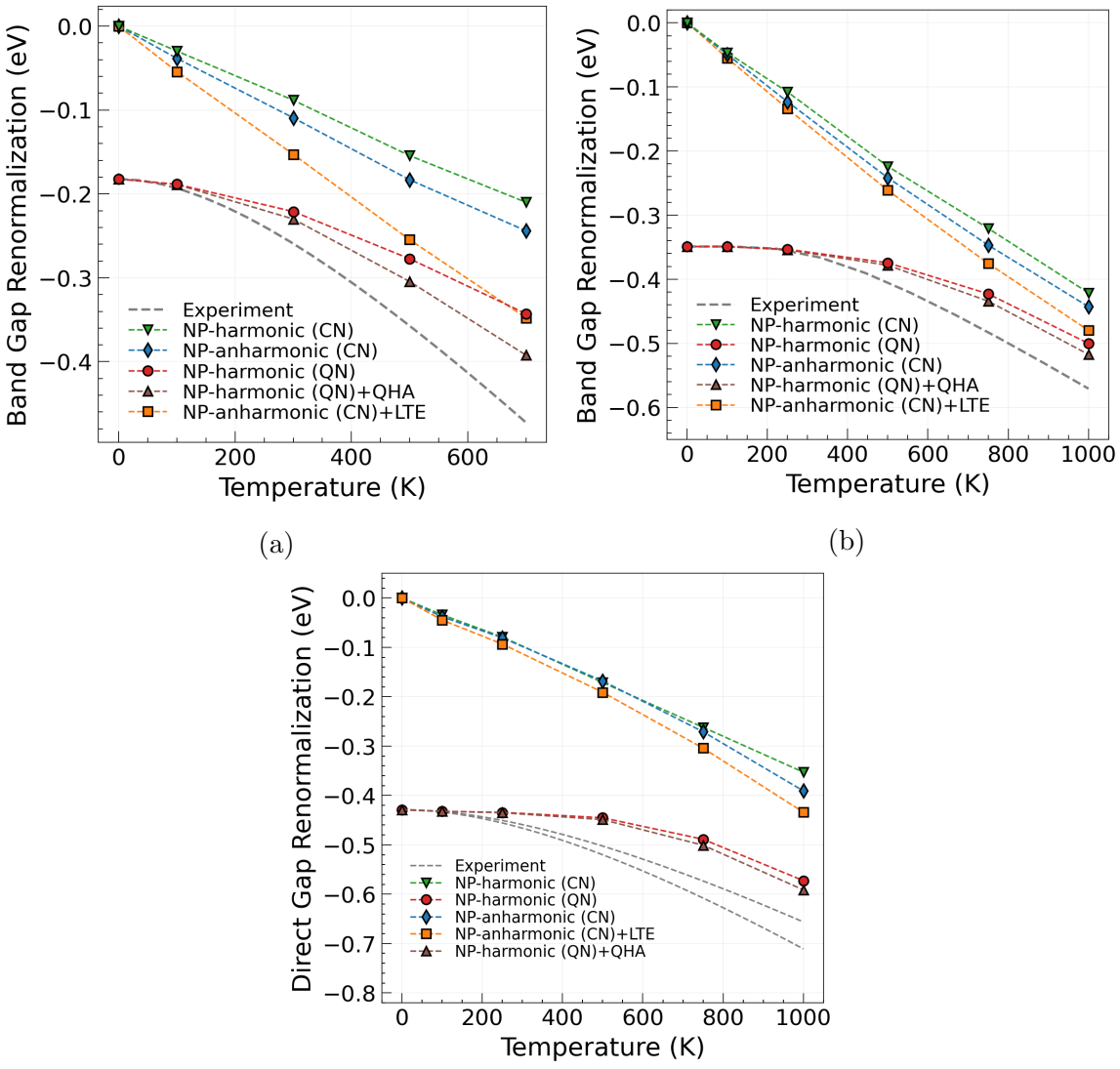

Figure 4.13: Temperature dependence of the band gap renormalization in (a) GaN and (b, c) diamond. Calculations are done with LDA xc-functional and cubic supercell containing 216 atoms. Thermodynamic averaging is done using 50 samples for GaN and 100 samples for diamond. Non-perturbative (NP) harmonic treatment is applied taken into account classical (CN) and quantum (QN) statistics for the nuclear motion. NP anharmonic treatment is done via aiMD simulations. Polar correction is included in both classical and quantum limits. Experimental data for GaN and diamond is taken from [86–88, 90]. Experimental data for the indirect band gap renormalization of diamond is taken from [271, 272], and for the direct band gap renormalization from [89].

Chapter 5

Quantifying the role of different contributions to the band gap renormalization at finite temperatures

The strength of electron-phonon interactions (EPI) in solids is frequently quantified based on the zero-point renormalization of the band gap (ZPR), which these interactions cause [12, 15–17, 21, 94, 182, 207, 213–216]. Although pioneering first principles calculations of the temperature-dependent band gap renormalization, caused by the EPI, appeared long time ago [59], the wider exploration of the temperature's influence on the band gap renormalization is a relatively recent trend [16, 39, 52, 85, 228, 246, 273]. Usually, published works rely on the Allen-Heine-Cardona formalism, which can be applied to harmonic materials like silicon or diamond straightforwardly, but can not be applied without extra caution for materials in which the harmonic ansatz for phonons is not applicable, for example, some perovskites [18, 85]. It was recently shown that a sufficient portion of materials is quite anharmonic already at room temperature, and the number of anharmonic materials increases with temperature [68]. However, the influence of the lattice dynamics anharmonicity on the band gap renormalization at finite temperatures has not been studied in detail, yet.

The band gap value is also affected by the thermal lattice expansion (or contraction). In certain cases, the band gap change due to the LTE is negligible. For example, in diamond the gap decreases by only 30 meV, when the temperature increases from 0 K to 1000 K (see discussion in Chapter 4). For the same temperature range the renormalization of the band gap due to the EPI is larger by one order of magnitude. On the other hand, in some materials LTE can cause tangible changes of the band gap value, for example, in the case of $SrTiO_3$ the gap opens by ≈200 meV at 1000 K [85]. Despite the widespread interest in evaluating the renormalization of the electronic band structure, a comprehensive study of the LTE influence at different temperatures is still missing (the influence of the zero-point lattice expansion was recently evaluated in [255]).

The methodology discussed and benchmarked in the previous chapters enables us to explore the microscopic origin of the band gap renormalization for both harmonic and an-

harmonic materials on equal footing. Thus, in this chapter, we investigate the impact of the EPI and the LTE on the band gap renormalization in 52 binary compounds. These materials have different structural types, including rock salt, zinc blende, wurtzite, fluorite, and anti-fluorite, exhibit a diversity of band gaps, bonding types (ionic and covalent), atomic masses, and lattice anharmonicity. We disentangled the contributions of the EPI and the LTE, quantified the role of different effects, and, in particular, showed the impact of the anharmonic effects. For the major portion of materials, we calculated the band gap renormalization at room temperature. For selected materials, an in-depth analysis is performed to clarify the general mechanisms governing band gap renormalization across a broad temperature range. We utilized aiMD trajectories available in the NOMAD repository [274]. [1] The computational details for the DFT calculations and the structural parameters of the materials under study are presented in Appendix C.

5.1 Zero-point renormalization of the band gap

Prior to carrying out an evaluation of the band gap renormalization at finite temperatures, it is imperative to determine the ZPR of the materials, used in our work. Benchmark calculations for diamond and zinc blende GaN was already conducted in Chapter 4 to validate the method. In the current section, a comprehensive examination of a wider range of materials is done. The calculations of the ZPR are done in the harmonic approximation, by generating uncorrelated samples in the classical and quantum limit (see details of such calculations in Chapter 4). First of all, this allows to further test the descriptors mentioned above on a larger set of materials. Secondly, these calculations allow us to check that a satisfactory description of the ZPR can be obtained before progressing to calculations at finite temperature. To maintain consistency with previously published data [94,182,213], 23 materials with rock salt structures and 9 compounds with zinc blende structures have been selected for calculations. The comparison between our results and literature data is shown in Fig. 5.2(a).

The ZPR values for the compounds with rock salt structure range from -5 meV for CaTe to -558 meV for LiF. This significant ZPR in LiF has been previously reported in prior computational studies [94, 273]. A comparison between the ZPR values obtained in the present study and those reported in [94], reveals a mean absolute error (MAE) of 8 meV and maximal difference is 22 meV as observed for CsF. It is worth noting that both studies employed the FHI-aims package, however, the calculations performed in [94] utilized the Perdew-Burke-Ernzerhof (PBE) xc-functional within the frozen phonon framework. The small discrepancy between the results may be attributed to differences in the methodologies employed, including the level of theory and the structural parameters of the materials used in the analysis.

The ZPR values of compounds with zinc blende structure range from -12 meV for CdTe to -92 meV for GaN. Tab. 5.1 presents a comparison of our results with the literature data for several compounds with zinc blende structure. We compared our results with those reported in [94, 182] and obtained a MAE of 7 meV and 6 meV, respectively. The largest deviation was observed in the case of GaAs, when compared to the data presented in [182]. The ZPR

[1] NOMAD dataset DOI:dx.doi.org/10.17172/NOMAD/2020.06.25-1.

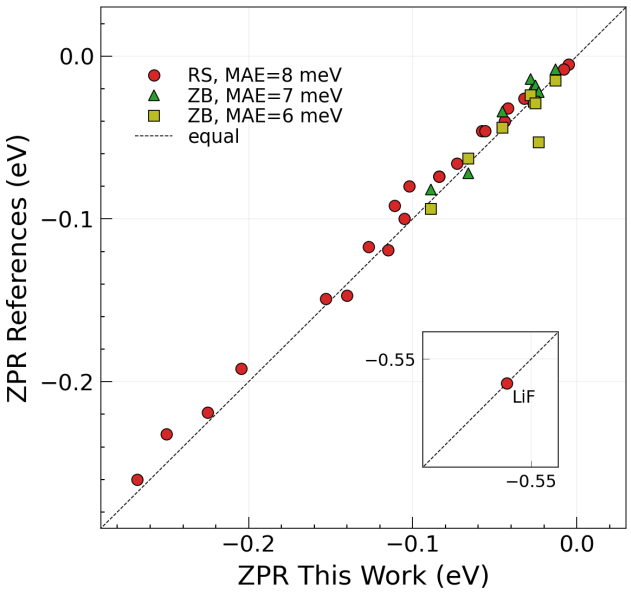

Figure 5.1: Comparison between ZPR in this work and references [94,182]. The inset shows the ZPR in LiF. Data for rock salt structures is shown as red disks. The comparison of our results for zinc blende structures is shown using olive squares once the comparsion is done with [182], and using green triangles for the comparison with [94].

of GaAs is -22 meV in our calculations, which is in agreement with the results reported in [94, 223], but differs from the ZPR value of -53 meV reported in [182, 213]. Given that the ZPR of GaAs was calculated to be -32 meV in another study [212], and that the HSE06 xc-functional was used for GaAs in [182], we consider our results for GaAs to be acceptable. We also note that the polar correction has negligible influence on the gap renormalization in GaAs [212].

Table 5.1: ZPR of the band gaps for materials with zinc blende structure. Reference data is taken from previous computational works [182] (first number), [213] (second number), and [94] (third number). The references for experimental values are explicitly noted. All values are in meV.

Material	This Work	Previous Works	Experiment
ZnS	-45	-44, -88, -34	-105 [275], -78 [264]
ZnSe	-25	-28, -44, -18	-55 [264], -64 [12]
ZnTe	-27	-24, -22, -14	-40 [264]
CdS	-25	-29, -70, -18	-62, -34 [264]
CdTe	-12	-15, -20, -8	-16 [264]
AlAs	-66	-63, -74, -72	-50 [264]
GaAs	-22	-53, -53, -22	-57±29 [276], -90 [12]
		-32 [212], -23 [223]	
GaN	-89	-94 [182], -82 [94]	

Experimentally, the ZPR is usually determined by fitting the measured band gap renor-

Table 5.2: Coefficient of determination R^2, obtained by a linear least-square regression between ZPR and different descriptors mentioned in the main text.

Materials Set	$\hbar\omega_{\max}$	$\Delta a/a$	M_{AB}^{-1}	$(M_{\mathrm{A}} \times M_{\mathrm{B}})^{-1/4}$
Rock Salt	0.55	0.68	0.84	0.79
Zinc Blende	0.86	0.18	0.82	0.86
Wurtzite	0.65	0.07	0.54	0.8
Whole set	0.38	0.70	0.83	0.81

malization at finite temperatures or by performing experiments with the isotopic mass derivatives of the gap [12]. These procedures are subject to various sources of uncertainty, as discussed in detail in [12]. Therefore, caution should be exercised when comparing experimental values between each other and with calculated values. Actually, in the case of first principles calculations an additional correction to the calculated values of the ZPR should be applied in polar materials [93, 213]. Moreover, it was recently shown that zero-point lattice expansion can cause additional renormalization reaching from 20% to more than 80% of the band gap ZPR [255].[2] In this chapter, we neither included polar correction, nor considered zero-point lattice expansion. However, we note that the results of our study are in agreement with previous computational works [94, 182, 213], which suggest that the obtained values of the ZPR are reliable.

The evaluation of the band gap ZPR is a complex subject, as demonstrated by the numerous debates surrounding its experimental and calculated values [12, 13, 17, 207, 213, 277]. Understanding and explaining trends for the observed ZPR values in different materials has been an active area of research [12, 17, 21, 94, 182, 207, 213]. The difference in ZPR among various materials was described based on the difference in the electronic structure [207] and on vibrational arguments [17,21]. In the former case, it was argued that the difference among ZPR in various materials can be attributed to the differences in the electronic structure of these compounds. In particular, this hypothesis was used to explain the substantial difference between the ZPR in diamond (-336 meV [207]) and silicon (-53 meV [207]). It is assumed that *p*-core states in Si screen the atomic potential more effectively than it is screened in diamond and thus, the ZPR in diamond is larger [207]. The DFT calculations performed in [17] for diamond, silicon, and silicon carbide showed that the microscopic origin of the different ZPR in these materials is related not only to the electronic structure of elements forming the crystal, but to the different bonding and the distortion of the bonds in these compounds.

Vibrational approach for the ZPR description is based on the assumption that the magnitude of the ZPR is related to the magnitude of the atomic vibrations. This assumption is reinforced by experimental works devoted to assessing the impact of the isotopic mass on the ZPR values [13, 207, 270, 278]. It was shown that the amplitude of atomic vibrations scales inversely with the square root of the isotopic mass, indicating that heavier isotopes have weaker EPI [207]. Consequently, it was assumed that there should be a correlation between the vibrational frequencies and the magnitude of the ZPR [12, 13, 207]. Fig. 5.2(a) shows the

[2] In the study [255], in total, 22 materials with cubic and wurtzite structural types were used.

correlation between the highest phonon frequency and the calculated values of the ZPR for the subset of materials, which we are going to study. As was previously observed in [182] for zinc blende compounds the dependence is almost linear. The coefficient of determination R^2 equals 0.86 for zinc blende compounds. However, some materials with rock salt structure follow this trend only qualitatively (R^2=0.55). For example, KF and LiF, do not obey the linear scaling. In general, the linear least-square regression shows a rather non-linear dependence (R^2=0.38) between the ZPR and the highest phonon frequency, as demonstrated in Tab. 5.2.

An intuitive argument that the value of the ZPR should be related to the amplitude of the nuclear motion lead to the ansatz that the correction of the gap should be proportional to the ratio $\Delta a/a$, where a is the bond length of the material[3] and Δa denotes the zero-point atomic displacement [21], which can be derived using a quantum harmonic oscillator model:

$$\Delta a = \sqrt{\frac{\hbar}{M\omega_{\mathrm{LO}}}} \tag{5.1}$$

Here, M denotes the average mass of ions in the unit cell and ω_{LO} denotes the longitudinal optical phonon frequency. This assumption implies that the ZPR magnitude is large when the magnitude of the atomic displacement is significant compared to the bond length. The original work demonstrated a non-linear proportionality between the suggested descriptor and the ZPR of the band gap [21].[4]

We expanded the number of tested materials and modified the descriptor defined in Eq. (5.1) slightly. Specifically, the accurate determination of ω_{LO} requires to treat LO-TO splitting, which can be done by applying a non-analytical correction as discussed in Sec. (2.1). However, this would require the calculation of the Born effective charges and the high-frequency dielectric constant for all materials in the set. We evaluated the amplitude of atomic displacement using the maximal phonon's frequency ω_{max} instead of the frequency of the LO phonon ω_{LO}. This modification is valid, based on our inspection of the phonon dispersion of the materials from our set using the database of phonon calculations [279]. As shown in Fig. 5.2(b), the descriptor introduced in Eq. (5.1) indeed has some qualitative predictive power – materials, with larger atomic vibrations tend to have larger ZPR. The dependence is, however, non-linear. Calculations of a linear least-squares regression for the set of materials including diamond, zinc blende, rock salt, and wurtzite compounds yield R^2=0.7. Tab. 5.2 contains results of the linear fitting for each set of materials.

According to the lattice dynamics equations introduced in Sec. (2.1) the eigenfrequencies of phonons are inversely proportional to the masses of the atoms in the unit cell. Following this observation, the utilization of the inverse average mass of the atoms in the unit cell was used as a descriptor to describe ZPR trends [182] for 18 semiconductors with zinc blende structure. It was argued that the band gap renormalization is inversely proportional to the mass of the constituting ions. That conclusion was later challenged in the work [94], where the inverse fourth root of the masses of constituting elements was used as a descriptor. We

[3]The bond length was defined as a distance between non-equivalent atoms in the unit cell. In the case of wurtzite structures, we used the bond length value averaged over distances between non-equivalent atoms of different elements.

[4]Work [21] used a set of 9 semiconductors: Ge, Si, C, InSb, CdTe, ZnTe, ZnSe, ZnS.

illustrated the dependence of the ZPR on the inverse average mass of the constituting ions as proposed in [182] in Fig. 5.2(c), and the inverse fourth root of the masses as suggested in [94] in Fig. 5.2(d). The values of ZPR are indeed found to correlate with these mass-based descriptors. In the case of the linear least-squares regression fit between the ZPR and inverse average atomic mass the R^2=0.83, while once the inverse fourth root of the masses is used R^2=0.81.

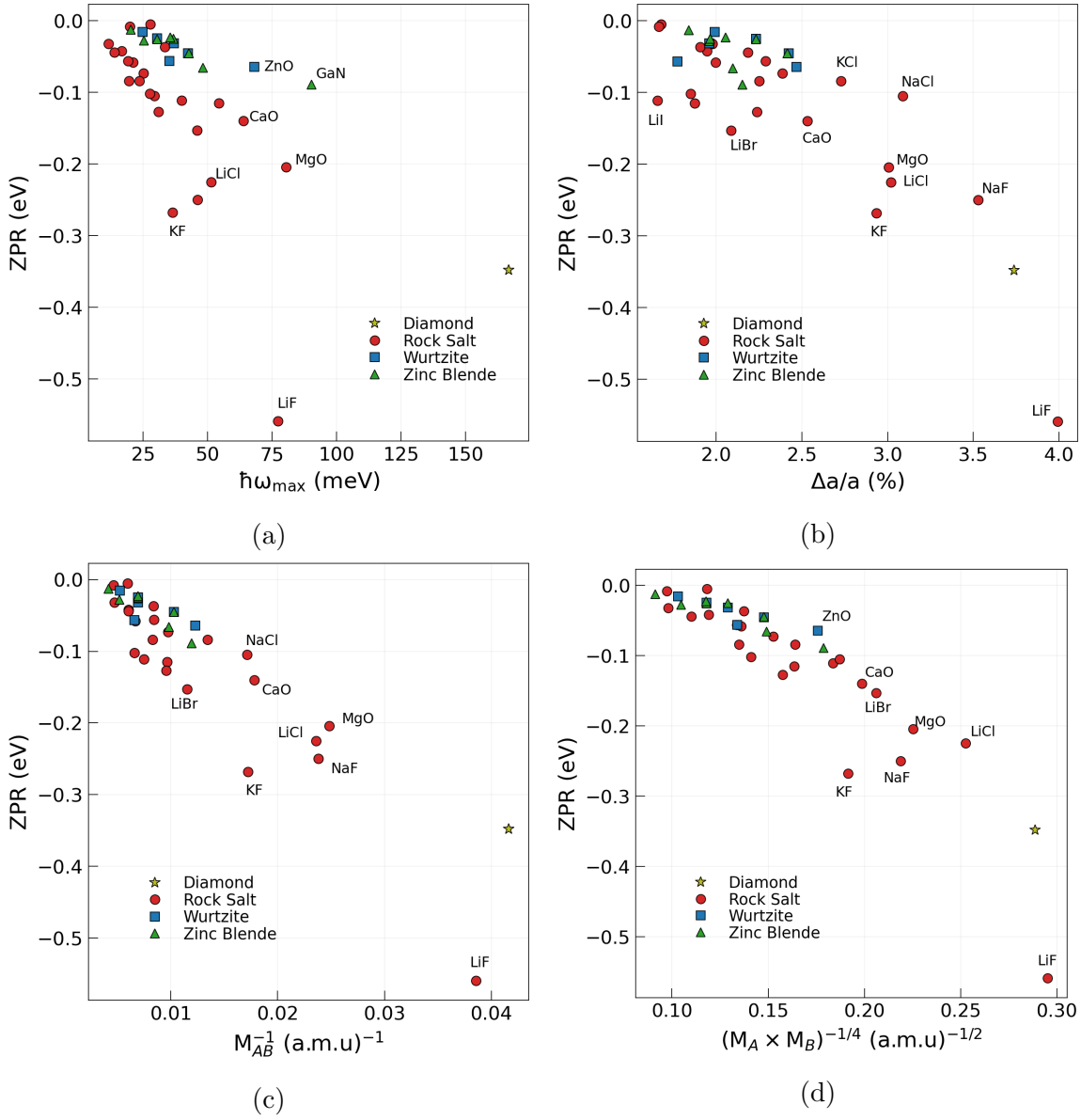

Figure 5.2: The dependencies between ZPR of the band gap and (a) largest phonon frequency, (b) largest atomic displacement normalized by interatomic bond length, (c) inverse average mass of atoms in the unit cell, (d) inverse forth root of the multiplication of the atomic masses.

The breakdown of the mass rule reported in [94], highly likely can be attributed to the inclusion of the Fröhlich polar correction. This correction can indeed constitute a significant contribution to the ZPR, but we note that in the work [94] an approximation introduced in [93]

and described by Eq. (3.31) was used for the polar correction evaluation. This approach is highly sensitive to the calculated polaron constant value (see the discussion in Chapter 4), and it is also challenging to apply it for the correct treatment of the anisotropic bands [93]. The reliable evaluation of the polar correction can only be based on more involved calculations [43, 213], which go beyond the scope of this thesis.

In summary, the evaluation of the ZPR serves as a starting point. Since our results agree well with the previously published data, we can proceed to the evaluation of the band gap renormalization at finite temperatures.

5.2 Electron-phonon interactions: quantum and classical treatment of the nuclear motion

In this section, we examine the impact of the nuclear motion on the band gap renormalization in the classical and quantum limits by performing calculations within the harmonic approximation. To this end, we generate configurations with nuclear displacements consistent with the canonical ensemble at a temperature of 300 K, as outlined in Sec. 2.1 and works [69, 180]. In addition to the materials included in the ZPR benchmark (rock salt, zinc blende, wurtzite-type structures), we also consider compounds with a fluorite and antifluorite structures. [5]

To start with, we calculate the band gap renormalization at 300 K by taking into account the quantum statistics of the nuclei. It has been previously proposed [12, 93] that the band gap renormalization should be in the range of 2-4 k_BT, which is indeed the case for some materials, such as GaAs, ZnO, and CdTe. However, Fig. 5.3 reveals that, in addition to the well-known case of diamond [207], which exhibits a relatively large renormalization of the band gap (-350 meV) at room temperature, there are compounds that feature even larger changes of the gap. For instance, the band gap renormalization in LiF at room temperature is around -600 meV, primarily due to the ZPR. Notably, the atomic mass-based descriptor previously utilized to describe ZPR has only limited validity at room temperature. As shown in Fig. 5.4, the inverse averaged atomic mass can reasonably describe the trends in the band gap renormalization for materials with the zinc blende structure, but not for the rest. A linear least-squares regression fitting yields R^2=0.93 for zinc blende materials and R^2=0.44 once the whole set is fitted. [6]

The comparison between band gap renormalization due to the nuclear motion calculated using quantum and classical limits is shown in Fig. 5.5(a). The vibronic renormalization in all materials is larger once nuclear motion is treated quantum-mechanically instead of classically, which can be attributed to the major contribution coming from the ZPR. The wurtzite and zinc blende structures feature rather small absolute values of the renormalization as was observed also in the quantum limit. However, some compounds such as diamond and Li_2O have much smaller values of the renormalization in the classical limit rather than in the quantum limit. Our calculations have revealed that the relationship between gap renormalization in the classical and quantum limits can be explained through the utilization of the highest

[5] We will call all these structures fluorite-type in the rest of the text for convenience.

[6] For wurtzite compounds R^2=0.036, for rock salt compounds R^2=0.45, for fluorite compounds R^2=0.06.

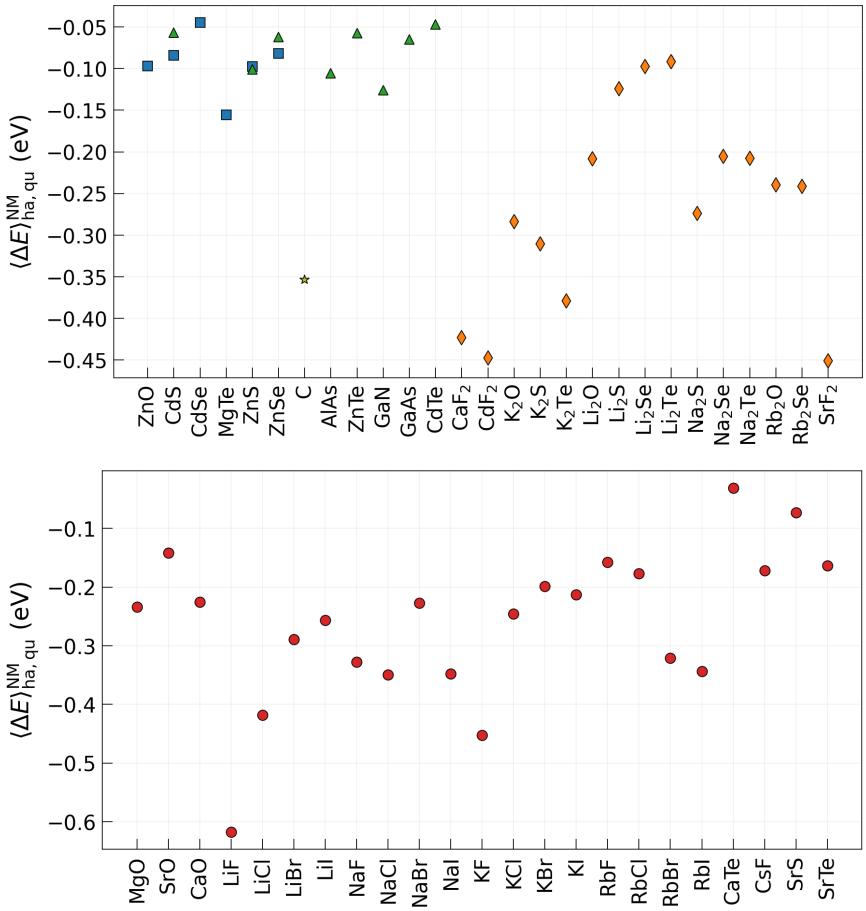

Figure 5.3: Band gap renormalization at room temperature due to the nuclear motion. The calculations are done in the harmonic approximation using quantum statistics for the nuclear motion.

phonon frequency. The studies related to the quantum nuclear effect [192, 193], commonly assert that materials comprised of lighter atomic masses exhibit a substantial quantum effect. As lighter atomic masses correspond to phonons of higher frequency, the highest frequency in the phonon spectrum can potentially serve as a simple descriptor. Fig. 5.5(b) illustrates the correlation between the highest phonon energy $\hbar\omega_{\max}$ and the ratio of band gap renormalization caused by nuclear motion in the classical and the quantum limits. A linear least-squares regression fitting yields R^2=0.8. Our sample materials encompass a diverse range of atomic masses, thus frequencies range from a few to tens of THz. In those materials where a maximum phonon energy $\hbar\omega_{\max} \approx$ exceeds 50 meV a contribution from the inclusion of quantum effects cause substantial renormalization of the gap. Materials in which 20 meV $< \hbar\omega_{\max} <$ 50 meV display moderate to low difference between quantum and classical treatment. In materials with $\hbar\omega_{\max} <$ 20 meV the treatment of the nuclear vibrations in the classical and in the quantum limits is approximately equivalent.

5.3 Electron-phonon interactions: harmonic and fully anharmonic treatment of the nuclear motion

In this section, we present an evaluation of the impact of a fully anharmonic treatment of the potential energy surface (PES) on band gap renormalization. We compare between the calcu-

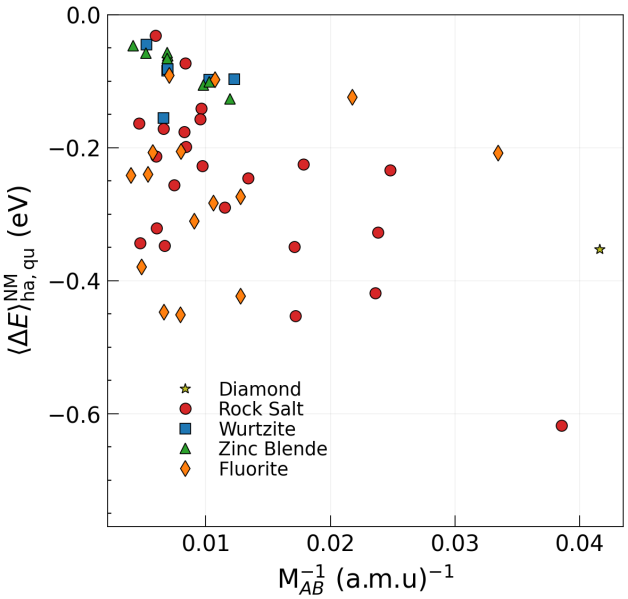

Figure 5.4: The dependence between band gap renormalization at room temperature and the inverse average mass of atoms in the unit cell.

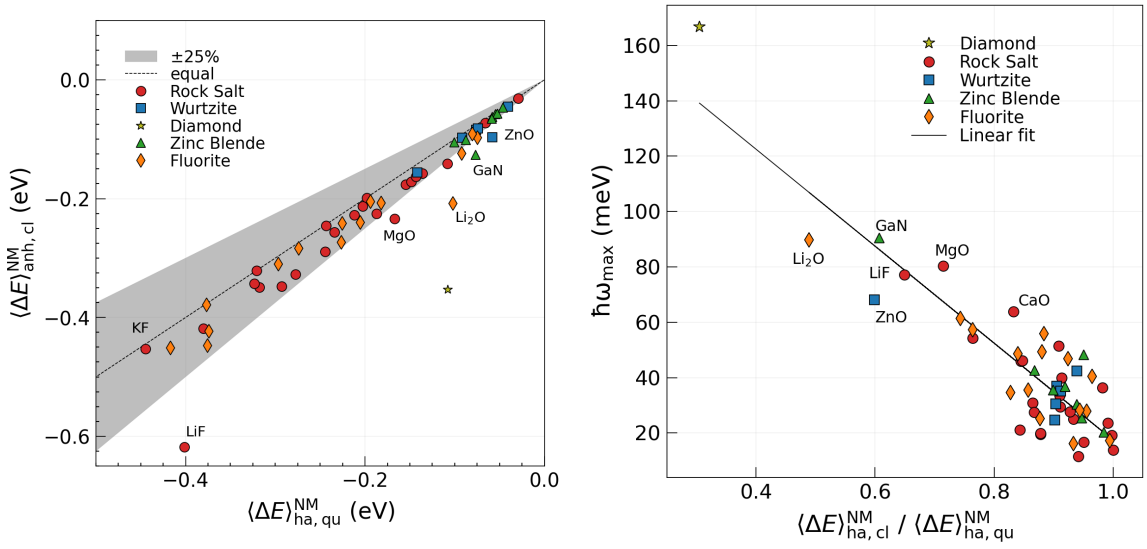

(a) (b)

Figure 5.5: (a) Relation between the band gap renormalization due to the nuclear motion calculated in the harmonic approximation using quantum and classical limits. (b) The dependence between the largest phonon energy and the ration shown in plot (a).

lations performed using the harmonic approximation and the fully anharmonic calculations performed using aiMD (see details for the aiMD trajectories calculations in Appendix C). As depicted in Fig. 5.6, the inclusion of the PES anharmonicity results in a larger band gap renormalization in all materials studied. In most cases the difference between the band gap renormalization calculated in the harmonic approximation and fully anharmonically does not exceed 20%. This additional renormalization ranges from a few meV to -62 meV in the case of LiI. The case of diamond is particularly noteworthy, since diamond is considered to be very harmonic (see Chapter 4 and [68]) and the inclusion of anharmonicity leads to just an extra -20 meV renormalization. However, this is larger than the additional renormalization observed in most wurtzite structures and zinc blende structures, except GaN, which experiences a similar additional renormalization. It is also worth mentioning that most of the compounds that exhibit a significant renormalization due to the inclusion of anharmonicity have rock salt structures. Compounds with fluorite structures, on the other hand, exhibit intermediate behavior between rock salts and compounds with wurtzite and zinc blende structures.

Our hypothesis is that the difference between fully anharmonic calculations and calculations in the harmonic approximation correlates with the average nuclear displacement in the material. The logic behind this hypothesis is that materials with larger atomic displacements should exhibit greater anharmonicity as the atoms would move outside of the region of validity for the harmonic potential. To test this, we calculated the root-mean-squared atomic displacements along aiMD trajectories, normalized by the bond distance, as described in Sec. 5.1. Fig. 5.7(a) shows the dependence between the band gap renormalization caused exclusive by PES anharmonicity ($\langle \Delta E \rangle^{\mathrm{NM}}_{\mathrm{anh,cl}}$ - $\langle \Delta E \rangle^{\mathrm{NM}}_{\mathrm{ha,cl}}$) and the atomic-displacement descriptor.

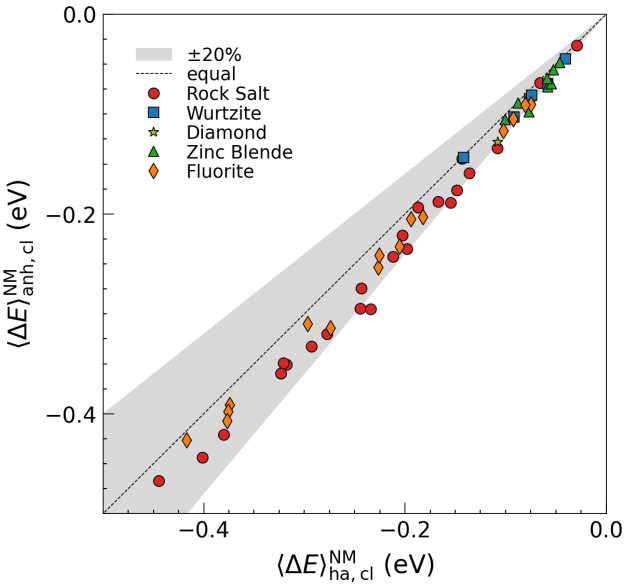

Figure 5.6: Relation between the band gap renormalization due to the nuclear motion calculated in the harmonic approximation in the classical limit and fully anharmonically using aiMD.

Our investigation of the impact of anharmonicity on the band gap renormalization in diamond and GaN, presented in Chapter 4, has revealed that the influence of anharmonicity

is negligible in those materials. The description of the observed trends was done by utilizing the anharmonicity measure σ^A, introduced in Sec. 2.3 following work [68]. In this respect, we sought to examine the correlation between the σ^A and the anharmonic contribution to the band gap renormalization across the whole set. The results of this examination are depicted in Fig. 5.7(b). Notably, the gap renormalization caused exclusively by anharmonicity in KF and GaN are nearly identical, despite the fact that the anharmonicity measure in KF is twice larger that in GaN.

5.4 Exploring the role of thermal expansion

In this section, we aim to quantify the magnitude of the LTE influence on the band gap changes. The unit cell volumes as a function of temperature can be calculated either approximately using the QHA method or by renormalizing the internal pressure extracted from the aiMD simulations, as described in Sec. 2.4, which is more accurate. Therefore, we will proceed with our calculations based on the renormalized volumes obtained from aiMD simulations, i.e., we calculate band gap for the equilibrium zero temperature volume and then recompute the band gap for the expanded unit cell – the difference between obtained values corresponds to the impact of the LTE on the band gap change. Fig. 5.8 shows the magnitude of the LTE influence on the band gaps changes at T=300 K. The absolute change of the band gap in the case of wurtzite and zinc blende compounds presented in our set does not exceed 50 meV. In the case of GaAs and GaN, the LTE causes an additional change in the gap of approximately 50 meV, in agreement with literature data [212, 280]. In some materials with rock salt structure, for example SrO and CaO, the band gap hardly changes, while in other

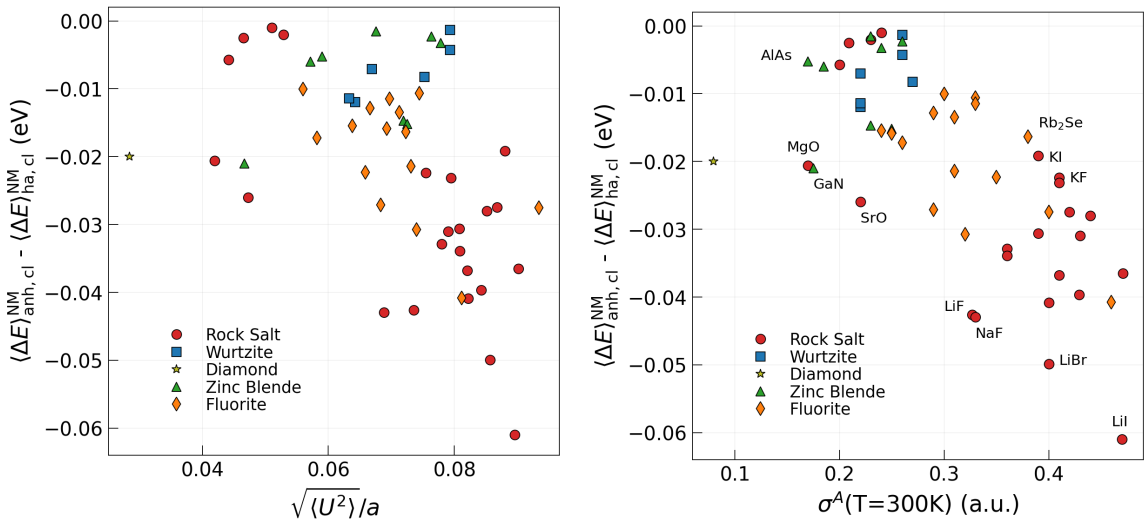

(a) (b)

Figure 5.7: Relation between the band gap renormalization, caused exclusively by the anharmonic part of the nuclear motion and (a) the root-mean-squared atomic displacements at room temperature normalized by the bond length between atoms in the unit cell; (b) anharmonicity measure extracted from the aiMD trajectories.

rock salt compounds the change constitutes hundreds of meV. For example, in the case of LiF the band gap changes by -318 meV only because of the LTE. In the case of materials with fluorite structure, the band gaps change in the range from 25 meV in the case of Li_2X (X=S, Se, Te) to around -150 meV in the case of K_2O and Rb_2O, which also constitutes 8 % and 10 % of the zero temperature band gaps in these materials, respectively.

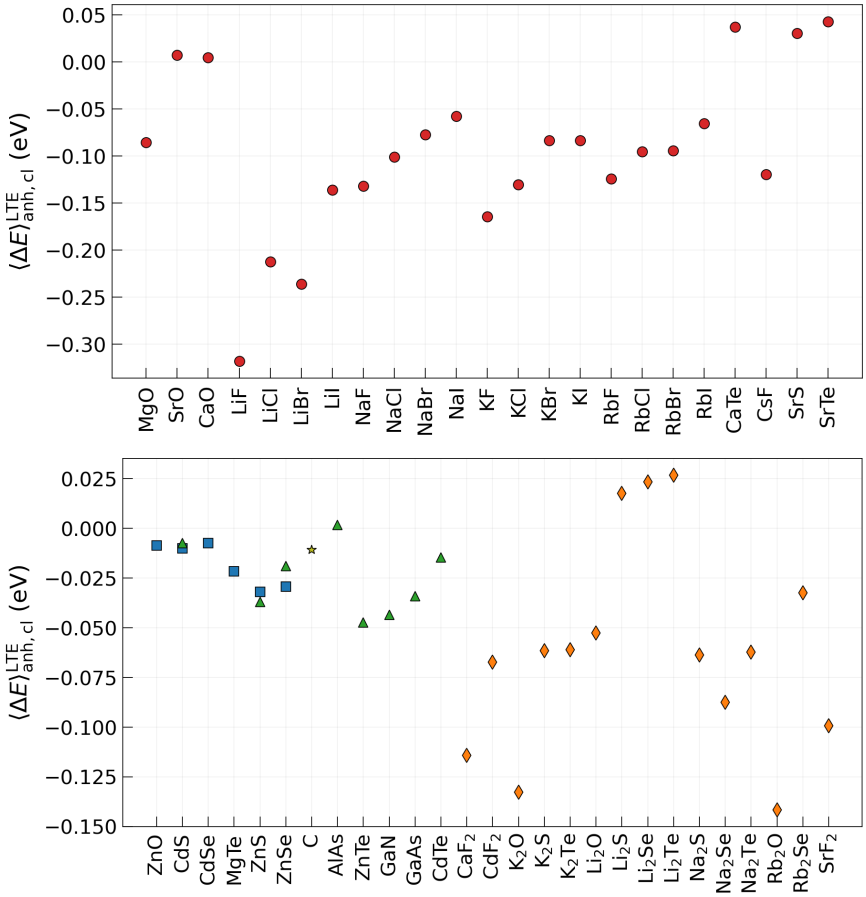

Figure 5.8: Band gap renormalization caused by the lattice thermal expansion at T=300 K.

The relationship between changes in the gap and relative changes in volume with temperature is shown in Fig. 5.9(a). Compounds with zinc blende and wurtzite structures exhibit minimal changes in both volume and band gap, with changes in volume being within 1 %. In contrast, rock salt and fluorite-type compounds display larger variations in volume, up to 5 %, and significant renormalization of the band gap. A comparison of the band gap renormalization caused exclusively by the nuclear motion calculated fully anharmonically and exclusively by the LTE is illustrated in Fig. 5.9(b). This comparison reveals that for some materials, for example LiF and LiBr, the band gap change caused by LTE constitutes almost a half of the gap renormalization caused exclusively by the nuclear motion. Although, for most of the materials, main contribution to the band gap renormalization at finite temperatures is regulated by the electron-phonon interactions, accurate calculations of the band gap renormalization require to take the LTE influence into account.

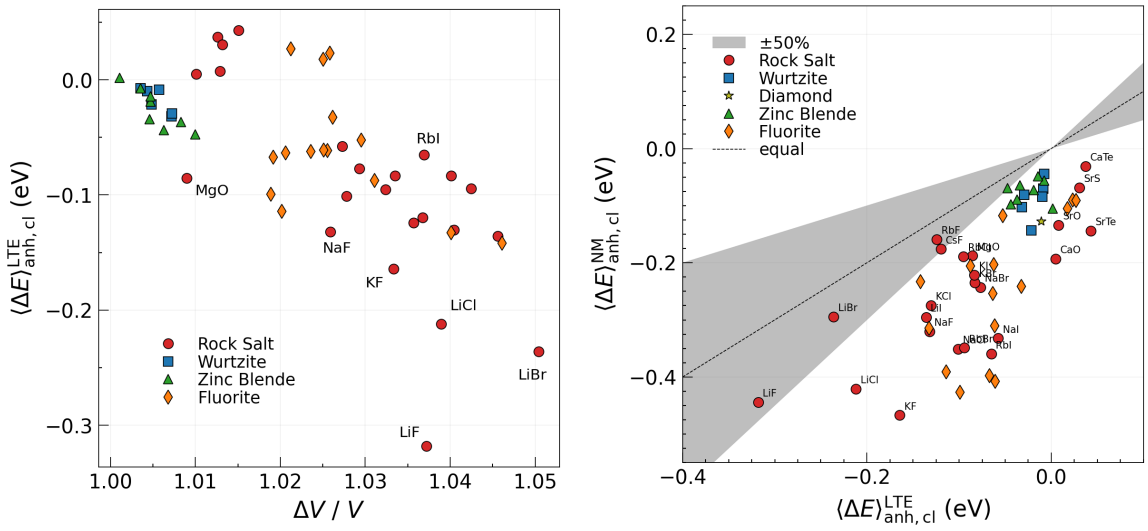

(a) (b)

Figure 5.9: (a) Band gap renormalization caused by the LTE with respect to the changes in volume once the material is heated to T=300 K. (b) The comparison between the band gap renormalization caused by LTE and nuclear motion calculated via aiMD.

5.5 The role of anharmonicity in the band gap renormalization

Earlier, it was emphasized that the impact of anharmonic effects on the band gap renormalization can be potentially evaluated by utilizing the anharmonicity measure, which is employed

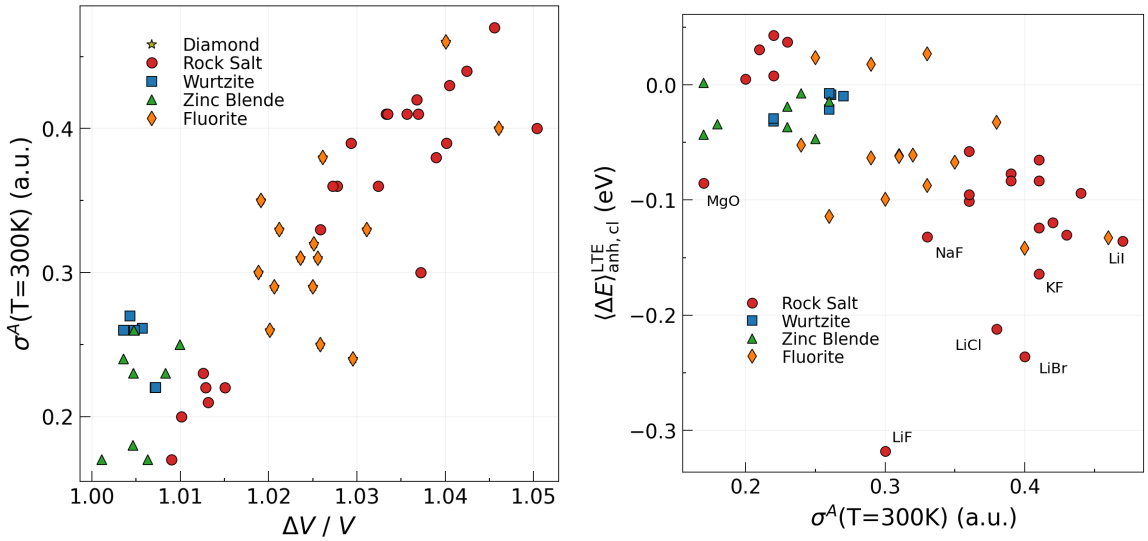

(a) (b)

Figure 5.10: (a) Relations between anharmonicity measure and changes in volume once materials are heated to T=300 K. (b) Relations between band gap renormalization caused by LTE at T=300 K and the anharmonicity measures $\sigma^A(T)$.

to categorize materials into harmonic and anharmonic in terms of their lattice dynamics [68]. Thermal expansion is considered to be an anharmonic effect, since under the harmonic approximation, the thermal expansion coefficient is zero. Fig. 5.10(a) illustrates the correlation between the anharmonicity measure σ^A at T=300 K and the volume changes experienced by materials when subjected to heating. We observe that anharmonic materials tend to have larger volume expansion. This comparison reveals that materials tend to clusterize based on their crystalline structure, with wurtzite and zinc blende structures being less anharmonic than rock salts, and fluorite-type structures falling in between.

Fig.5.10(b) depicts the correlation between the band gap renormalization caused exclusively by the LTE and the anharmonicity measure σ^A at T=300 K. We found that LiF has a band gap renormalization that is twice as large as LiI, even though LiI is more anharmonic. In a similar way, MgO, which is considered a rather harmonic material, experiences a band gap renormalization that is of the same magnitude as RbBr, which is twice as anharmonic according to its σ^A. While some correlation between an increase in anharmonic measure and band gap renormalization is apparent, this relation appears to be non-linear.

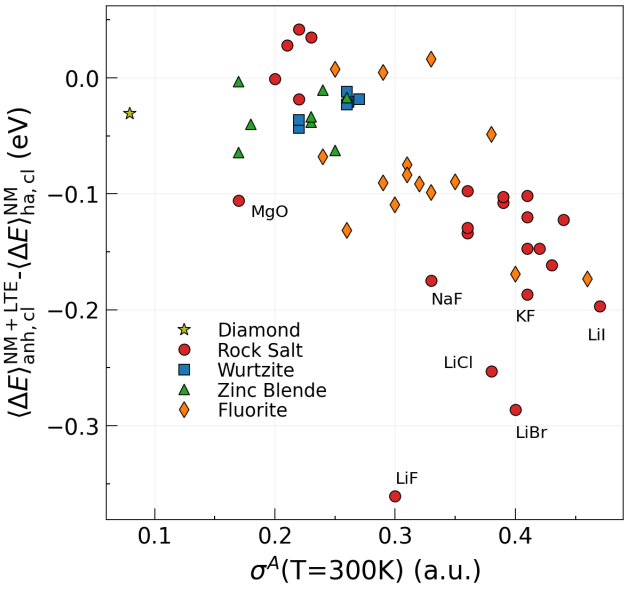

Figure 5.11: Relations between the band gap renormalization caused exclusively by lattice and nuclear dynamics anharmonic effects and anharmonicity measures at T=300 K.

In order to assess the overall impact of anharmonic effects on the band gap, we must consider the sum of the band gap renormalization contributions resulting from the fully anharmonic nuclear motion $\langle\Delta E\rangle^{\mathrm{NM}}_{\mathrm{anh,\,cl}}$ and lattice thermal expansion $\langle\Delta E\rangle^{\mathrm{LTE}}_{\mathrm{anh,\,cl}}$, while excluding the contribution from the harmonic nuclear motion $\langle\Delta E\rangle^{\mathrm{NM}}_{\mathrm{ha,\,cl}}$. The comparison between $\langle\Delta E\rangle^{\mathrm{NM+LTE}}_{\mathrm{anh,\,cl}} - \langle\Delta E\rangle^{\mathrm{NM}}_{\mathrm{ha,\,cl}}$ and the anharmonicity measure is presented in Fig. 5.11. It is apparent that the inclusion of anharmonic effects results in a substantial renormalization of the band gap in some materials, with LiF being a prime example, where almost half of the gap renormalization is attributed to anharmonic effects. The contribution coming from anharmonicity is anticipated to grow with temperature, as anharmonicity has been observed to increase with temperature [68]. It is worth noting that MgO and LiF have previously

Table 5.3: ZPR of the band gaps in MgO, LiF, and LiI. All values are reported in meV.

Material	This Work	Previous Works
MgO	-205	-196 [281], -210 [273]
		-281 [283], -192 [94]
LiF	-559	-523 [281], -559 [94]
		-460 [273]
LiI	-110	-92 [94]

been identified as materials where a proper treatment of anharmonic effects on the band gap renormalization is crucial [213, 281, 282].

We conclude by noting that there is a correlation, albeit non-linear, between lattice anharmonicity and the band gap renormalization at room temperature. Solids that exhibit higher levels of anharmonicity also demonstrate higher renormalization due to anharmonic effects and vice versa. In order to gain a deeper understanding of the physical processes that govern this relationship, further investigation is necessary. For this purpose, the lattice dynamics and electronic structure properties of MgO, LiF, and LiI will be examined over a wider temperature range.

5.6 Band gap renormalization in MgO, LiF, and LiI

In this section, we examine the temperature-dependence of the band gap in MgO, LiF and LiI. We start with an elementary comparison of the ZPR values obtained in our work and literature references. Our results are presented in Tab. (5.3) and are found to be in agreement with previously published data [94, 273, 281, 283]. The deviations from ZPR values reported in various studies can be attributed to various factors, including anharmonic corrections to the LO phonon frequency, approximations used for the Fröhlich polar correction, and the reliability of the DFT xc-functionals, as discussed in [213]. It is also important to note that these ZPR values do not take into account the Fröhlich polar correction. This correction is significant for MgO with a value of -137 meV [213]. However, as was already pointed out above, an accurate treatment [43, 213] of the Fröhlich polar correction is beyond the scope of this thesis.

As the ZPR results of our work appear to be in reasonable agreement with the relevant literature, we can proceed with the exploration of the temperature-dependence of the band gap renormalization. The thermodynamically averaged spectral function of MgO calculated in the harmonic approximation along the high-symmetry X-G BZ path at T=300 K is presented in Fig. 5.12(a). The temperature-dependent band gap renormalization for MgO is presented in Fig. 5.12(b). Treatment of the EPI in the harmonic approximation and fully anharmonically leads to almost identical band gap renormalizations at finite temperatures. This suggests that even at high temperatures, MgO is a rather harmonic material. Approximately at T=500 K the difference between quantum and classical nuclear dynamics also becomes negligible. Although, the inclusion of anharmonicity to the description of PES has negligible effect, the lattice thermal expansion in MgO has a prominent influence on the band

gap renormalization. This observation was also highlighted in [283], where the LTE was evaluated using the QHA. We have calculated the LTE in the QHA to have a comparison with the fully anharmonic treatment of the LTE, and found that at high temperatures, the difference becomes non-negligible as demonstrated in Fig. 5.12(b). At T=1200 K the LTE constitutes a bit less than a half of the total band gap renormalization in MgO.

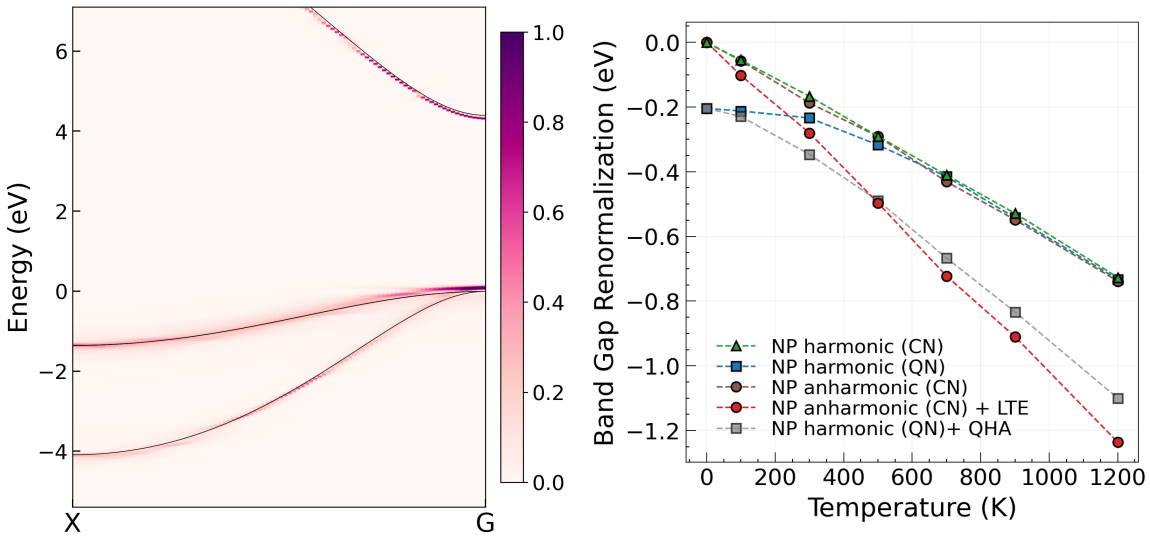

(a) (b)

Figure 5.12: (a) Thermodynamically averaged spectral function $\langle A(k,E)\rangle_T$ of MgO along X-G Brillouin zone path at T=300 K. Calculations are done at the DFT-PBEsol level of theory, with the cubic supercell containing 216 atoms. The band structure in static equilibrium is shown in black. (b) Temperature-dependent band gap renormalization in MgO. Both classical and quantum nuclei dynamics are taken into account.

The thermodynamically averaged spectral function of LiF calculated along the high-symmetry X-G BZ path at T=300K, calculated using stochastic sampling in quantum limit is presented in Fig. 5.13(a). The temperature-dependence of the band gap renormalization for LiF is shown in Fig. 5.13(b). Contrary to MgO, in LiF the quantum nature of the nuclei is important even at high temperatures. Moreover, a fully anharmonic treatment of the potential energy surface also leads to observable differences in the band gap renormalization. The LTE is influence on the band gap renormalization is comparable with the effects caused by the nuclear movement.

The temperature-dependence of the band gap renormalization for LiI is shown in Fig. 5.14. First of all, it is evident that the fully anharmonic treatment of the nuclear motion leads to substantially different results of the band gap renormalization. Specifically, at room temperature the anharmonic treatment leads to a 60 meV larger gap renormalization compared to the harmonic case. The difference grows with temperature and equals to 100 meV at T=600 K. The difference between the quantum and classical treatment of the nuclear motion is not that substantial and equals 22 meV at room temperature. The LTE influence on the gap renormalization is tangible already at room temperature and corresponds to almost half of the gap renormalization at high temperature.

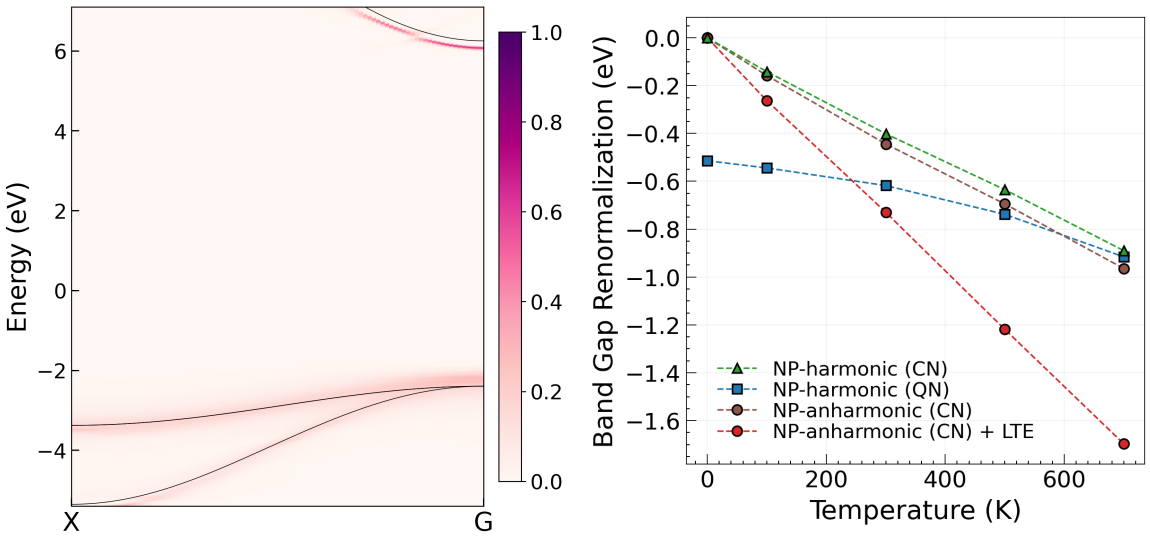

(a) (b)

Figure 5.13: (a) Thermodynamically averaged spectral function $\langle A(k,E)\rangle_T$ of LiF along X-G Brillouin zone path at T=300 K. Calculations are done at the DFT-PBEsol level of theory, with the cubic supercell containing 216 atoms. The band structure in static equilibrium is shown in black. (b) Temperature-dependent band gap renormalization in LiI. Both classical and quantum nuclei dynamics are taken into account.

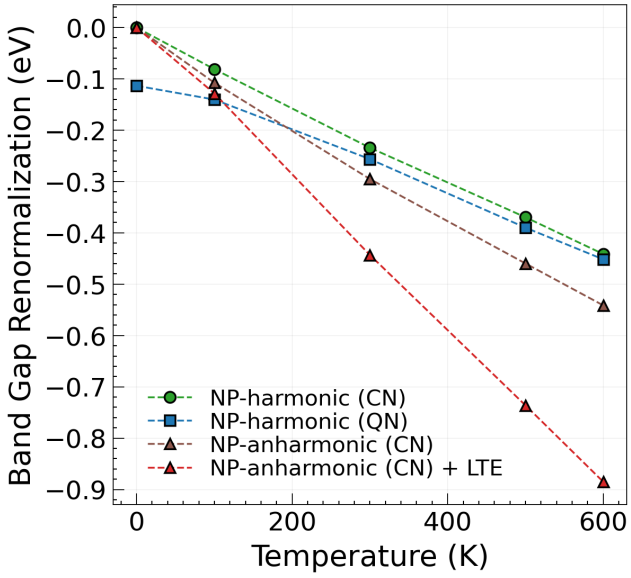

Figure 5.14: Temperature-dependent band gap renormalization in LiI. Both classical and quantum nuclei dynamics are taken into account.

The amplitude of nuclear vibrations grows with temperature as shown in Fig. 5.15(a). We evaluated the root-mean-squared atomic displacements along aiMD trajectories and evaluated bond length between atoms in the unit cell at different temperatures. This allowed us to evaluate the dependence between the band gap renormalization relative to the equilibrium gap and the amplitude of the atomic motion normalized to the bond length as shown in

Fig. 5.15(b). MgO and GaN have very similar amplitudes of atomic vibrations and also similar band gap renormalization values relative to the equilibrium gap.[7] The same trend is observed for LiI and LiF. However, the trends between compounds lead to the conclusion that the microscopic mechanism, which can describe band gap changes is more complicated and can not be directly explained solely based on the arguments related to the atomic vibrations. This suggests that, the bonding should be considered as in [17] for a more in-depth analysis.

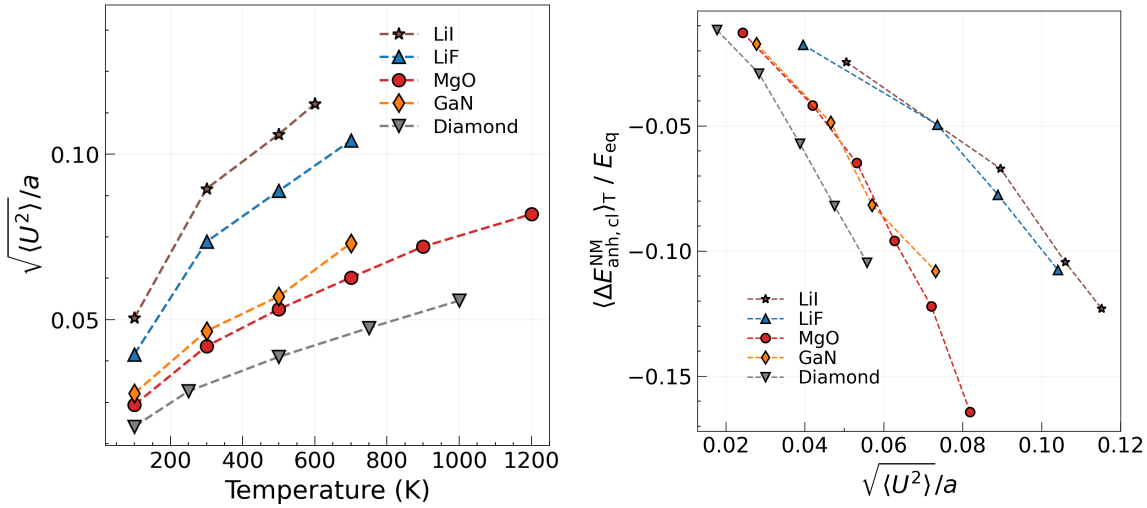

(a) (b)

Figure 5.15: (a) Temperature dependence of the root-mean-squared atomic displacements normalized by the bond distance between unit cell atoms. (b) Band gap renormalization caused by the nuclear motion normalized to the equilibrium band gap and root-mean-squared atomic displacements normalized by the bond distance between unit cell atoms. Same temperatures are used in plot (b) as in plot (a).

In order to gain a deeper understanding of the anharmonicity influence in LiF, LiI, and Mgo at different temperatures, we have computed the temperature dependence of the anharmonicity measure σ^A(T). Our results are shown in Fig. 5.16(a), which also includes the results for diamond and GaN obtained in Chapter 4. Our findings indicate that at room temperature, the anharmonicity metric of MgO (represented by σ^A_{300}(MgO) = 0.17) is comparable to that of GaN (σ^A_{300}(GaN) = 0.175). On the other hand, LiF and LiI exhibit anharmonic behavior already at room temperature, with σ^A_{300}(LiF)=0.3 and σ^A_{300}(LiI)=0.47, respectively. We note that LiI is the most anharmonic material in the chosen set. At T=1200 K, the anharmonicity measure of MgO is approximately 0.32, similar to σ^A_{300}(LiF) = 0.3. The anharmonicity measures of LiF and LiI grow linearly from room temperature to temperatures close to the melting points of these compounds. The slope of σ^A(LiF) and σ^A(LiI) below room temperature and T=100K is observed to be much steeper compared to temperatures above the room temperature. This behavior is likely associated with the quantum nuclear effect, which causes an underestimation of the anharmonicity metrics at low temperatures. This hypothesis is based on the data reported on anharmonicity measure in LiH, where it

[7] Equilibrium gaps are calculated at the DFT-PBEsol level of theory and thus, are underestimated comparably to the experimental values.

is shown that the inclusion of the QNE, by means of the path-integral aiMD, doubles the anharmonicity measure from ≈0.15 to ≈0.30 at T=100 [284].

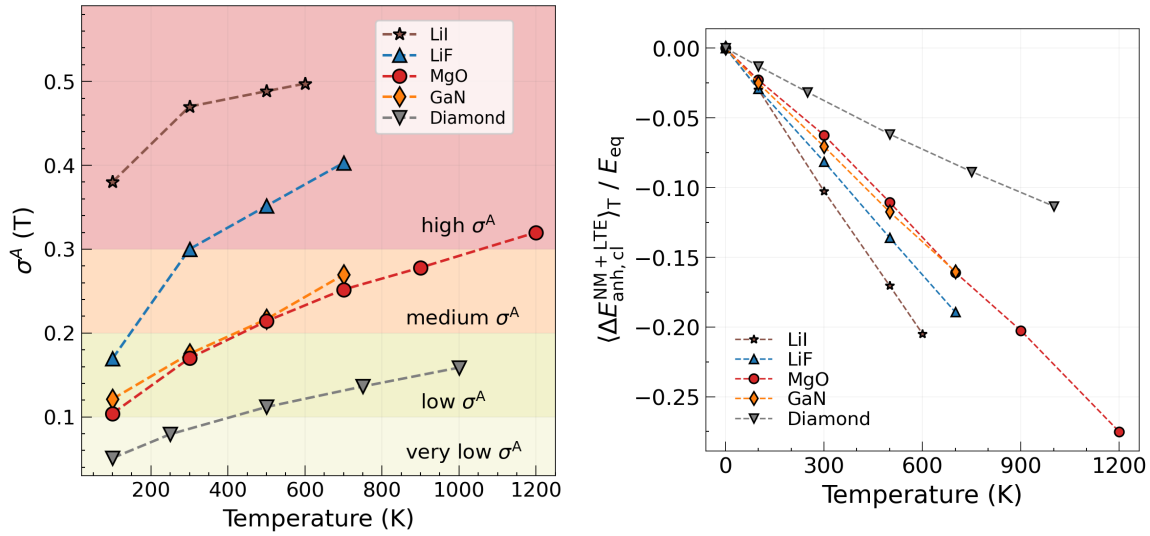

(a) (b)

Figure 5.16: (a) Temperature dependence of the anharmonicity measure σ^A(T) for diamond, zinc blende GaN, MgO, LiF, and LiI. (b) Total band gap renormalization caused by the nuclear motion and LTE normalized on the equilibrium band gaps with respect to the anharmonicity measure $\sigma^A(T)$ at different temperatures.

After analyzing these trends, we can assume that if there is a connection between anharmonicity metrics and band gap renormalization, the latter should be more pronounced in LiF than in MgO, once a wider temperature range is investigated. Fig. 5.16(b) shows the temperature-dependence of the band gap renormalization relative to the equilibrium band gap. As expected, compounds with higher anharmonicity metrics experience stronger renormalization. Consequently, we conclude that anharmonicity measure cannot only be an indicator of lattice anarmonicity [68], but also an indicator of non-negligible influence of lattice anharmonicity on the band gap.

5.7 Note on the accuracy of the DFT-PBEsol

We performed our calculations exclusively with the PBEsol xc-functional. Thus, equilibrium band gaps are noticeably underestimated. Nevertheless, it was frequently stated that for the calculations of the electron-phonon induced band gap corrections the LDA and GGA-type xc-functionals are appropriate, albeit the absolute value of the band gap is wrong [17]. The reason for that is that usual band gap underestimation of standard DFT approximations affects all frozen-phonon configurations in a very similar manner, and thus, it is expected to cancel in the calculation of the band gap correction, as it is a difference between the static equilibrium gap and the renormalized gap. These results are also supported by numerical calculations with methods of higher accuracy. For example, the pioneering work [52], related to the evaluation of the temperature-dependent band gap renormalization in diamond,

reported negligible difference between results obtained using GW [221, 222] and DFT-LDA calculations. Similar results for diamond were reported in [182], where it was shown that the utilization of G_0W_0 leads to an extra -10 meV renormalization of the indirect band gap of diamond at T=700 K. In addition, it was reported in the same work [182] that for a set of zinc blende compounds G_0W_0 corrections to the ZPR renormalization are very small comparably to the calculations done at the DFT-LDA level of theory. Calculations of the temperature dependence of the band gaps of diamond, Si, LiF, MgO, and TiO_2 have been performed in work [273] using both semi-local DFT (DFT-PBE) and the many-body G_0W_0 approximation. It was demonstrated that only in the case of TiO_2 the temperature-dependence of the band gap was sensitive to the level of the theory employed, while in the case of diamond, Si, LiF, and MgO inclusion of the correlation effects at the GW level of theory did not substantially affect the estimation of the band gap renormalization. Consequently, we assume that our findings, at least for MgO and LiF, will not change if many-body correlation will be considered.

On the other hand, the reliability of DFT for electron-phonon couplings has been questioned in recent years. Since the scattering of an electron by a phonon probes the excited states of a system, a theory describing this process should rely on an accurate unrenormalized band structures, unlike the ones of DFT. For example, the utilization of non-local DFT xc-functionals showed that in some cases (C_{60}, graphene, graphite, high-temperature superconductors) hybrid xc-functionals not only correct the band gap, but also more accurately describe the electron-phonon coupling [285–288]. In addition, it was demonstrated that the inclusion of many-body correlation effects by means of the GW calculations increases the strength of the EPI by 40% in GaAs [223]. However, the observed difference in the temperature dependence of the band gap only appears at high temperatures. As was shown in [182], the ZPR difference in GaAs between calculations with DFT-LDA and G_0W_0 is just 1 meV.

Since calculations of the band gap renormalization caused by LTE are done with unit cells, it is possible to check to which degree usage of different xc-functional affects the LTE contribution. We performed additional calculations of the band gap change, caused by the LTE with HSE06 xc-functional. For this test, equilibrium and expanded unit cell geometries, obtained with DFT-PBEsol, were used. Fig. 5.17(a) shows the difference between equilibrium gaps calculated with HSE06 and PBEsol. The MAE between the band gaps obtained with PBEsol and HSE06 is 1.57 eV. Tab. 5.4 contains information about MAE resolved for materials with different structural types. In most cases, equilibrium band gap, evaluated at the DFT-HSE06 level of theory is by 30% larger than in the case of DFT-PBEsol. Note that structural optimization with HSE06 will bring some additional change.

The influence of the LTE on the band gap renormalization calculated with PBEsol and HSE06 is shown in Fig. 5.17(b). For almost all compounds the difference between results obtained with HSE06 and PBEsol is within 25%, and the MAE is 9 meV among the whole set. Thus, we conclude that the differences in the band gaps change due to the LTE, between calculations done with HSE06 and PBEsol are not substantial for the compounds in our set, but note that this finding should be taken into account carefully, since we did not perform relaxation and the LTE evaluation using HSE06. Furthermore, these findings cannot be expanded to make conclusions about the difference between nuclear motion evaluation with

HSE06.

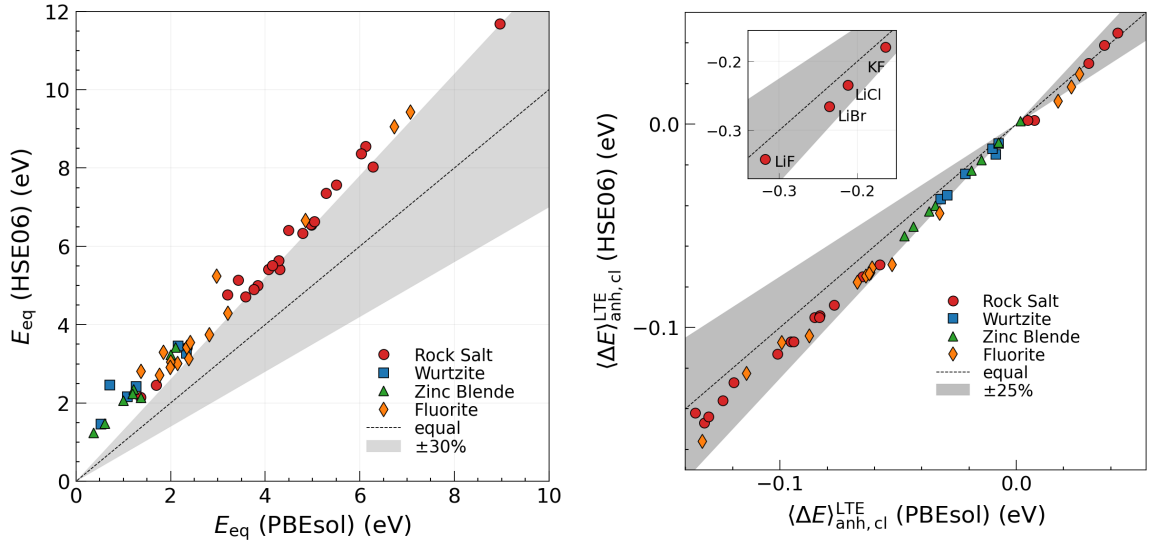

(a) (b)

Figure 5.17: (a) Comparison of the band gaps evaluated using HSE06 and PBEsol. (b) Comparison of the renormalization of the band gaps caused by the LTE and evaluated using HSE06 and PBEsol.

Table 5.4: MAE between the band gaps E_{eq} calculated using HSE06 and PBEsol and MAE between the band gaps renormalization caused by the LTE ΔE^{LTE} calculated using HSE06 and PBEsol.

Set	MAE(E_{eq}), eV	MAE($\langle \Delta E \rangle^{LTE}$), eV
Rock Salt	1.57	0.011
Wurtzite	1.19	0.004
Fluoride	1.36	0.012
Zinc Blende	1.03	0.004
Full Set	1.38	0.009

In summary, albeit for some materials many-body correlation effects can potentially alter the results obtained by the DFT calculations, we assume that our data is reliable, since the main points are made about the comparison of different effects, rather than the absolute values of renormalizations. Furthermore, calculations at a more accurate level are unfeasible with the current approach, since the utilized supercells contain hundreds of atoms.

Summary of the chapter

In this chapter, the band gap zero-point renormalization (ZPR) was thoroughly evaluated for a selected set of materials. The ionic mass and atomic motion amplitudes were applied as descriptors to observe and explain trends in the ZPR values. Subsequently, the quantifiable

contribution of the nuclear motion and lattice thermal expansion to the band gap renormalization at room temperature was assessed. The systematic investigation of the anharmonic lattice dynamics effects on the band gap renormalization was also conducted, using binary materials with rock salt, zinc blende, wurtzite, and fluorite-type structures. It is imperative to emphasize that the findings presented in this chapter should not be generalized to other types of semiconducting materials without proper consideration, as differing behaviors can potentially emerge in compounds with alternative structural types and chemical environments. An in-depth analysis of the band gap renormalization was performed for LiF, LiI, and MgO in a broad temperature range, resulting in the conclusion that the relative change of the band gap is correlated with the anharmonicity measure, with materials that have higher anharmonicities exhibiting a larger band gap renormalization. Similar studies of other material classes may deepen our comprehension of the relative significance of the various effects on the strength of electron-phonon interactions.

Summary and outlook

We have conducted a comprehensive analysis of the temperature-dependent band gap renormalization using a computationally guided approach. The methodology employed in this study is applicable to both harmonic and anharmonic materials and is based on a combination of ab initio molecular dynamics (aiMD) simulations and the band-unfolding technique. This approach allows for a fully anharmonic treatment of the nuclear motion. If needed the calculations can be also done in the harmonic approximation for the potential energy surface. To validate the methodology, we performed benchmark simulations on diamond and zinc blende GaN, and compared the results to previously published theoretical and experimental data.

As an application, we analyzed 52 binary materials to examine the temperature influence on the band gap renormalization. The trends of the ZPR were explained using descriptors based on the amplitude of the nuclear motion and the atomic masses of the materials. We also contrasted the treatment of the nuclear motion in the classical and quantum limits and showed that the highest phonon frequency can be used as a descriptor to classify materials in which quantum statistics for nuclear motion has particular importance. Then we evaluated the impact of the LTE and the anharmonicity of PES on the band gap renormalization. Our findings indicate that the highest phonon energy can be a useful indicator of the quantum nature of the nuclear motion. Moreover, the separation of LTE and nuclear motion contributions to the band gap renormalization allowed us to quantify the importance of the anharmonic treatment of atomic vibrations. Our results suggest that LTE can contribute up to half of the total band gap renormalization.

In order to assess the impact of the anharmonicity of the PES on the band gap renormalization, we utilized a recently introduced anharmonicity measure [68]. Consequently, it was demonstrated that, to a certain extent, the anharmonicity measure can be utilized to identify materials in which the fully anharmonic treatment of the nuclear motion has to be taken into account to obtain accurate estimates of the band gap renormalization. Our study entailed the calculation of the temperature-dependent band gap renormalization for MgO, LiF, and LiI across a broad temperature range, with the goal of gaining a deeper understanding of the influence of anharmonicity. Our results showed that the temperature-dependent anharmonicity measure indicates that materials with higher anharmonicity measure exhibit a greater degree of band gap renormalization. Specifically, it was established that the band gap of materials with highly harmonic potential energy surfaces, such as diamond, undergo much lower changes compared to highly anharmonic materials like LiI. On the other hand, materials with moderate anharmonicity, such as GaN or MgO, undergo moderate changes

in the band gap renormalization with temperature. It is important to note that this computational study was only conducted with diamond, zinc blende GaN, MgO, LiF, and LiI, and thus the results obtained can be extended to other materials with a certain portion of consideration, because different behavior may emerge in compounds with different structural types and chemical environments.

In this study, we concentrated on binary materials with a set of different structural types and physical properties. However, to extend our understanding of the method applicability and nature of the EPI, the method should be further applied to other classes of materials. It is potentially interesting, from our perspective, to study materials with the inverse Varshni effect [273, 277, 289–294]. Some of these materials, specifically copper halides, are also extremely anharmonic and display ionic diffusion under heating [68]. Treatment of ionic diffusion in the supercell during simulations requires further development of band unfolding methodology though. The same is relevant for materials with pronounced spin-orbit coupling [18, 295], which would be interesting to investigate at finite temperatures, but also requires to implement further functionality. Additionally, it is important to investigate the nuclear quantum effect, which has been noted to produce substantial alterations in the EPI strength in diamond [228, 296], anharmonicity in LiH [284], and electron-phonon interaction strength in molecular crystals [30, 216]. It is noteworthy that the established methodology can, in principle, accommodate materials with defects, though further testing is required to perfect the procedure. Furthermore, the established approach can be applied to analyze the physical properties governed by the EPI, such as electronic transport [28], optical properties [39], and temperature impact on topological insulators [19, 297].

A substantial portion of aiMD trajectories, stored in the NOMAD repository [274] [8], were reused in the present study. The computational demands associated with the aiMD simulations constitute one of the key challenges in the workflow, thus reuse of the dataset stored in the NOMAD repository appeared to be extremely useful. In principle, to minimize the computational cost, modern machine learning techniques for molecular dynamics simulations can be employed, as outlined in [298–300]. The aiMD trajectory, calculated at the DFT level of theory with smaller supercells, can serve as a basis for fitting, while simulations with the production-size supercells, can be performed with machine learned potentials. The electronic structure calculations required for systems with thousands of atoms can also be accelerated through the fitting of the Kohn-Sham DFT results for smaller supercells using either the atomic cluster expansion method [301, 302] or message-passing neural networks [303, 304] as demonstrated in [305].

Our methodology can be integrated into various electronic structure packages during the post-processing stage. aiMD simulations are commonly available in a multitude of packages [3–6]. The stochastic sampling process can be performed using either the TDEP approach [69, 70] or the SSCHA method [72], which are interfaced to different DFT codes. In addition, the band structure unfolding formalism has been developed for codes that use plane wave basis sets [81, 84, 239]. While it is reasonable to assume that results obtained from different codes will be of comparable accuracy [306], further tests similar to those performed in [265] are required. We note that initial tests conducted with Si using the Quantum Espresso

[8] NOMAD dataset DOI:dx.doi.org/10.17172/NOMAD/2020.06.25-1 associated with the work [68]

package yielded results in perfect agreement with those from FHI-aims. Our user-friendly interface is written in Python and makes use of the ASE [307] library. The scheduling of calculations is managed using Fireworks [308]. The interface can be expanded to accommodate simulations with other DFT codes.

The electronic transport properties of materials can be analyzed through the evaluation of the EPI [27, 28, 60, 309–313]. In theory, the electrical conductivity tensor can be obtained from first principles using the Kubo-Greenwood formalism [314, 315], as demonstrated in the recent work [316]. However, such computations necessitate the utilization of an extremely dense sampling of the Brillouin zone to obtain converged values of the electrical transport coefficients [317]. A more pragmatic approach, is based on the perturbative treatment of the EPI, as demonstrated in [25]. In the case of highly-anharmonic materials, the lattice dynamics must be handled with caution, as illustrated in the examination of $SrTiO_3$ [77] through the treatment of the anharmonicity of the potential energy surface to the third order in Taylor expansion. Although the temperature-dependence of the mobility obtained in [77] is consistent with experimental results, the absolute values differ from the experimental ones by a factor of ten [77]. It remains an open question whether this discrepancy is a result of polaronic effects, as suggested in a accompanying study [78], or if higher-order terms of anharmonicity need to be taken into account.

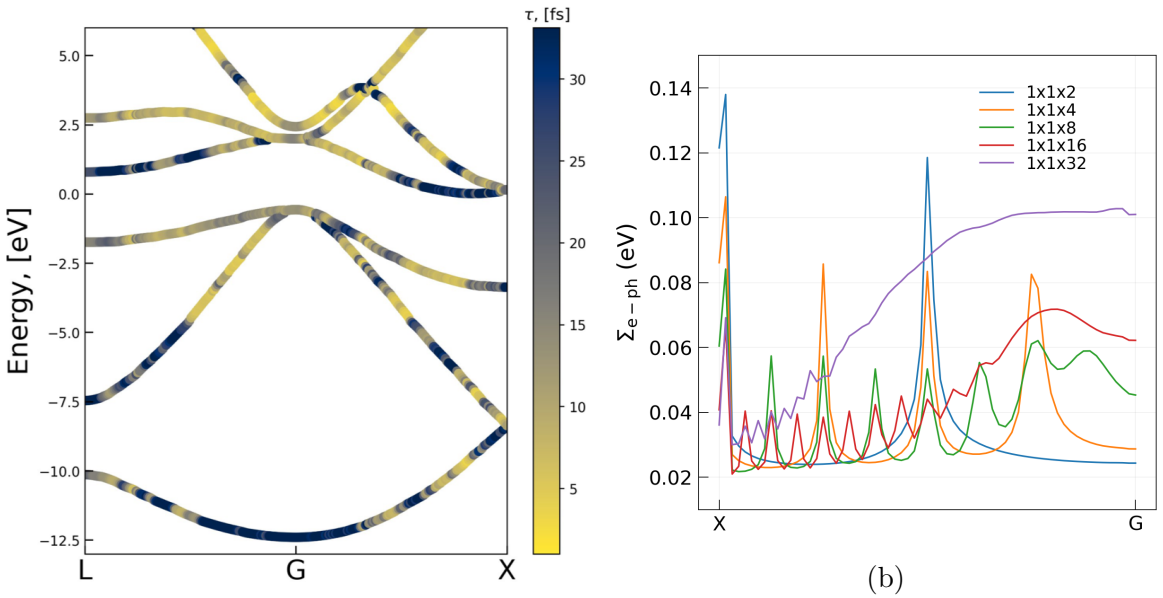

Figure 5.18: (a) The band structure of Si, together with a color map of the quasiparticles relaxation time. (b) Convergence of the $\mathrm{Im}\Sigma_{\text{e-ph}}$ of the lowest lying energy level from plot(a) with respect to the 1×1×N supercell.

Besides elucidating the underlying microscopic mechanisms of the band gap renormalization at finite temperatures, developments presented here, can potentially enable a fully non-perturbative assessment of the charge transport coefficients. According to the reference [8], the spread of the spectral function corresponds to the imaginary part of the electron-

phonon self-energy $\mathrm{Im}\Sigma_{\text{e-ph}}$, which is inversely proportional to the quasiparticle lifetimes $\tau_{\text{e-ph}} = [\mathrm{Im}\Sigma_{\text{e-ph}}]^{-1}\,\hbar/2$. Consequently, $\mathrm{Im}\Sigma_{\text{e-ph}}$ can be extracted by fitting the thermodynamically averaged spectral function with the assumption of a Lorentzian lineshape for the spectral function peaks. Quasiparticle lifetimes calculated in this manner can then be incorporated into the Boltzmann transport equation to determine transport coefficients such as the mobility and Seebeck coefficient at finite temperatures [7, 28, 309]. To validate this workflow, we tried to obtain lifetimes in Si. We have chosen Si, because the literature data for $\mathrm{Im}\Sigma_{\text{e-ph}}$ of Si at room temperature is published in [38]. The band structure of Si, along with the color-coded imaginary part of the electron-phonon self energy, is shown in Fig. 5.18(a). For these calculations, a $4 \times 4 \times 4$ supercell of Si was used, while the electron-phonon matrix elements in [38] were calculated on interpolated 40×40×40 q and k-point grids. However, while the lifetimes in [38] exhibit a smooth variation along the band, this is not the case in our calculations. The main challenge faced by the study is therefore to reach the thermodynamic limit, i.e., to converge e-ph self energy with respect to the supercell size.

We evaluated the convergence of $\mathrm{Im}\Sigma_{\text{e-ph}}$ by incrementally increasing the length of the Si conventional cell in one direction. For this test we used supercells with size ranging from 1×1×2 to 1×1×32 of the primitive cell size. The results of this investigation are displayed in Fig. 5.18(b). One can observe that the magnitude of $\mathrm{Im}\Sigma_{\text{e-ph}}$ decreases in the mid of the path between X and G points, as the size of the supercell approaches 1×1×16, but at 1×1×32 it experiences an rapid increase. Furthermore, no convergence is observed at the G-point.

A deeper understanding of the physics behind the observed trends in $\mathrm{Im}\Sigma_{\text{e-ph}}$ behavior, can be attained by disentangling the influence of different phonon modes. To perform such operation one has to decompose phonon dispersion into properly connected phonon branches. This can be achieved by assigning an index to each phonon band at each phonon wave vector. A somehow naive labeling can be done by comparing the scalar product of each phonon eigenvector at one q-point with the phonon eigenvectors at neighboring q-points in the BZ. However, this approach necessitates a dense sampling of the BZ and may fail in the case of phonon branch crossings [318]. An unambiguous labeling can be accomplished by calculating the Berry connection for phonons, as demonstrated in previous studies [225,319]. At present, there is no readily available solution for this task to the best of our knowledge and thus, it is likely the subject of the future work.

Appendix A: Polarization and Born effective charges benchmark

We validate the accuracy of our calculations by firstly comparing our results to literature values of the spontaneous polarization (P_s) of BaTiO3 and PbTiO3 [320, 321]. Fig. 5.19 shows the polarization of BaTiO3 with respect to the linear displacements from the centrosymmetric $P4/mmm$ phase to the non-centrosymmetric $P4mm$ phase. The distance between polarization branches corresponds to the polarization quanta [322] ($P_q = eR/\Omega$), with P_c and being the polarization of the centrosymmetric and non-centrosymmetric structures, respectively. The spontaneous polarization is calculated as $P_s = P_{nc}$ - P_c. The results of this validation test are presented in Tab. 5.5.

In the second step of our benchmark, we calculated the P_s value using various xc-functionals (LDA, PBE, PBEsol, HSE06, PBE0). We optimized the structures such that the force on the atoms was below 0.1 meV/atom. For the numerical settings, we used the *tight* default for LDA, PBE, and PBEsol, and the *intermediate* default for the HSE06 and PBE0 xc-functionals. [9] The spin-unpolarized calculations for $BaTiO_3$ and PbTiO3 were performed using a Gamma-centered $8 \times 8 \times 8$ k-points grid. For the evaluation of Ps, we used 20 grid points in the direction parallel to the polarization vector ($\vec{k}\|$) and 20×20 grid points for the perpendicular directions ($\vec{k}\perp$) in all calculations. The results of the structural parameters and P_s values are shown in Table 5.6. Ps was calculated both with (numbers in brackets) and without spin-orbit coupling (SOC), which was taken into account in a perturbative manner [263]. Our results for both $P4mm$-Ba/$PbTiO_3$ compounds show good agreement with previous calculations [320, 321, 324–326]. The effect of SOC was found to be minimal.

We also conducted cross-check calculations by optimizing the structure with one xc-functional and then computing P_s of the optimized structure using all xc-functionals in a set. The results of this test are shown in Fig.5.20. Hybrid functionals tend to display slightly lower values of P_s, within a couple percent, compared to LDA or GGA-type functionals. For instance, P_s calculated with HSE06, using the geometry optimized with LDA, is 25.5 $\mu C/cm^2$, whereas calculations of P_s with LDA give 26.4 $\mu C/cm^2$. Therefore, the dependency of the spontaneous polarization on the xc-functional is not primarily rooted in the calculation of the polarization itself, but rather in the dependence of the equilibrium geometry on the xc-functional, which is also in agreement with previous studies [321, 326].

The comparison with experimentally reported values of the P_s is complicated, since exper-

[9] The xc-functional discussion is presented in Sec. 1.3. We note that for the PBE0 xc-functional exchange energy and Hartree-Fock energy are mixed in a set 3:1, along with the full PBE correlation energy [323].

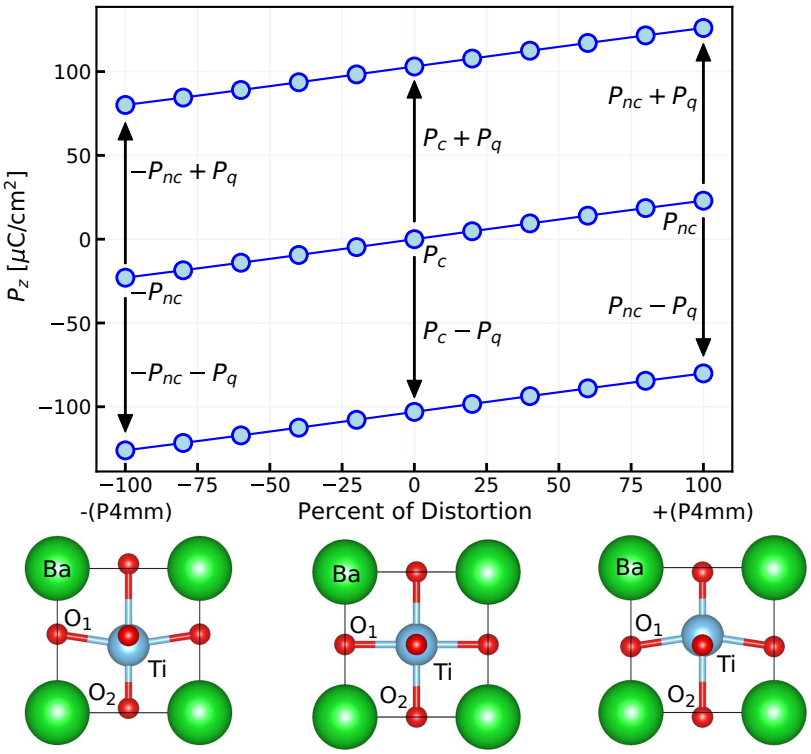

Figure 5.19: P_s=P_{nc}-P_c calculated as a function of distortion from the centrosymmetric $P4/mmm$-$BaTiO_3$ to non-centrosymmetric structure $P4mm$-$BaTiO_3$. We used relaxed structure and LDA xc-functional, 20×20×20 for P_s and 8×8×8 kpoints grid for sampling the BZ. Green spheres correspond to Ba, blue to Ti, and red to O.

iments devoted to the polarization measurements [328–332] do not mention information about the structural parameters, while the works, which reported structural information [333–335] are not devoted to the polarization measurements. Consequently, we performed the calculations at experimentally reported parameters, but make comparison with works, which reported polarization measurements. The results of this test are presented in Tab. 5.7. Both experimental works [328,329] found that the value of P_s for $P4mm$-$BaTiO_3$ is 26 $\mu C/cm^2$, which was determined using the Sawyer-Tower arrangement in the former work and optical mode-strength analysis in the latter. Our calculated values are in good agreement with these results. For $P4mm$-$PbTiO_3$, experimental measurements at room temperature have been scattered, with estimates ranging from 57 $\mu C/cm^2$ [331] (below 300°C) to 75$\mu C/cm^2$ [330, 332]. Our computations have resulted in higher values of P_s – around a hundred $\mu C/cm^2$. This significant difference between experimental and calculated values for $P4mm$-$PbTiO_3$ has also been observed in other computational works [320, 321, 324–326].

There are several potential explanations for this discrepancy. Firstly, it should be noted that the experimental works were often conducted using modified $PbTiO_3$ ceramics [331,332]. Secondly, the work by [332] highlighted the formation of microcracks and potential charge leakage during measurements at high-frequency fields (above 10 Hz), which could impact the

Table 5.5: Difference between the P_s values calculated in this work and previously reported computational studies.

Code	xc	a (Å)	c/a	P_s (μC/cm^2) Reference	This work
			$BaTiO_3$		
VASP	LDA	3.943	1.013	22.9 [320]	22.91
Abinit	LDA	3.954	1.006	20 [321]	19.9
Abinit	PBE	4.013	1.035	39 [321]	39.8
			$PbTiO_3$		
VASP	LDA	3.858	1.071	94.3 [320]	95.1
Abinit	LDA	3.872	1.041	78 [321]	79.7
Abinit	PBE	3.834	1.221	129 [321]	128.8

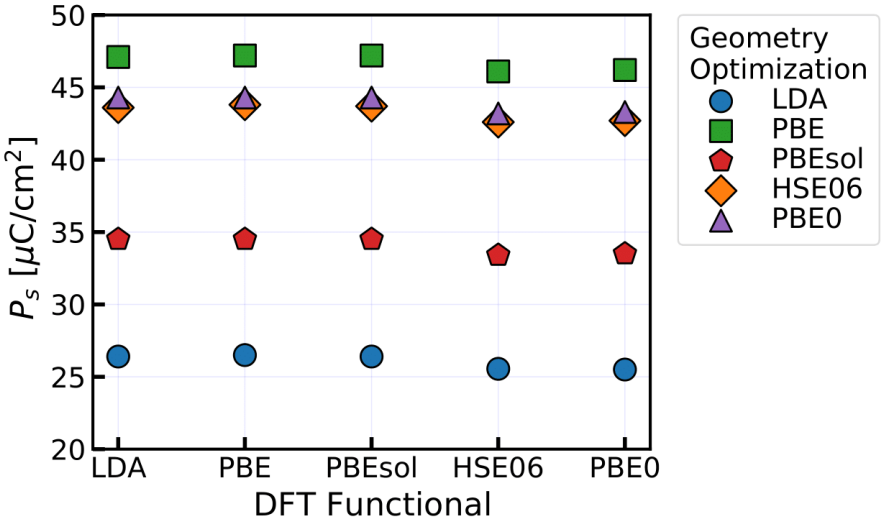

Figure 5.20: The correlation of P_s values calculated with different DFT xc-functionals and different geometries for $BaTiO_3$. The shape of the point on the graph represents the DFT functional used for structure optimization. Abscissa shows the functional used for P_s evaluation.

measurements of natural ferroelectric properties. Thirdly, such uncertainty may be related to the different thermodynamic conditions during measurements, as $PbTiO_3$ is sensitive to temperature conditions [336]. It is worth noting that in the work by [327], P_s of $PbTiO_3$ was computed to be 104 $\mu C/cm^2$ at 295°C and 74 $\mu C/cm^2$ at 700°C.

Finally, we verified the values of the Z^* tensor for the cubic phases of Ba/$PbTiO_3$, which have the space group $Pm\bar{3}m$. The crystalline symmetry resulted in the Z^* tensor for both compounds being isotropic. We used the finite-difference method with atom displacements of 0.5-2% of the lattice vector length and obtained identical values. The Z^* values are in agreement with previous literature reports [327, 329, 337] (see Tab. 5.8).

Table 5.6: Results for the P_s of $P4mm$-Ba/$PbTiO_3$. First two columns are lattice vector length a and tetragonality c/a. Next three columns contain Ti and O positions and the last one is the P_s value, without and with spin-orbit coupling, respectively. Ba/Pb atom is situated at the origin. Reference computational results are taken from: [a] [326], [b] [320], [c] [327], [d] [324].

Approach	a (Å)	c/a	Ti	O_1	O_2	P_s ($\mu C/cm^2$)
			$BaTiO_3$			
LDA	3.926	1.01	0.487	0.514	0.021	26.4 (26.5)
PBE	3.984	1.05	0.481	0.529	0.049	47.2 (47.3)
PBEsol	3.953	1.02	0.483	0.518	0.029	34.51 (34.56)
PBE0	3.953	1.04	0.479	0.523	0.043	43.33 (43.37)
HSE06	3.958	1.04	0.480	0.523	0.042	42.65 (42.69)
LDA [a]	3.946	1.011	0.488			24.3
HSE06 [a]	3.959	1.039	0.481			40.7
LDA [b]	3.943	1.013	0.492	0.513	0.021	22.9
LDA [c]						30
			$PbTiO_3$			
LDA	3.857	1.04	0.533	0.604	0.092	81.7 (80.6)
PBE	3.839	1.23	0.556	0.667	0.190	126.3 (125.1)
PBEsol	3.867	1.08	0.538	0.622	0.118	96.1 (94.9)
PBE0	3.824	1.19	0.549	0.656	0.161	114.24 (104.09)
HSE06	3.825	1.19	0.578	0.655	0.170	120.3 (119.2)
LDA [a]	3.865	1.045	0.566			79.8
HSE06 [a]	3.832	1.158	0.547			114.4
GGA [d]						88
LDA [b]	3.858	1.071	0.542	0.622	0.115	94.3
LDA [c]						104 (T=295 K)
LDA [c]						74 (T=700 K)

Table 5.7: P_s value of $P4mm$-Ba/$PbTiO_3$ calculated using different DFT functionals at experimental structural parameters. PBE and PBEsol lead to nearly the same value as LDA.

P_s, $\mu C/cm^2$				
Material	Structure	LDA	HSE06	Experiment[c]
$BaTiO_3$	[334]	22.5	21.6	26[d]
$PbTiO_3$	[335]	99.8	98.4	57[e], 75[f]

Table 5.8: Born Effective Charges tensor in units of the electron charge for $Pm\bar{3}m$-$BaTiO_3$ and $Pm\bar{3}m$-$PbTiO_3$.

Approach	a, (Å)	Z^*_{zz} (Ba/Pb)	Z^*_{zz} (Ti)	Z^*_{zz} (O_1)	Z^*_{zz} (O_2)
		$Pm\bar{3}m$-$BaTiO_3$			
LDA	3.934	+2.79	+7.35	-5.80	-2.17
LDA	3.94	+2.78	+7.36	-5.80	-2.17
LDA	4.0	+2.75	+7.40	-5.85	-2.15
PBE	4.017	+2.76	+7.41	-5.89	-2.14
PBEsol	3.967	+2.78	+7.36	-5.83	-2.16
HSE06	3.981	+2.69	+7.02	-5.54	-2.09
PBE0	3.976	+2.70	+7.03	-5.56	-2.09
Exp [329]	4.008	+2.9	+6.7	-4.8	-2.4
LDA [327]	3.945	+2.75	+7.16	-5.69	-2.11
LDA [337]	3.94	+2.77	+7.25	-5.71	-2.15
		$Pm\bar{3}m$-$PbTiO_3$			
LDA	3.884	+3.91	+7.22	-5.93	-2.60
PBE	3.964	+3.85	+7.28	-6.01	-2.56
PBEsol	3.917	+3.90	+7.22	-5.95	-2.58
HSE06	3.927	+3.77	+6.93	-5.62	-2.54
PBE0	3.921	+3.77	+6.93	-5.62	-2.54
LDA [327]	3.89	+3.90	+7.06	-5.83	-2.56

Appendix B: computational details for chapter 4

All calculations were performed using the full-potential all-electron numeric atomic orbital code FHI-aims [5]. The LDA xc-functional was used exclusively. FHI-aims *light* defaults were used for the numerical settings and for the basis set for both materials. *Tight* defaults were only used to check the value of zero point renormalization. The $12 \times 12 \times 12$ kpoints BZ integration grid was used for the calculations with the primitive cell. K-points sampling was adapted for the calculations with the supercells.

The LDA optimized lattice constant of diamond is 3.537 Å, which is slightly smaller than the experimental value of 3.567 Å [338] and comparable to the lattice constant 3.529 Å, used in the previous computational work [17]. GaN exhibits two polymorphs: zinc blende and wurtzite. We used the zinc blende structure to allow for a comparison with the literature [90, 93, 94]. The LDA optimized lattice constant of GaN is 4.475 Å, while the experimental values range from 4.507 Å [339] to 4.52 Å [90]. The LDA band gaps of GaN and diamond are, as expected [90, 339], substantially lower than their experimental values. The LDA band gaps of GaN and diamond are 2.00 eV and 4.23 eV, while the experimental values are 3.28 eV [90, 339] and 5.47 eV [208], respectively. The parameters of materials used in our calculations are summarized in Tab. 5.9. We also note that we can perform calculations of the band gap renormalization up to the high temperatures, because GaN is stable up to approximately T=1700 K [340], while melting point of diamond is pressure-dependent and reaches approximately T=4000 K at 11 GPa [341].

Lattice dynamics calculations were managed using the FHI-vibes [342] interface. Phonons were calculated using the finite differences approach [162] as implemented in the Phonopy package [164]. Born-Oppenheimer Ab Initio Molecular Dynamics (aiMD) simulations were performed for diamond and GaN to take into account all orders of the anharmonicity of the

Table 5.9: Lattice parameters and band gap of diamond and GaN used in this work and comparison to literature data. Note that works [17] and [93] only mentioned the lattice parameters of diamond and GaN without the values of the band gap.

Material	This Work		Reference Theory	Experiment	
	a (Å)	E (eV)	a (Å)	a (Å)	E (eV)
diamond	3.537	4.23	3.529 [17]	3.567 [338]	5.47 [208]
GaN	4.475	2.04	4.499 [93]	4.507 [339] , 4.52 [90]	3.28 [90, 339]

nuclear movement. aiMD simulations were carried out in the canonical ensemble (NVT) with the Langevin thermostat [187, 343, 344] using a time step of 1 fs. We generated trajectories with a time length of 5 ps, of which the first picosecond were used to thermally equilibrate the system and the last 4 ps were used for the band gap renormalization calculations. Initial atomic positions and velocities were pre-thermalized using stochastic sampling of the canonical ensemble approach [180, 181]. This allows to start ensemble run of aiMD with negligible equilibration time [69].

Evaluation of the LTE in the QHA is done by performing calculations of the optimal lattice constant at different temperatures, by minimizing the free energy based on the Birch-Murnaghan equation of state [202, 203]. Slightly increased and slightly decreased volumes ($\pm 2.5\%$ from the equilibrium volume) of the supercell with 216 atoms were used in this case. Once LTE is known, we performed band structure calculations for the structures with varying lattice constant according to the measured thermal lattice expansion coefficient and obtained the band gap renormalization. The LTE in the case of NVT-aiMD simulations is taken into account by computing thermodynamic average of the stress tensor observed along aiMD trajectory [68, 85]. Once the internal pressure is estimated from the stress tensor, the structure is reoptimized under this internal pressure to obtain thermally expanded geometry. See Sec. (2.4) for details of the LTE evaluation.

Appendix C: computational details for chapter 5

We performed all calculations with the all-electron, full-potential, numeric-atomic orbital code FHI-aims [5] with PBEsol xc-functional in the DFT framework. Lattice dynamics calculations were managed by using FHI-vibes [342]. Phonons were calculated using finite differences approach [162] as implemented in the Phonopy package [164]. For all compounds FHI-aims *light* defaults were used for the numerical settings and for the basis set, if it is not stated otherwise. We used $12 \times 12 \times 12$ Brillouin zone (BZ) integration k-points grid for the self-consistency calculations of the primitive cells (k-points grid was adjusted for the calculations with supercell). The band gaps computed at the DFT-PBEsol level of theory are lower that the experimental values, due to the well known inability of PBEsol exchange-correlation functional to accurately describe the band gap [124, 125].

A substantial portion of aiMD trajectories, stored in the NOMAD repository [274] [10], were reused in the present study. In the work [68], Born-Oppenheimer aiMD simulations were carried out in the canonical ensemble (NVT) with the Langevin thermostat. These aiMD trajectories have lengths 5 fs each. For some compounds of the particular interest (MgO, LiF, LiI), we performed additional aiMD simulations. We utilize the FHI-vibes interface between ASE and FHI-aims to manage aiMD calculations. We pretermalize samples (generate displacements and assign velocities to each atom) using harmonic sampling of the canonical ensemble methodology [180]. This allows to start ensemble run of aiMD with negligible equilibration time [181, 184]. We generated trajectories with a time length of 5 ps, with a time step of 1 fs. Thermal lattice expansion was calculated by computing the thermodynamic average of the stress tensor observed during an aiMD trajectory. The structure was then reoptimized under external pressure to obtain temperature-dependent geometries for which the stress tensor becomes negligible in the thermodynamic average.

Fig. 5.21 shows the value of the band gap change caused by the LTE relatively to the equilibrium gap. Fig. 5.22 shows the results of the band gap renormalization calculations treating nuclear motion in the classical limit. Tab. 5.10, Tab. 5.11, Tab. 5.12, and Tab. 5.13 contain information about the lattice parameters of materials in the study at zero temperature and once they are heated to 300 K. Band gaps calculated for initial structures and for expanded structures are reported as well.

[10] NOMAD dataset DOI:dx.doi.org/10.17172/NOMAD/2020.06.25-1 associated with the work [68].

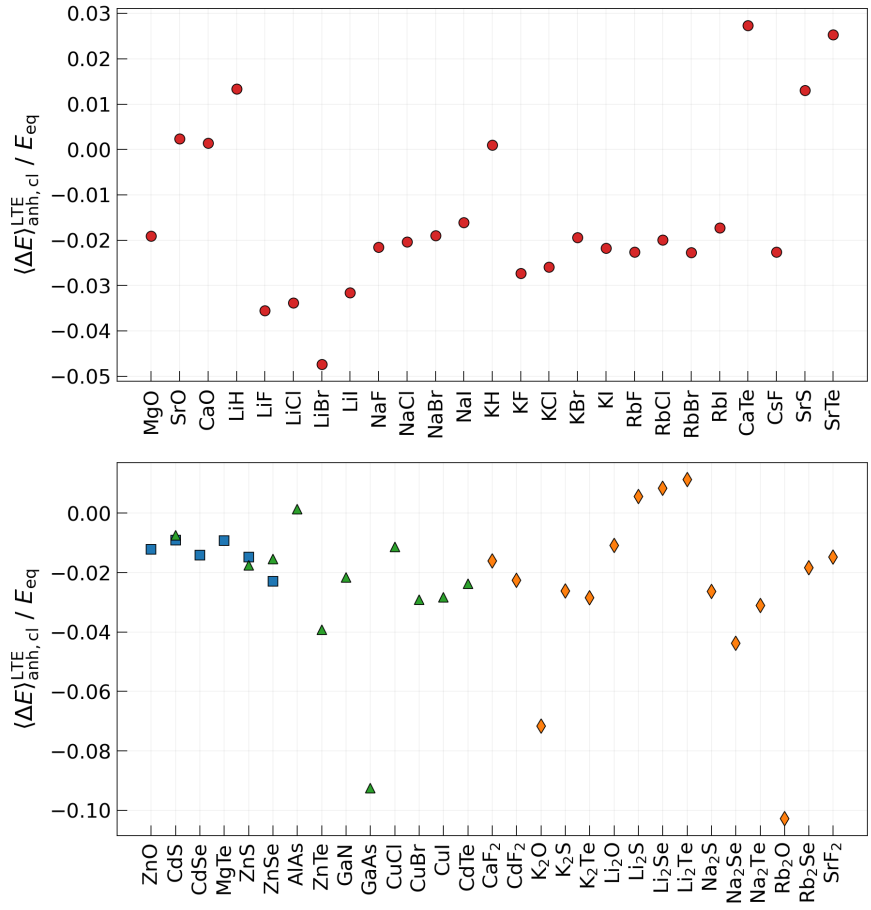

Figure 5.21: Band gap renormalization caused by the lattice thermal expansion at T=300 K for compounds with wurtzite, zinc blende, and fluoride structure. The calculations are done fully anharmonically.

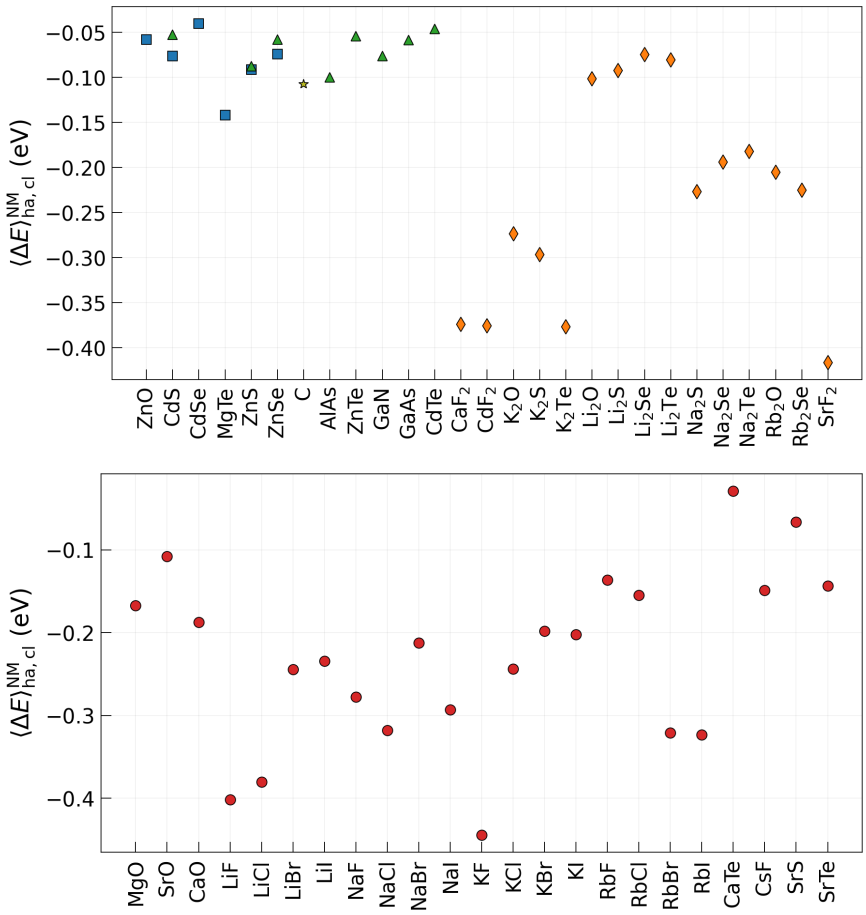

Figure 5.22: Band gap renormalization at room temperature due to the nuclear motion. The calculations are done in the harmonic approximation using classical statistics for the nuclear motion.

Table 5.10: Rock Salt Structures

System	σ^{A}_{300}	$E^{PBEsol}_{g,0}$	$E^{PBEsol}_{g,300}$	a_0	a_{300}	$E^{HSE06}_{g,0}$	$E^{HSE06}_{g,300}$	ΔE^{PBEsol}_{g}	ΔE^{HSE06}_{g}
KCl	0.419	5.036	4.906	6.254	6.337	6.489	6.345	-0.13	-0.144
LiI	0.488	4.311	4.175	5.898	5.987	5.266	5.254	-0.136	-0.012
SrO	0.223	3.203	3.211	5.139	5.161	4.762	4.765	0.008	0.002
NaCl	0.37	4.971	4.87	5.613	5.664	6.446	6.334	-0.101	-0.113
KF	0.374	6.032	5.868	5.313	5.371	8.194	8.015	-0.164	-0.179
KI	0.448	3.84	3.757	6.995	7.087	4.904	4.809	-0.083	-0.095
AgCl	1.058	0.734	0.733	5.47	5.512	2.311	2.308	-0.001	-0.003
SrS	0.209	2.346	2.377	5.983	6.01	3.443	3.473	0.031	0.03
NaI	0.429	3.584	3.526	6.404	6.461	4.641	4.572	-0.058	-0.069
CsF	0.48	5.285	5.165	5.986	6.058	7.231	7.104	-0.12	-0.127
RbCl	0.434	4.795	4.699	6.566	6.636	6.231	6.124	-0.095	-0.107
MgO	0.172	4.488	4.402	4.226	4.239	6.313	6.218	-0.085	-0.095
SrTe	0.24	1.692	1.735	6.623	6.656	2.502	2.547	0.043	0.045
KBr	0.426	4.282	4.199	6.559	6.631	5.543	5.449	-0.083	-0.094
RbBr	0.44	4.152	4.058	6.859	6.955	5.404	5.297	-0.094	-0.107
NaF	0.318	6.121	5.989	4.634	4.674	8.402	8.255	-0.132	-0.147
RbF	0.407	5.501	5.377	5.632	5.699	7.565	7.429	-0.124	-0.136
CaO	0.196	3.424	3.429	4.774	4.79	5.135	5.137	0.005	0.002
LiBr	0.468	4.982	4.746	5.411	5.5	6.286	6.021	-0.236	-0.265
LiCl	0.4	6.279	6.067	5.079	5.144	7.791	7.558	-0.212	-0.234
CaTe	0.238	1.362	1.399	6.317	6.344	2.186	2.225	0.037	0.039
NaBr	0.4	4.065	3.988	5.932	5.99	5.326	5.237	-0.077	-0.089
RbI	0.471	3.76	3.695	7.303	7.392	4.823	4.748	-0.065	-0.075
LiF	0.327	8.965	8.646	4.013	4.062	11.346	11.003	-0.318	-0.342

Table 5.11: Zinc Blende Structures

System	σ^{A}_{300}	$E^{PBEsol}_{g,0}$	$E^{PBEsol}_{g,300}$	a_0	a_{300}	$E^{HSE06}_{g,0}$	$E^{HSE06}_{g,300}$	ΔE^{PBEsol}_{g}	ΔE^{HSE06}_{g}
AlAs	0.181	1.377	1.379	5.698	5.7	2.135	2.136	0.002	0.002
CuI	0.479	1.111	1.08	5.991	6.014	2.632	2.606	-0.031	-0.026
CdTe	0.319	0.614	0.599	6.524	6.534	1.454	1.436	-0.015	-0.018
ZnTe	0.264	1.203	1.156	6.091	6.111	2.184	2.129	-0.047	-0.055
ZnS	0.243	2.107	2.07	5.365	5.38	3.373	3.33	-0.037	-0.043
ZnSe	0.256	1.222	1.203	5.653	5.662	2.325	2.302	-0.019	-0.023
GaAs	0.185	0.369	0.335	5.681	5.689	1.2	1.16	-0.034	-0.04
CdS	0.288	1.008	1.0	5.846	5.853	2.053	2.044	-0.007	-0.009

Table 5.12: Wurtzite Structures

System	σ^{A}_{300}	$E^{PBEsol}_{g,0}$	$E^{PBEsol}_{g,300}$	$E^{HSE06}_{g,0}$	$E^{HSE06}_{g,300}$	ΔE^{PBEsol}_{g}	ΔE^{HSE06}_{g}
ZnO	0.26126	0.70893	0.7003	2.4406	2.42584	-8.62	-14.76
ZnSe	0.2623	1.27261	1.24344	2.38015	2.34529	-29.17	-34.86
CdSe	0.31413	0.5277	0.52021	1.45646	1.44693	-7.48	-9.54
CdS	0.28724	1.09018	1.08022	2.14711	2.13495	-9.96	-12.16
MgTe	0.27212	2.33304	2.31154	3.24429	3.21994	-21.5	-24.35
ZnS	0.24267	2.15619	2.12423	3.42154	3.38463	-31.96	-36.91

Table 5.13: Fluorite and antifluorite Structures

System	σ^{A}_{300}	$E^{PBEsol}_{g,0}$	$E^{PBEsol}_{g,300}$	a_0	a_{300}	$E^{HSE06}_{g,0}$	$E^{HSE06}_{g,300}$	ΔE^{PBEsol}_{g}	ΔE^{HSE06}_{g}
K_2S	0.35866	2.3437	2.28214	7.34288	7.40489	3.3486	3.27553	-61.56	-73.08
Rb_2Se	0.3681	1.77041	1.73793	7.97062	8.0395	2.66965	2.62571	-32.47	-43.94
K_2O	0.38829	1.85088	1.71812	6.36583	6.44976	3.14198	2.98583	-132.76	-156.15
Rb_2O	0.47681	1.37798	1.23625	6.73157	6.83339	2.63385	2.46467	-141.73	-169.18
Li_2O	0.28575	4.85498	4.80244	4.59246	4.63723	6.58904	6.51987	-52.53	-69.16
Na_2Te	0.37855	1.99884	1.9366	7.25975	7.31646	2.83188	2.75838	-62.24	-73.5
CdF_2	0.41829	2.97451	2.90729	5.39362	5.42784	5.15672	5.07902	-67.23	-77.7
SrF_2	0.30611	6.73702	6.63776	5.78194	5.8181	8.94265	8.83525	-99.26	-107.34
K_2Te	0.38024	2.14434	2.08335	8.11736	8.18479	2.94068	2.86988	-60.99	-70.79
Li_2S	0.30653	3.20744	3.22508	5.67797	5.72496	4.30221	4.31356	17.65	11.35
Li_2Te	0.35856	2.38102	2.40772	6.46147	6.50685	3.15665	3.18127	26.71	24.62
Na_2S	0.33714	2.41257	2.34893	6.51605	6.56054	3.46594	3.39113	-63.64	-74.8
Na_2Se	0.35612	2.0024	1.9148	6.76791	6.83738	2.94458	2.84052	-87.6	-104.06
CaF_2	0.3168	7.07279	6.95861	5.43612	5.47241	9.29982	9.1772	-114.18	-122.62
Li_2Se	0.3292	2.8157	2.83898	5.95429	6.00513	3.76357	3.78181	23.29	18.24

Bibliography

[1] S. G. Louie, Y. H. Chan, F. H. da Jornada, Z. Li, and D. Y. Qiu, "Discovering and understanding materials through computation," *Nature Materials*, vol. 20, no. 6, pp. 728–735, 2021.

[2] N. Marzari, A. Ferretti, and C. Wolverton, "Electronic-structure methods for materials design," *Nature Materials*, vol. 20, no. 6, pp. 736–749, 2021.

[3] X. Gonze *et al.*, "The ABINIT project: impact, environment and recent developments," *Computer Physics Communications*, vol. 248, p. 107042, 2020.

[4] G. Kresse and J. Hafner, "Ab initio molecular dynamics for liquid metals," *Physical Review B*, vol. 47, pp. 558–561, 1993.

[5] V. Blum, R. Gehrke, F. Hanke, P. Havu, V. Havu, X. Ren, K. Reuter, and M. Scheffler, "Ab initio molecular simulations with numeric atom-centered orbitals," *Computer Physics Communications*, vol. 180, no. 11, pp. 2175–2196, 2009.

[6] P. Giannozzi *et al.*, "Quantum Espresso: a modular and open-source software project for quantum simulations of materials," *Journal of Physics: Condensed Matter*, vol. 21, no. 39, p. 395502, 2009.

[7] J. Ziman, *Electrons and Phonons: the theory of transport phenomena in solids*. Oxford University Press, 2001.

[8] G. Grimvall, "The electron-phonon interaction in normal metals," *Physica Scripta*, vol. 14, no. 1-2, pp. 63–78, 1976.

[9] M. N. D. Ashcroft, Neil W., *Solid state physics*. New York: Holt, Rinehart and Winston, 1976.

[10] D. Olguín, M. Cardona, and A. Cantarero, "Electron-phonon effects on the direct band gap in semiconductors: LCAO calculations," *Solid State Communications*, vol. 122, no. 11, pp. 575–589, 2002.

[11] B. Fultz, "Vibrational thermodynamics of materials," *Progress in Materials Science*, vol. 55, no. 4, pp. 247–352, 2010.

[12] M. Cardona, "Renormalization of the optical response of semiconductors by electron-phonon interaction," *Physica Status Solidi (A) Applied Research*, vol. 188, no. 4, pp. 1209–1232, 2001.

[13] M. Cardona and M. L. W. Thewalt, "Isotope effects on the optical spectra of semiconductors," *Reviews of Modern Physics*, vol. 77, pp. 1173–1224, 2005.

[14] R. B. Capaz, C. D. Spataru, P. Tangney, M. L. Cohen, and S. G. Louie, "Temperature dependence of the band gap of semiconducting carbon nanotubes," *Physical Review Letters*, vol. 94, p. 036801, 2005.

[15] S. Poncé, G. Antonius, Y. Gillet, P. Boulanger, J. Laflamme Janssen, A. Marini, M. Côté, and X. Gonze, "Temperature dependence of electronic eigenenergies in the adiabatic harmonic approximation," *Physical Review B*, vol. 90, p. 214304, 2014.

[16] S. Poncé, Y. Gillet, J. Laflamme Janssen, A. Marini, M. Verstraete, and X. Gonze, "Temperature dependence of the electronic structure of semiconductors and insulators," *The Journal of Chemical Physics*, vol. 143, no. 10, p. 102813, 2015.

[17] B. Monserrat and R. J. Needs, "Comparing electron-phonon coupling strength in diamond, silicon, and silicon carbide: First-principles study," *Physical Review B*, vol. 89, p. 214304, 2014.

[18] W. A. Saidi, S. Poncé, and B. Monserrat, "Temperature dependence of the energy levels of methylammonium lead iodide perovskite from first-principles," *Journal of Physical Chemistry Letters*, vol. 7, no. 24, pp. 5247–5252, 2016.

[19] B. Monserrat and D. Vanderbilt, "Temperature effects in the band structure of topological insulators," *Physical Review Letters*, vol. 117, p. 226801, 2016.

[20] P. Han and G. Bester, "First-principles calculation of the electron-phonon interaction in semiconductor nanoclusters," *Physical Review B*, vol. 85, p. 235422, 2012.

[21] P. Han and G. Bester, "Large nuclear zero-point motion effect in semiconductor nanoclusters," *Physical Review B*, vol. 88, p. 165311, 2013.

[22] V.-A. Ha, G. Volonakis, H. Lee, M. Zacharias, and F. Giustino, "Quasiparticle band structure and phonon-induced band gap renormalization of the lead-free halide double perovskite $Cs_2InAgCl_6$," *The Journal of Chemical Physics C*, vol. 125, no. 39, pp. 21689–21700, 2021.

[23] W. Shockley and J. Bardeen, "Energy bands and mobilities in monatomic semiconductors," *Physical Review*, vol. 77, no. 3, pp. 407–408, 1950.

[24] J.-J. Zhou and M. Bernardi, "Ab initio electron mobility and polar phonon scattering in gaas," *Physical Review B*, vol. 94, p. 201201, 2016.

[25] S. Poncé, E. R. Margine, and F. Giustino, "Towards predictive many-body calculations of phonon-limited carrier mobilities in semiconductors," *Physical Review B*, vol. 97, p. 121201, 2018.

[26] C.-H. Park, N. Bonini, T. Sohier, G. Samsonidze, B. Kozinsky, M. Calandra, F. Mauri, and N. Marzari, "Electron–phonon interactions and the intrinsic electrical resistivity of graphene," *Nano Letters*, vol. 14, no. 3, pp. 1113–1119, 2014.

[27] B. Xu and M. J. Verstraete, "First principles explanation of the positive seebeck coefficient of lithium," *Physical Review Letters*, vol. 112, p. 196603, 2014.

[28] S. Poncé, W. Li, S. Reichardt, and F. Giustino, "First-principles calculations of charge carrier mobility and conductivity in bulk semiconductors and two-dimensional materials," *Reports on Progress in Physics*, vol. 83, no. 3, p. 036501, 2020.

[29] S. Poncé, F. Macheda, E. R. Margine, N. Marzari, N. Bonini, and F. Giustino, "First-principles predictions of hall and drift mobilities in semiconductors," *Physical Review Research*, vol. 3, p. 043022, 2021.

[30] N.-E. Lee, J.-J. Zhou, L. A. Agapito, and M. Bernardi, "Charge transport in organic molecular semiconductors from first principles: The bandlike hole mobility in a naphthalene crystal," *Physical Review B*, vol. 97, p. 115203, 2018.

[31] J. I. Mustafa, M. Bernardi, J. B. Neaton, and S. G. Louie, "Ab initio electronic relaxation times and transport in noble metals," *Physical Review B*, vol. 94, p. 155105, 2016.

[32] B. K. Chang, J. J. Zhou, N. E. Lee, and M. Bernardi, "Intermediate polaronic charge transport in organic crystals from a many-body first-principles approach," *npj Computational Materials*, vol. 8, no. 1, 2022.

[33] M. Bernardi, D. Vigil-Fowler, C. S. Ong, J. B. Neaton, and S. G. Louie, "Ab initio study of hot electrons in GaAs," *Proceedings of the National Academy of Sciences*, vol. 112, no. 17, pp. 5291–5296, 2015.

[34] V. A. Jhalani, J.-J. Zhou, and M. Bernardi, "Ultrafast hot carrier dynamics in GaN and its impact on the efficiency droop," *Nano Letters*, vol. 17, no. 8, pp. 5012–5019, 2017.

[35] L. H. Hall, J. Bardeen, and F. J. Blatt, "Infrared absorption spectrum of germanium," *Physical Review*, vol. 95, pp. 559–560, 1954.

[36] K. Frohna, T. Deshpande, J. Harter, W. Peng, B. A. Barker, J. B. Neaton, S. G. Louie, O. M. Bakr, D. Hsieh, and M. Bernardi, "Inversion symmetry and bulk rashba effect in methylammonium lead iodide perovskite single crystals," *Nature Communications*, vol. 9, no. 1, p. 1829, 2018.

[37] C.-H. Park, F. Giustino, C. D. Spataru, M. L. Cohen, and S. G. Louie, "Angle-resolved photoemission spectra of graphene from first-principles calculations," *Nano Letters*, vol. 9, no. 12, pp. 4234–4239, 2009.

[38] M. Bernardi, D. Vigil-Fowler, J. Lischner, J. B. Neaton, and S. G. Louie, "Ab initio study of hot carriers in the first picosecond after sunlight absorption in silicon," *Physical Review Letters*, vol. 112, p. 257402, 2014.

[39] M. Zacharias, C. E. Patrick, and F. Giustino, "Stochastic approach to phonon-assisted optical absorption," *Physical Review Letters*, vol. 115, p. 177401, 2015.

[40] H. Fröhlich, "Electrons in lattice fields," *Advances in Physics*, vol. 3, no. 11, pp. 325–361, 1954.

[41] M. Schlipf, S. Poncé, and F. Giustino, "Carrier lifetimes and polaronic mass enhancement in the hybrid halide perovskite $CH_3NH_3PbI_3$ from multiphonon Fröhlich coupling," *Physical Review Letters*, vol. 121, p. 086402, 2018.

[42] P. Vogl, "Microscopic theory of electron-phonon interaction in insulators or semiconductors," *Physical Review B*, vol. 13, pp. 694–704, 1976.

[43] C. Verdi and F. Giustino, "Fröhlich electron-phonon vertex from first principles," *Physical Review Letters*, vol. 115, p. 176401, 2015.

[44] C. Franchini, M. Reticcioli, M. Setvin, and U. Diebold, "Polarons in materials," *Nature Reviews Materials*, vol. 6, 2021.

[45] L. N. Cooper, "Bound electron pairs in a degenerate fermi gas," *Physical Review*, vol. 104, pp. 1189–1190, 1956.

[46] J. Bardeen, L. N. Cooper, and J. R. Schrieffer, "Microscopic theory of superconductivity," *Physical Review*, vol. 106, pp. 162–164, 1957.

[47] P. Hohenberg and W. Kohn, "Inhomogeneous electron gas," *Physical Review*, vol. 136, pp. B864–B871, 1964.

[48] W. Kohn and L. J. Sham, "Self-consistent equations including exchange and correlation effects," *Physical Review*, vol. 140, pp. A1133–A1138, 1965.

[49] W. Kohn, "Nobel lecture: Electronic structure of matter—wave functions and density functionals," *Reviews of Modern Physics*, vol. 71, pp. 1253–1266, 1999.

[50] R. O. Jones, "Density functional theory: its origins, rise to prominence, and future," *Reviews of Modern Physics*, vol. 87, pp. 897–923, 2015.

[51] S. Baroni, S. de Gironcoli, A. Dal Corso, and P. Giannozzi, "Phonons and related crystal properties from density-functional perturbation theory," *Reviews of Modern Physics*, vol. 73, pp. 515–562, 2001.

[52] F. Giustino, S. G. Louie, and M. L. Cohen, "Electron-phonon renormalization of the direct band gap of diamond," *Physical Review Letters*, vol. 105, p. 265501, 2010.

[53] H. Y. Fan, "Temperature dependence of the energy gap in monatomic semiconductors," *Physical Review*, vol. 78, pp. 808–809, 1950.

[54] H. Y. Fan, "Temperature dependence of the energy gap in semiconductors," *Physical Review*, vol. 82, pp. 900–905, 1951.

[55] E. Anton, T. Physics, and P. On, "On the theory of temperature shift of the absoption curve in non-polar crystals," vol. 5, pp. 449–461, 1955.

[56] J. Bardeen and D. Pines, "Electron-phonon interaction in metals," *Physical Review*, vol. 99, pp. 1140–1150, 1955.

[57] P. B. Allen and V. Heine, "Theory of the temperature dependence of electronic band structures," *Journal of Physics C: Solid State Physics*, vol. 9, no. 12, pp. 2305–2312, 1976.

[58] P. B. Allen and M. Cardona, "Theory of the temperature dependence of the direct gap of germanium," *Physical Review B*, vol. 23, pp. 1495–1505, 1981.

[59] R. D. King-Smith, R. J. Needs, V. Heine, and M. J. Hodgson, "A first-principle calculation of the temperature dependence of the indirect band gap of silicon," *Europhysics Letters (EPL)*, vol. 10, no. 6, pp. 569–574, 1989.

[60] F. Giustino, "Electron-phonon interactions from first principles," *Reviews of Modern Physics*, vol. 89, no. 1, pp. 1–63, 2017.

[61] M. Bernardi, "First-principles dynamics of electrons and phonons," *European Physical Journal B*, vol. 89, no. 11, pp. 1–14, 2016.

[62] B. Monserrat, "Electron–phonon coupling from finite differences," *Journal of Physics: Condensed Matter*, vol. 30, no. 8, p. 083001, 2018.

[63] S. Poncé, E. Margine, C. Verdi, and F. Giustino, "EPW: Electron–phonon coupling, transport and superconducting properties using maximally localized wannier functions," *Computer Physics Communications*, vol. 209, pp. 116–133, 2016.

[64] J. Noffsinger, F. Giustino, B. D. Malone, C.-H. Park, S. G. Louie, and M. L. Cohen, "EPW: a program for calculating the electron–phonon coupling using maximally localized wannier functions," *Computer Physics Communications*, vol. 181, no. 12, pp. 2140–2148, 2010.

[65] J.-J. Zhou, J. Park, I.-T. Lu, I. Maliyov, X. Tong, and M. Bernardi, "Perturbo: a software package for ab initio electron–phonon interactions, charge transport and ultrafast dynamics," *Computer Physics Communications*, vol. 264, p. 107970, 2021.

[66] A. H. Romero *et al.*, "ABINIT: overview, and focus on selected capabilities," *The Journal of Chemical Physics.*, vol. 152, p. 124102, 2020.

[67] K. Bourzac, "Supercomputing poised for a massive speed boost," *Nature*, vol. 551, no. 7682, pp. 554–556, 2017.

[68] F. Knoop, T. A. R. Purcell, M. Scheffler, and C. Carbogno, "Anharmonicity measure for materials," *Physical Review Materials*, vol. 4, p. 083809, 2020.

[69] O. Hellman, I. A. Abrikosov, and S. I. Simak, "Lattice dynamics of anharmonic solids from first principles," *Physical Review B*, vol. 84, p. 180301, 2011.

[70] O. Hellman and I. A. Abrikosov, "Temperature-dependent effective third-order interatomic force constants from first principles," *Physical Review B*, vol. 88, p. 144301, 2013.

[71] O. Hellman, P. Steneteg, I. A. Abrikosov, and S. I. Simak, "Temperature dependent effective potential method for accurate free energy calculations of solids," *Physical Review B*, vol. 87, p. 104111, 2013.

[72] I. Errea, M. Calandra, and F. Mauri, "First-principles theory of anharmonicity and the inverse isotope effect in superconducting palladium-hydride compounds," *Physical Review Letters*, vol. 111, p. 177002, 2013.

[73] R. Bianco, I. Errea, L. Paulatto, M. Calandra, and F. Mauri, "Second-order structural phase transitions, free energy curvature, and temperature-dependent anharmonic phonons in the self-consistent harmonic approximation: Theory and stochastic implementation," *Physical Review B*, vol. 96, p. 014111, 2017.

[74] I. Errea, M. Calandra, C. J. Pickard, J. Nelson, R. J. Needs, Y. Li, H. Liu, Y. Zhang, Y. Ma, and F. Mauri, "High-pressure hydrogen sulfide from first principles: A strongly anharmonic phonon-mediated superconductor," *Physical Review Letters*, vol. 114, p. 157004, 2015.

[75] I. Errea, F. Belli, L. Monacelli, A. Sanna, T. Koretsune, T. Tadano, R. Bianco, M. Calandra, R. Arita, F. Mauri, and J. A. Flores-Livas, "Quantum crystal structure in the 250-Kelvin superconducting lanthanum hydride," *Nature*, 2020.

[76] Y.-N. Wu, W. A. Saidi, J. K. Wuenschell, T. Tadano, P. Ohodnicki, B. Chorpening, and Y. Duan, "Anharmonicity explains temperature renormalization effects of the band gap in $SrTiO_3$," *Journal of Physical Chemistry Letters*, vol. 11, no. 7, pp. 2518–2523, 2020.

[77] J.-J. Zhou, O. Hellman, and M. Bernardi, "Electron-phonon scattering in the presence of soft modes and electron mobility in $SrTiO_3$ perovskite from first principles," *Physical Review Letters*, vol. 121, p. 226603, 2018.

[78] J.-J. Zhou and M. Bernardi, "Predicting charge transport in the presence of polarons: The beyond-quasiparticle regime in $SrTiO_3$," *Physical Review Research*, vol. 1, p. 033138, 2019.

[79] G. Galli, R. M. Martin, R. Car, and M. Parrinello, "Structural and electronic properties of amorphous carbon," *Physical Review Letters*, vol. 62, pp. 555–558, 1989.

[80] T. B. Boykin, N. Kharche, G. Klimeck, and M. Korkusinski, "Approximate bandstructures of semiconductor alloys from tight-binding supercell calculations," *Journal of Physics Condensed Matter*, vol. 19, no. 3, 2007.

[81] V. Popescu and A. Zunger, "Extracting E versus k - effective band structure from supercell calculations on alloys and impurities," *Physical Review B*, no. 8, pp. 1–12.

[82] W. Ku, T. Berlijn, and C. C. Lee, "Unfolding first-principles band structures," *Physical Review Letters*, vol. 104, no. 21, pp. 1–4, 2010.

[83] P. B. Allen, T. Berlijn, D. A. Casavant, and J. M. Soler, "Recovering hidden Bloch character: Unfolding electrons, phonons, and slabs," *Physical Review B*, vol. 87, no. 8, pp. 1–10, 2013.

[84] P. V. Medeiros, S. S. Tsirkin, S. Stafström, and J. Björk, "Unfolding spinor wave functions and expectation values of general operators: Introducing the unfolding-density operator," *Physical Review B*, vol. 91, no. 4, pp. 1–3, 2015.

[85] M. Zacharias, M. Scheffler, and C. Carbogno, "Fully anharmonic nonperturbative theory of vibronically renormalized electronic band structures," *Physical Review B*, vol. 102, p. 045126, 2020.

[86] H. Teisseyre, P. Perlin, T. Suski, I. Grzegory, S. Porowski, J. Jun, A. Pietraszko, and T. D. Moustakas, "Temperature dependence of the energy gap in GaN bulk single crystals and epitaxial layer," *Journal of Applied Physics*, vol. 76, no. 4, pp. 2429–2434, 1994.

[87] G. Ramírez-Flores, H. Navarro-Contreras, A. Lastras-Martínez, R. C. Powell, and J. E. Greene, "Temperature-dependent optical band gap of the metastable zinc blende structure β-GaN," *Physical Review B*, vol. 50, pp. 8433–8438, 1994.

[88] J. Petalas, S. Logothetidis, S. Boultadakis, M. Alouani, and J. M. Wills, "Optical and electronic-structure study of cubic and hexagonal GaN thin films," *Physical Review B*, vol. 52, pp. 8082–8091, 1995.

[89] S. Logothetidis, J. Petalas, H. M. Polatoglou, and D. Fuchs, "Origin and temperature dependence of the first direct gap of diamond," *Physical Review B*, vol. 46, pp. 4483–4494, 1992.

[90] M. E. Levinshtein, S. L. Rumyantsev, and M. S. Shur, *Properties of Advanced Semiconductor Materials: GaN, AlN, InN, BN, SiC, SiGe*. John Wiley & Sons, 2001.

[91] R. Ramírez, C. P. Herrero, and E. R. Hernández, "Path-integral molecular dynamics simulation of diamond," *Physical Review B*, vol. 73, p. 245202, 2006.

[92] H. Kawai, K. Yamashita, E. Cannuccia, and A. Marini, "Electron-electron and electron-phonon correlation effects on the finite-temperature electronic and optical properties of zinc-blende GaN," *Physical Review B*, vol. 89, p. 085202, 2014.

[93] J. P. Nery and P. B. Allen, "Influence of Fröhlich polaron coupling on renormalized electron bands in polar semiconductors: Results for zinc-blende GaN," *Physical Review B*, vol. 94, p. 115135, 2016.

[94] H. Shang, J. Zhao, and J. Yang, "Assessment of the mass factor for the electron–phonon coupling in solids," *The Journal of Chemical Physics C*, vol. 125, no. 11, pp. 6479–6485, 2021.

[95] F. Giustino, *Materials modelling using density functional theory: properties and predictions*. Oxford University Press, 2014.

[96] J. Kohanoff, *Electronic Structure Calculations for Solids and Molecules Theory and Computational Methods*. Cambridge University Press, 2006.

[97] R. M. Martin, *Electronic Structure Basic Theory and Practical Methods*. Cambridge University Press, 2004.

[98] H. A. Bethe and E. E. Salpeter, *Quantum mechanics of one-and two-electron atoms*. Springer Science & Business Media, 2012.

[99] M. Born and R. Oppenheimer, "Zur quantentheorie der molekeln," *Annalen der Physik*, vol. 389, no. 20, pp. 457–484, 1927.

[100] N. C. Handy and A. M. Lee, "The adiabatic approximation," *Chemical Physics Letters*, vol. 252, no. 5, pp. 425–430, 1996.

[101] A. Szabo and N. Ostlund, *Modern Quantum Chemistry: Introduction to Advanced Electronic Structure Theory*. Dover Books on Chemistry, Dover Publications, 1996.

[102] C. Cramer, *Essentials of Computational Chemistry: Theories and Models*. Wiley, 2004.

[103] F. Jensen, *Introduction to Computational Chemistry*. Wiley, 2017.

[104] D. R. Hartree, "The wave mechanics of an atom with a non-coulomb central field. Part I. Theory and methods," *Mathematical Proceedings of the Cambridge Philosophical Society*, vol. 24, no. 1, p. 89–110, 1928.

[105] V. Fock, "Näherungsmethode zur lösung des quantenmechanischen mehrkörperproblems," *Zeitschrift für Physik*, vol. 61, no. 1, pp. 126–148, 1930.

[106] J. C. Slater, "A simplification of the Hartree-Fock method," *Physical Review*, vol. 81, pp. 385–390, 1951.

[107] R. J. Bartlett and M. Musiał, "Coupled-cluster theory in quantum chemistry," *Reviews of Modern Physics*, vol. 79, pp. 291–352, 2007.

[108] L. H. Thomas, "The calculation of atomic fields," *Mathematical Proceedings of the Cambridge Philosophical Society*, vol. 23, no. 5, p. 542–548, 1927.

[109] E. Fermi, "Eine statistische methode zur bestimmung einiger eigenschaften des atoms und ihre anwendung auf die theorie des periodischen systems der elemente," *Zeitschrift für Physik*, vol. 48, no. 1, pp. 73–79, 1928.

[110] R. Dreizler and E. Gross, *Density Functional Theory: an approach to the quantum many-body problem*. Springer Berlin Heidelberg, 2012.

[111] E. Engel and R. Dreizler, *Density Functional Theory: an advanced course*. Theoretical and Mathematical Physics, Springer Berlin Heidelberg, 2011.

[112] J. P. Perdew and K. Schmidt, "Jacob's ladder of density functional approximations for the exchange-correlation energy," *AIP Conference Proceedings*, vol. 577, no. 1, pp. 1–20, 2001.

[113] A. J. Cohen, P. Mori-Sánchez, and W. Yang, "Challenges for density functional theory," *Chemical Reviews*, vol. 112, no. 1, pp. 289–320, 2012.

[114] J. P. Perdew, K. Burke, and M. Ernzerhof, "Generalized gradient approximation made simple," *Physical Review Letters*, vol. 77, pp. 3865–3868, 1996.

[115] J. P. Perdew, A. Ruzsinszky, G. I. Csonka, O. A. Vydrov, G. E. Scuseria, L. A. Constantin, X. Zhou, and K. Burke, "Restoring the density-gradient expansion for exchange in solids and surfaces," *Physical Review Letters*, vol. 100, p. 136406, 2008.

[116] J. Heyd, G. E. Scuseria, and M. Ernzerhof, "Hybrid functionals based on a screened coulomb potential," *The Journal of Chemical Physics*, vol. 118, no. 18, pp. 8207–8215, 2003.

[117] A. V. Krukau, O. A. Vydrov, A. F. Izmaylov, and G. E. Scuseria, "Influence of the exchange screening parameter on the performance of screened hybrid functionals," *The Journal of Chemical Physics*, vol. 125, no. 22, p. 224106, 2006.

[118] P. A. Dirac, "Note on exchange phenomena in the Thomas atom," in *Mathematical proceedings of the Cambridge philosophical society*, vol. 26, pp. 376–385, Cambridge University Press, 1930.

[119] T. Chachiyo, "Communication: simple and accurate uniform electron gas correlation energy for the full range of densities," *The Journal of Chemical Physics*, vol. 145, no. 2, p. 021101, 2016.

[120] D. M. Ceperley and B. J. Alder, "Ground state of the electron gas by a stochastic method," *Physical Review Letters*, vol. 45, pp. 566–569, 1980.

[121] J. P. Perdew and Y. Wang, "Accurate and simple analytic representation of the electron-gas correlation energy," *Physical Review B*, vol. 45, pp. 13244–13249, 1992.

[122] P. Haas, F. Tran, and P. Blaha, "Calculation of the lattice constant of solids with semilocal functionals," *Physical Review B*, vol. 79, p. 085104, 2009.

[123] G.-X. Zhang, A. M. Reilly, A. Tkatchenko, and M. Scheffler, "Performance of various density-functional approximations for cohesive properties of 64 bulk solids," *New Journal of Physics*, vol. 20, no. 6, p. 063020, 2018.

[124] J. P. Perdew, "Density functional theory and the band gap problem," *International Journal of Quantum Chemistry*, vol. 28, no. S19, pp. 497–523, 1985.

[125] A. Seidl, A. Görling, P. Vogl, J. A. Majewski, and M. Levy, "Generalized Kohn-Sham schemes and the band gap problem," *Physical Review B*, vol. 53, pp. 3764–3774, 1996.

[126] P. Mori-Sánchez, A. J. Cohen, and W. Yang, "Localization and delocalization errors in density functional theory and implications for band-gap prediction," *Physical Review Letters*, vol. 100, p. 146401, 2008.

[127] J. P. Perdew *et al.*, "Understanding band gaps of solids in generalized Kohn–Sham theory," *Proceedings of the National Academy of Sciences*, vol. 114, no. 11, pp. 2801–2806, 2017.

[128] J. P. Perdew and M. Levy, "Physical content of the exact Kohn-Sham orbital energies: band gaps and derivative discontinuities," *Physical Review Letters*, vol. 51, pp. 1884–1887, 1983.

[129] L. J. Sham and M. Schlüter, "Density-functional theory of the energy gap," *Physical Review Letters*, vol. 51, pp. 1888–1891, 1983.

[130] W. Yang, Y. Zhang, and P. W. Ayers, "Degenerate ground states and a fractional number of electrons in density and reduced density matrix functional theory," *Physical Review Letters*, vol. 84, pp. 5172–5175, 2000.

[131] P. Mori-Sánchez, A. J. Cohen, and W. Yang, "Discontinuous nature of the exchange-correlation functional in strongly correlated systems," *Physical Review Letters*, vol. 102, p. 066403, 2009.

[132] A. J. Cohen, P. Mori-Sánchez, and W. Yang, "Fractional charge perspective on the band gap in density-functional theory," *Physical Review B*, vol. 77, p. 115123, 2008.

[133] J. P. Perdew and A. Zunger, "Self-interaction correction to density-functional approximations for many-electron systems," *Physical Review B*, vol. 23, pp. 5048–5079, 1981.

[134] J. P. Perdew, R. G. Parr, M. Levy, and J. L. Balduz, "Density-functional theory for fractional particle number: derivative discontinuities of the energy," *Physical Review Letters*, vol. 49, pp. 1691–1694, 1982.

[135] J. P. Perdew, M. Ernzerhof, and K. Burke, "Rationale for mixing exact exchange with density functional approximations," *The Journal of Chemical Physics*, vol. 105, no. 22, pp. 9982–9985, 1996.

[136] J. Heyd and G. E. Scuseria, "Efficient hybrid density functional calculations in solids: assessment of the Heyd–Scuseria–Ernzerhof screened coulomb hybrid functional," *The Journal of Chemical Physics*, vol. 121, no. 3, pp. 1187–1192, 2004.

[137] A. J. Garza and G. E. Scuseria, "Predicting band gaps with hybrid density functionals," *Journal of Physical Chemistry Letters*, vol. 7, no. 20, pp. 4165–4170, 2016.

[138] S. J. Clark and J. Robertson, "Screened exchange density functional applied to solids," *Physical Review B*, vol. 82, p. 085208, 2010.

[139] T. Körzdörfer and S. Kümmel, "Single-particle and quasiparticle interpretation of Kohn-Sham and generalized Kohn-Sham eigenvalues for hybrid functionals," *Physical Review B*, vol. 82, p. 155206, 2010.

[140] P. Borlido, T. Aull, A. W. Huran, F. Tran, M. A. L. Marques, and S. Botti, "Large-scale benchmark of exchange–correlation functionals for the determination of electronic band

gaps of solids," *Journal of Chemical Theory and Computation*, vol. 15, no. 9, pp. 5069–5079, 2019.

[141] S. V. Levchenko, X. Ren, J. Wieferink, R. Johanni, P. Rinke, V. Blum, and M. Scheffler, "Hybrid functionals for large periodic systems in an all-electron, numeric atom-centered basis framework," *Computer Physics Communications*, vol. 192, pp. 60–69, 2015.

[142] G. Kresse and D. Joubert, "From ultrasoft pseudopotentials to the projector augmented-wave method," *Physical Review B*, vol. 59, pp. 1758–1775, 1999.

[143] M. J. Frisch *et al.*, "Gaussian16 revision C.01," 2016. Gaussian Inc. Wallingford CT.

[144] V. Havu, V. Blum, P. Havu, and M. Scheffler, "Efficient O(N) integration for all-electron electronic structure calculation using numeric basis functions," *Journal of Computational Physics*, vol. 228, no. 22, pp. 8367–8379, 2009.

[145] B. Delley, "An all-electron numerical method for solving the local density functional for polyatomic molecules," *The Journal of Chemical Physics*, vol. 92, no. 1, pp. 508–517, 1990.

[146] A. D. Becke, "A multicenter numerical integration scheme for polyatomic molecules," *The Journal of Chemical Physics*, vol. 88, no. 4, pp. 2547–2553, 1988.

[147] G. Kresse and J. Furthmüller, "Efficiency of ab-initio total energy calculations for metals and semiconductors using a plane-wave basis set," *Computational Materials Science*, vol. 6, no. 1, pp. 15–50, 1996.

[148] A. Marek, V. Blum, R. Johanni, V. Havu, B. Lang, T. Auckenthaler, A. Heinecke, H.-J. Bungartz, and H. Lederer, "The ELPA library: scalable parallel eigenvalue solutions for electronic structure theory and computational science," *Journal of Physics: Condensed Matter*, vol. 26, no. 21, p. 213201, 2014.

[149] P. Pulay, "Convergence acceleration of iterative sequences. The case of SCF iteration," *Chemical Physics Letters*, vol. 73, no. 2, pp. 393–398, 1980.

[150] C. Payne and N. York, "Iterative minimization techniques for ab initio total-energy calculations- molecular dynamics and conjugate gradients," vol. 64, no. 4, pp. 1–53, 2011.

[151] H. J. Monkhorst and J. D. Pack, "Special points for Brillouin zone integrations," *Physical Review B*, vol. 13, pp. 5188–5192, 1976.

[152] M. T. Dove, *Introduction to Lattice Dynamics*. Cambridge Topics in Mineral Physics and Chemistry, Cambridge University Press, 1993.

[153] D. Wallace, *Thermodynamics of Crystals*. Dover books on physics, Dover Publications, 1998.

[154] M. Born and K. Huang, *Dynamical Theory of Crystal Lattices*. International series of monographs on physics, Clarendon Press, 1988.

[155] D. Frenkel and B. Smit, *Understanding Molecular Simulation*. USA: Academic Press, Inc., 2nd ed., 2001.

[156] D. A. McQuarrie, *Statistical Mechanics*. Harper's chemistry series, New York: Harper Collins, 1976.

[157] H. Hellmann, "Zur rolle der kinetischen elektronenenergie für die zwischenatomaren kräfte," *Zeitschrift für Physik*, vol. 85, no. 3, pp. 180–190, 1933.

[158] R. P. Feynman, "Forces in molecules," *Physical Review*, vol. 56, pp. 340–343, 1939.

[159] P. Pulay, "Ab initio calculation of force constants and equilibrium geometries in polyatomic molecules," *Molecular Physics*, vol. 17, no. 2, pp. 197–204, 1969.

[160] R. Gehrke, *First-principles basin-hopping for the structure determination of atomic clusters*. PhD thesis, 2009.

[161] X. Gonze and J.-P. Vigneron, "Density-functional approach to nonlinear-response coefficients of solids," *Physical Review B*, vol. 39, pp. 13120–13128, 1989.

[162] K. Parlinski, Z. Q. Li, and Y. Kawazoe, "First-principles determination of the soft mode in cubic ZrO_2," *Physical Review Letters*, vol. 78, pp. 4063–4066, 1997.

[163] A. Togo, F. Oba, and I. Tanaka, "First-principles calculations of the ferroelastic transition between rutile-type and $cacl_2$-type sio_2 at high pressures," *Physical Review B*, vol. 78, p. 134106, 2008.

[164] A. Togo and I. Tanaka, "First principles phonon calculations in materials science," *Scripta Materialia*, vol. 108, pp. 1–5, 2015.

[165] F. Eriksson, E. Fransson, and P. Erhart, "The hiphive package for the extraction of high-order force constants by machine learning," *Advanced Theory and Simulations*, vol. 2, no. 5, p. 1800184, 2019.

[166] T. Tadano, Y. Gohda, and S. Tsuneyuki, "Anharmonic force constants extracted from first-principles molecular dynamics: applications to heat transfer simulations," *Journal of Physics: Condensed Matter*, vol. 26, no. 22, p. 225402, 2014.

[167] W. Li, J. Carrete, N. A. Katcho, and N. Mingo, "ShengBTE: a solver of the Boltzmann transport equation for phonons," *Computer Physics Communications*, vol. 185, no. 6, pp. 1747–1758, 2014.

[168] A. Togo and I. Tanaka, "Spglib: a software library for crystal symmetry search," *arXiv preprint arXiv:1808.01590*, vol. 471, 2018.

[169] M. J. L. Sangster, G. Peckham, and D. H. Saunderson, "Lattice dynamics of magnesium oxide," *Journal of Physics C: Solid State Physics*, vol. 3, no. 5, p. 1026, 1970.

[170] X. Gonze and C. Lee, "Dynamical matrices, born effective charges, dielectric permittivity tensors, and interatomic force constants from density-functional perturbation theory," *Physical Review B*, vol. 55, pp. 10355–10368, 1997.

[171] Y. Wang, J. J. Wang, W. Y. Wang, Z. G. Mei, S. L. Shang, L. Q. Chen, and Z. K. Liu, "A mixed-space approach to first-principles calculations of phonon frequencies for polar materials," *Journal of Physics: Condensed Matter*, vol. 22, no. 20, p. 202201, 2010.

[172] X. Gonze, J.-C. Charlier, D. Allan, and M. Teter, "Interatomic force constants from first principles: The case of α-quartz," *Physical Review B*, vol. 50, pp. 13035–13038, 1994.

[173] M. Royo, K. R. Hahn, and M. Stengel, "Using high multipolar orders to reconstruct the sound velocity in piezoelectrics from lattice dynamics," *Physical Review Letters*, vol. 125, p. 217602, 2020.

[174] P. Ghosez, J.-P. Michenaud, and X. Gonze, "Dynamical atomic charges: the case of ABO_3 compounds," *Physical Review B*, vol. 58, pp. 6224–6240, 1998.

[175] H. Shang, C. Carbogno, P. Rinke, and M. Scheffler, "Lattice dynamics calculations based on density-functional perturbation theory in real space," *Computer Physics Communications*, vol. 215, pp. 26–46, 2017.

[176] R. Resta, "Theory of the electric polarization in crystals," *Ferroelectrics*, vol. 136, no. 1, pp. 51–55, 1992.

[177] R. D. King-Smith and D. Vanderbilt, "Theory of polarization of crystalline solids," *Physical Review B*, vol. 47, no. 3, pp. 1651–1654, 1993.

[178] R. Resta, "Macroscopie electric polarization as a geometric quantum phase," *Epl*, vol. 22, no. 2, pp. 133–138, 1993.

[179] M. V. Berry and P. R. S. L. A, "Quantal phase factors accompanying adiabatic changes," *Proceedings of the Royal Society of London. A. Mathematical and Physical Sciences*, vol. 392, no. 1802, pp. 45–57, 1984.

[180] D. West and S. K. Estreicher, "First-principles calculations of vibrational lifetimes and decay channels: hydrogen-related modes in Si," *Physical Review Letters*, vol. 96, p. 115504, 2006.

[181] F. C. Yang, O. Hellman, and B. Fultz, "Temperature dependence of electron-phonon interactions in vanadium," *Physical Review B*, vol. 101, no. 9, pp. 1–9, 2020.

[182] F. Karsai, M. Engel, E. Flage-Larsen, and G. Kresse, "Electron–phonon coupling in semiconductors within the GW approximation," *New Journal of Physics*, vol. 20, no. 12, p. 123008, 2018.

[183] T. M. Gibbons, B. Kang, S. K. Estreicher, and C. Carbogno, "Thermal conductivity of si nanostructures containing defects: methodology, isotope effects, and phonon trapping," *Physical Review B*, vol. 84, p. 035317, 2011.

[184] N. Shulumba, Z. Raza, O. Hellman, E. Janzén, I. A. Abrikosov, and M. Odén, "Impact of anharmonic effects on the phase stability, thermal transport, and electronic properties of aln," *Physical Review B*, vol. 94, p. 104305, 2016.

[185] K. E. Atkinson, *An Introduction to Numerical Analysis*. New York: John Wiley & Sons, second ed., 1989.

[186] L. Verlet, "Computer experiments on classical fluids I. Thermodynamical properties of Lennard-Jones molecules," *Physical Review*, vol. 159, pp. 98–103, 1967.

[187] M. P. Allen and D. J. Tildesley, *Computer Simulation of Liquids*. Oxford University Press, 2017.

[188] G. Zheng, A. M. N. Niklasson, and M. Karplus, "Lagrangian formulation with dissipation of Born-Oppenheimer molecular dynamics using the density-functional tight-binding method," *The Journal of Chemical Physics*, vol. 135, no. 4, p. 044122, 2011.

[189] P. H. Hünenberger, *Thermostat Algorithms for Molecular Dynamics Simulations*, pp. 105–149. Berlin, Heidelberg: Springer Berlin Heidelberg, 2005.

[190] E. Vanden-Eijnden and G. Ciccotti, "Second-order integrators for Langevin equations with holonomic constraints," *Chemical Physics Letters*, vol. 429, no. 1, pp. 310–316, 2006.

[191] C. Cazorla and J. Boronat, "Simulation and understanding of atomic and molecular quantum crystals," *Reviews of Modern Physics*, vol. 89, p. 035003, 2017.

[192] T. E. Markland and M. Ceriotti, "Nuclear quantum effects enter the mainstream," *Nature Reviews Chemistry*, 2018.

[193] M. Rossi, "Progress and challenges in ab initio simulations of quantum nuclei in weakly bonded systems," *The Journal of Chemical Physics*, vol. 154, no. 17, p. 170902, 2021.

[194] J. A. Morrone and R. Car, "Nuclear quantum effects in water," *Physical Review Letters*, vol. 101, p. 017801, 2008.

[195] Y. Litman, D. Donadio, M. Ceriotti, and M. Rossi, "Decisive role of nuclear quantum effects on surface mediated water dissociation at finite temperature," *The Journal of Chemical Physics*, vol. 148, no. 10, p. 102320, 2018.

[196] M. E. Tuckerman, D. Marx, M. L. Klein, and M. Parrinello, "On the quantum nature of the shared proton in hydrogen bonds," *Science*, vol. 275, no. 5301, pp. 817–820, 1997.

[197] F. Knoop, *Heat transport in strongly anharmonic solids from first principles*. PhD thesis, Humboldt-Universität zu Berlin, Mathematisch-Naturwissenschaftliche Fakultät, 2022.

[198] A. Togo, L. Chaput, and I. Tanaka, "Distributions of phonon lifetimes in Brillouin zones," *Physical Review B*, vol. 91, p. 094306, 2015.

[199] N. R. Werthamer, "Self-consistent phonon formulation of anharmonic lattice dynamics," *Physical Review B*, vol. 1, pp. 572–581, 1970.

[200] I. Errea, M. Calandra, and F. Mauri, "Anharmonic free energies and phonon dispersions from the stochastic self-consistent harmonic approximation: application to platinum and palladium hydrides," *Physical Review B*, vol. 89, p. 064302, 2014.

[201] T. Tadano and S. Tsuneyuki, "Self-consistent phonon calculations of lattice dynamical properties in cubic $SrTiO_3$ with first-principles anharmonic force constants," *Physical Review B*, vol. 92, p. 054301, 2015.

[202] F. Birch, "Finite elastic strain of cubic crystals," *Physical Review*, vol. 71, pp. 809–824, 1947.

[203] F. D. Murnaghan, "The compressibility of media under extreme pressures," *Proceedings of the National Academy of Sciences*, vol. 30, no. 9, pp. 244–247, 1944.

[204] M. Hebbache and M. Zemzemi, "Ab initio study of high-pressure behavior of a low compressibility metal and a hard material: osmium and diamond," *Physical Review B*, vol. 70, p. 224107, 2004.

[205] P. Vinet, J. R. Smith, J. Ferrante, and J. H. Rose, "Temperature effects on the universal equation of state of solids," *Physical Review B*, vol. 35, pp. 1945–1953, 1987.

[206] M. Cardona, T. A. Meyer, and M. L. W. Thewalt, "Temperature dependence of the energy gap of semiconductors in the low-temperature limit," *Physical Review Letters*, vol. 92, p. 196403, 2004.

[207] M. Cardona, "Electron–phonon interaction in tetrahedral semiconductors," *Solid State Communications*, vol. 133, no. 1, pp. 3–18, 2005.

[208] C. J. Wort and R. S. Balmer, "Diamond as an electronic material," *Materials Today*, vol. 11, no. 1, pp. 22–28, 2008.

[209] J. Sjakste, N. Vast, M. Calandra, and F. Mauri, "Wannier interpolation of the electron-phonon matrix elements in polar semiconductors: Polar-optical coupling in gaas," *Physical Review B*, vol. 92, p. 054307, 2015.

[210] K. Baumann, "Effect of the zero-point motion on band structure: valence band of ^{3}He," *Physical Review B*, vol. 21, pp. 2063–2066, 1980.

[211] B. Monserrat, "Vibrational averages along thermal lines," *Physical Review B*, vol. 93, p. 014302, 2016.

[212] M. Zacharias and F. Giustino, "One-shot calculation of temperature-dependent optical spectra and phonon-induced band-gap renormalization," *Physical Review B*, vol. 94, p. 075125, 2016.

[213] A. Miglio *et al.*, "Predominance of non-adiabatic effects in zero-point renormalization of the electronic band gap," *npj Computational Materials*, vol. 6, no. 1, p. 167, 2020.

[214] B. Monserrat, N. D. Drummond, and R. J. Needs, "Anharmonic vibrational properties in periodic systems: energy, electron-phonon coupling, and stress," *Physical Review B*, vol. 87, p. 144302, 2013.

[215] B. Monserrat, G. J. Conduit, and R. J. Needs, "Extracting semiconductor band gap zero-point corrections from experimental data," *Physical Review B*, vol. 90, p. 184302, 2014.

[216] B. Monserrat, E. A. Engel, and R. J. Needs, "Giant electron-phonon interactions in molecular crystals and the importance of nonquadratic coupling," *Physical Review B*, vol. 92, p. 140302, 2015.

[217] J.-J. Zhou, J. Park, I. Timrov, A. Floris, M. Cococcioni, N. Marzari, and M. Bernardi, "Ab initio electron-phonon interactions in correlated electron systems," *Physical Review Letters*, vol. 127, p. 126404, 2021.

[218] V. I. Anisimov, J. Zaanen, and O. K. Andersen, "Band theory and Mott insulators: Hubbard U instead of Stoner I," *Physical Review B*, vol. 44, pp. 943–954, 1991.

[219] V. I. Anisimov, F. Aryasetiawan, and A. I. Lichtenstein, "First-principles calculations of the electronic structure and spectra of strongly correlated systems: the LDA+U method," *Journal of Physics: Condensed Matter*, vol. 9, no. 4, p. 767, 1997.

[220] A. Floris, I. Timrov, B. Himmetoglu, N. Marzari, S. de Gironcoli, and M. Cococcioni, "Hubbard-corrected density functional perturbation theory with ultrasoft pseudopotentials," *Physical Review B*, vol. 101, p. 064305, 2020.

[221] L. Hedin, "New method for calculating the one-particle Green's function with application to the electron-gas problem," *Physical Review*, vol. 139, pp. A796–A823, 1965.

[222] F. Aryasetiawan and O. Gunnarsson, "The GW method," *Reports on Progress in Physics*, vol. 61, no. 3, pp. 237–312, 1998.

[223] G. Antonius, S. Poncé, P. Boulanger, M. Côté, and X. Gonze, "Many-body effects on the zero-point renormalization of the band structure," *Physical Review Letters*, vol. 112, p. 215501, 2014.

[224] Z. Li, G. Antonius, M. Wu, F. H. da Jornada, and S. G. Louie, "Electron-phonon coupling from ab initio linear-response theory within the GW method: correlation-enhanced interactions and superconductivity in $Ba_{1-x}K_xBiO_3$," *Physical Review Letters*, vol. 122, p. 186402, 2019.

[225] Z. Li, M. Wu, Y.-H. Chan, and S. G. Louie, "Unmasking the origin of kinks in the photoemission spectra of cuprate superconductors," *Physical Review Letters*, vol. 126, p. 146401, 2021.

[226] A. Tamm, G. Samolyuk, A. A. Correa, M. Klintenberg, A. Aabloo, and A. Caro, "Electron-phonon interaction within classical molecular dynamics," *Physical Review B*, vol. 94, p. 024305, 2016.

[227] R. Ramírez, C. P. Herrero, E. R. Hernández, and M. Cardona, "Path-integral molecular dynamics simulation of 3C-SiC," *Physical Review B*, vol. 77, p. 045210, 2008.

[228] A. Kundu, M. Govoni, H. Yang, M. Ceriotti, F. Gygi, and G. Galli, "Quantum vibronic effects on the electronic properties of solid and molecular carbon," *Physical Review Materials*, vol. 5, p. L070801, 2021.

[229] K. Prasai, P. Biswas, and D. A. Drabold, "Electrons and phonons in amorphous semiconductors," *Semiconductor Science and Technology*, vol. 31, no. 7, p. 073002, 2016.

[230] M. Rossi, P. Gasparotto, and M. Ceriotti, "Anharmonic and quantum fluctuations in molecular crystals: a first-principles study of the stability of paracetamol," *Physical Review Letters*, vol. 117, p. 115702, 2016.

[231] T. B. Boykin and G. Klimeck, "Practical application of zone-folding concepts in tight-binding calculations," *Physical Review B*, vol. 71, no. 11, pp. 1–6, 2005.

[232] C. C. Lee, Y. Yamada-Takamura, and T. Ozaki, "Unfolding method for first-principles LCAO electronic structure calculations," *Journal of Physics Condensed Matter*, vol. 25, no. 34, 2013.

[233] H. Huang, F. Zheng, P. Zhang, J. Wu, B. L. Gu, and W. Duan, "A general group theoretical method to unfold band structures and its application," *New Journal of Physics*, vol. 16, 2014.

[234] M. Tomi, H. O. Jeschke, and R. Valent, "Unfolding of electronic structure through induced representations of space groups : application to Fe-based superconductors," vol. 195121, pp. 1–11, 2014.

[235] T. B. Boykin, A. Ajoy, H. Ilatikhameneh, M. Povolotskyi, and G. Klimeck, "Unfolding and effective bandstructure calculations as discrete real and reciprocal-space operations," *Physica B: Condensed Matter*, vol. 491, pp. 22–30, 2016.

[236] T. Kosugi, H. Nishi, Y. Kato, and Y. ichiro Matsushita, "Periodicity-free unfolding method of electronic energy spectra," *Journal of the Physical Society of Japan*, vol. 86, no. 12, pp. 1–8, 2017.

[237] A. Damascelli, Z. Hussain, and Z.-X. Shen, "Angle-resolved photoemission studies of the cuprate superconductors," *Reviews of Modern Physics*, vol. 75, pp. 473–541, 2003.

[238] B. R. Hoffmann and R. Hoffmann, "How chemistry and physics meet in the solid state," *Angewandte Chemie International Edition in English*, vol. 26, no. 9, pp. 846–878, 1987.

[239] V. Popescu and A. Zunger, "Effective band structure of random alloys," *Physical Review Letters*, vol. 104, no. 23, pp. 1–4, 2010.

[240] T. B. Boykin, A. Ajoy, H. Ilatikhameneh, M. Povolotskyi, and G. Klimeck, "Brillouin zone unfolding method for effective phonon spectra," *Physical Review B*, vol. 90, p. 205214, 2014.

[241] Y. Ikeda, A. Carreras, A. Seko, A. Togo, and I. Tanaka, "Mode decomposition based on crystallographic symmetry in the band-unfolding method," *Physical Review B*, vol. 95, p. 024305, 2017.

[242] L. W. Wang, L. Bellaiche, S. H. Wei, and A. Zunger, "Majority representation of alloy electronic states," *Physical Review Letters*, vol. 80, no. 21, pp. 4725–4728, 1998.

[243] M. W. Haverkort, I. S. Elfimov, and G. A. Sawatzky, "Electronic structure and self energies of randomly substituted solids using density functional theory and model calculations," pp. 1–14, 2011.

[244] O. Rubel, A. Bokhanchuk, S. J. Ahmed, and E. Assmann, "Unfolding the band structure of disordered solids: from bound states to high-mobility Kane fermions," *Physical Review B*, vol. 90, no. 11, pp. 1–8, 2014.

[245] A. B. Gordienko and A. V. Kosobutsky, "Analysis of the electronic structure of crystals through band structure unfolding," *Physics of the Solid State*, vol. 58, no. 3, pp. 462–468, 2016.

[246] M. Zacharias and F. Giustino, "Theory of the special displacement method for electronic structure calculations at finite temperature," *Physical Review Research*, vol. 2, p. 013357, 2020.

[247] Y. T. Lee, C. C. Lee, M. Fukuda, and T. Ozaki, "Unfolding optical transition weights of impurity materials for first-principles LCAO electronic structure calculations," *Physical Review B*, vol. 102, no. 7, pp. 1–9, 2020.

[248] P. V. Medeiros, S. Stafström, and J. Björk, "Effects of extrinsic and intrinsic perturbations on the electronic structure of graphene: retaining an effective primitive cell band structure by band unfolding," *Physical Review B*, vol. 89, no. 4, 2014.

[249] D. Dirnberger, G. Kresse, C. Franchini, and M. Reticcioli, "Electronic state unfolding for plane waves: energy bands, fermi surfaces, and spectral functions," *Journal of Physical Chemistry C*, vol. 125, no. 23, pp. 12921–12928, 2021.

[250] Y.-S. Lee, M. B. Nardelli, and N. Marzari, "Band structure and quantum conductance of nanostructures from maximally localized wannier functions: the case of functionalized carbon nanotubes," *Physical Review Letters*, vol. 95, p. 076804, 2005.

[251] I. Deretzis, G. Calogero, G. G. Angilella, and A. La Magna, "Role of basis sets on the unfolding of supercell band structures: from tight-binding to density functional theory," *Europhysics Letters*, vol. 107, no. 2, 2014.

[252] V. Alex, S. Finkbeiner, and J. Weber, "Temperature dependence of the indirect energy gap in crystalline silicon," *Journal of Applied Physics*, vol. 79, no. 9, pp. 6943–6946, 1996.

[253] A. Togo, L. Chaput, I. Tanaka, and G. Hug, "First-principles phonon calculations of thermal expansion in Ti_3SiC_2, Ti_3AlC_2, Ti_3GeC_2," *Physical Review B*, vol. 81, p. 174301, 2010.

[254] P. B. Allen, "Theory of thermal expansion: Quasi-harmonic approximation and corrections from quasi-particle renormalization," *Modern Physics Letters B*, vol. 34, no. 02, p. 2050025, 2019.

[255] V. Brousseau-Couture, E. Godbout, M. Côté, and X. Gonze, "Zero-point lattice expansion and band gap renormalization: Grüneisen approach versus free energy minimization," *Physical Review B*, vol. 106, p. 085137, 2022.

[256] S. Biernacki and M. Scheffler, "Negative thermal expansion of diamond and zinc-blende semiconductors," *Physical Review Letters*, vol. 63, pp. 290–293, 1989.

[257] D. S. Kim, O. Hellman, J. Herriman, H. L. Smith, J. Y. Y. Lin, N. Shulumba, J. L. Niedziela, C. W. Li, D. L. Abernathy, and B. Fultz, "Nuclear quantum effect with pure anharmonicity and the anomalous thermal expansion of silicon," *Proceedings of the National Academy of Sciences*, vol. 115, no. 9, pp. 1992–1997, 2018.

[258] G. D. Mahan, *Many Particle Physics, Third Edition*. New York: Plenum, 2000.

[259] V. Brousseau-Couture, X. Gonze, and M. Côté, "Effect of spin-orbit coupling on the zero-point renormalization of the electronic band gap in cubic materials: first-principles calculations and generalized Fröhlich model," *Physical Review B*, vol. 107, p. 115173, 2023.

[260] P. García-Risueño, P. Han, and G. Bester, "Frozen-phonon method for state anticrossing situations and its application to zero-point motion effects in diamondoids," 2019.

[261] D. G. Altman and J. M. Bland, "Standard deviations and standard errors," *Bmj*, vol. 331, no. 7521, p. 903, 2005.

[262] J. H. Lloyd-Williams and B. Monserrat, "Lattice dynamics and electron-phonon coupling calculations using nondiagonal supercells," *Physical Review B*, vol. 92, p. 184301, 2015.

[263] W. P. Huhn and V. Blum, "One-hundred-three compound band-structure benchmark of post-self-consistent spin-orbit coupling treatments in density functional theory," *Physical Review Materials*, vol. 1, p. 033803, 2017.

[264] R. Pässler, "Dispersion-related description of temperature dependencies of band gaps in semiconductors," *Physical Review B*, vol. 66, p. 085201, 2002.

[265] S. Poncé, G. Antonius, P. Boulanger, E. Cannuccia, A. Marini, M. Côté, and X. Gonze, "Verification of first-principles codes: Comparison of total energies, phonon frequencies, electron–phonon coupling and zero-point motion correction to the gap between ABINIT and QE/Yambo," *Computational Materials Science*, vol. 83, pp. 341–348, 2014.

[266] G. A. Slack and S. F. Bartram, "Thermal expansion of some diamondlike crystals," *Journal of Applied Physics*, vol. 46, no. 1, pp. 89–98, 1975.

[267] Y. Varshni, "Temperature dependence of the energy gap in semiconductors," *Physica*, vol. 34, no. 1, pp. 149–154, 1967.

[268] L. Viña, S. Logothetidis, and M. Cardona, "Temperature dependence of the dielectric function of germanium," *Physical Review B*, vol. 30, pp. 1979–1991, 1984.

[269] A. Manoogian and A. Leclerc, "Determination of the dilation and vibrational contributions to the energy band gaps in germanium and silicon," *Physica Status Solidi B*, vol. 92, no. 1, pp. K23–K27, 1979.

[270] A. T. Collins, S. C. Lawson, G. Davies, and H. Kanda, "Indirect energy gap of ^{13}C diamond," *Physical Review Letters*, vol. 65, pp. 891–894, 1990.

[271] K. P. O'Donnell and X. Chen, "Temperature dependence of semiconductor band gaps," *Applied Physics Letters*, vol. 58, no. 25, pp. 2924–2926, 1991.

[272] C. D. Clark, P. J. Dean, P. V. Harris, and W. C. Price, "Intrinsic edge absorption in diamond," *Proceedings of the Royal Society of London. Series A. Mathematical and Physical Sciences*, vol. 277, no. 1370, pp. 312–329, 1964.

[273] B. Monserrat, "Correlation effects on electron-phonon coupling in semiconductors: many-body theory along thermal lines," *Physical Review B*, vol. 93, p. 100301, 2016.

[274] C. Draxl and M. Scheffler, "The nomad laboratory: from data sharing to artificial intelligence," *Journal of Physics: Materials*, vol. 2, no. 3, p. 036001, 2019.

[275] F. Manjón, M. Mollar, B. Marí, N. Garro, A. Cantarero, R. Lauck, and M. Cardona, "Effect of isotopic mass on the photoluminescence spectra of β zinc sulfide," *Solid State Communications*, vol. 133, no. 4, pp. 253–258, 2005.

[276] P. Lautenschlager, M. Garriga, S. Logothetidis, and M. Cardona, "Interband critical points of gaas and their temperature dependence," *Physical Review B*, vol. 35, pp. 9174–9189, 1987.

[277] J. Bhosale, A. K. Ramdas, A. Burger, A. Muñoz, A. H. Romero, M. Cardona, R. Lauck, and R. K. Kremer, "Temperature dependence of band gaps in semiconductors: electron-phonon interaction," *Physical Review B*, vol. 86, p. 195208, 2012.

[278] C. Parks, A. K. Ramdas, S. Rodriguez, K. M. Itoh, and E. E. Haller, "Electronic band structure of isotopically pure germanium: modulated transmission and reflectivity study," *Physical Review B*, vol. 49, pp. 14244–14250, 1994.

[279] G. Petretto, S. Dwaraknath, H. P.C. Miranda, D. Winston, M. Giantomassi, M. J. van Setten, X. Gonze, K. A. Persson, G. Hautier, and G.-M. Rignanese, "High-throughput density-functional perturbation theory phonons for inorganic materials," *Scientific Data*, vol. 5, no. 1, p. 180065, 2018.

[280] J. P. Walter, R. R. L. Zucca, M. L. Cohen, and Y. R. Shen, "Temperature dependence of the wavelength-modulation spectra of GaAs," *Physical Review Letters*, vol. 24, pp. 102–104, 1970.

[281] G. Antonius, S. Poncé, E. Lantagne-Hurtubise, G. Auclair, X. Gonze, and M. Côté, "Dynamical and anharmonic effects on the electron-phonon coupling and the zero-point renormalization of the electronic structure," *Physical Review B*, vol. 92, p. 085137, 2015.

[282] J. P. Nery, P. B. Allen, G. Antonius, L. Reining, A. Miglio, and X. Gonze, "Quasiparticles and phonon satellites in spectral functions of semiconductors and insulators: cumulants applied to the full first-principles theory and the Fröhlich polaron," *Physical Review B*, vol. 97, p. 115145, 2018.

[283] Y. Zhang, Z. Wang, J. Xi, and J. Yang, "Temperature-dependent band gaps in several semiconductors: from the role of electron–phonon renormalization," *Journal of Physics: Condensed Matter*, vol. 32, no. 47, p. 475503, 2020.

[284] H.-H. Kowalski, *Theory of thermal conductivity.* PhD thesis, Techniche Universität Berlin, 2023.

[285] J. Laflamme Janssen, M. Côté, S. G. Louie, and M. L. Cohen, "Electron-phonon coupling in C_{60} using hybrid functionals," *Physical Review B*, vol. 81, p. 073106, 2010.

[286] C. Faber, J. L. Janssen, M. Côté, E. Runge, and X. Blase, "Electron-phonon coupling in the C_{60} fullerene within the many-body GW approach," *Physical Review B*, vol. 84, p. 155104, 2011.

[287] M. Lazzeri, C. Attaccalite, L. Wirtz, and F. Mauri, "Impact of the electron-electron correlation on phonon dispersion: failure of LDA and GGA DFT functionals in graphene and graphite," *Physical Review B*, vol. 78, p. 081406, 2008.

[288] Z. P. Yin, A. Kutepov, and G. Kotliar, "Correlation-enhanced electron-phonon coupling: applications of GW and screened hybrid functional to bismuthates, chloronitrides, and other high-T_c superconductors," *Physical Review X*, vol. 3, p. 021011, 2013.

[289] C. E. P. Villegas, A. R. Rocha, and A. Marini, "Anomalous temperature dependence of the band gap in black phosphorus," *Nano Letters*, vol. 16, no. 8, pp. 5095–5101, 2016.

[290] J. Wu, W. Walukiewicz, K. M. Yu, J. W. Ager, E. E. Haller, H. Lu, W. J. Schaff, Y. Saito, and Y. Nanishi, "Unusual properties of the fundamental band gap of InN," *Applied Physics Letters*, vol. 80, no. 21, pp. 3967–3969, 2002.

[291] S. Lewonczuk, J. G. Gross, and J. Ringeissen, "Temperature dependence of the spin-orbit coupling and energy gap in cuprous bromide," *Journal de Physique Lettres*, vol. 42, no. 4, pp. 91–94, 1981.

[292] Y. Kaifu and T. Komatsu, "Exciton line-width and exciton-phonon interaction in CuCl," *Physica Status Solidi B*, vol. 48, no. 2, pp. K125–K128, 1971.

[293] A. Göbel, T. Ruf, M. Cardona, C. Lin, J. Wrzesinski, M. Steube, and K. Reimann, "Effects of the isotopic composition on the fundamental gap of CuCl," *Physical Review B*, vol. 57, no. 24, pp. 15183–15190, 1998.

[294] N. Garro, A. Cantarero, M. Cardona, T. Ruf, A. Göbel, C. Lin, K. Reimann, S. Rübenacke, and M. Steube, "Electron-phonon interaction at the direct gap of the copper halides," *Solid State Communications*, vol. 98, no. 1, pp. 27–30, 1996.

[295] R. N. Tauber, A. A. Machonis, and I. B. Cadoff, "Thermal and optical energy gaps in PbTe," *Journal of Applied Physics*, vol. 37, no. 13, pp. 4855–4860, 1966.

[296] E. Cannuccia and A. Marini, "Effect of the quantum zero-point atomic motion on the optical and electronic properties of diamond and trans-polyacetylene," *Physical Review Letters*, vol. 107, p. 255501, 2011.

[297] J.-M. Lihm and C.-H. Park, "Phonon-induced renormalization of electron wave functions," *Physical Review B*, vol. 101, p. 121102, 2020.

[298] S. Chmiela, H. E. Sauceda, K.-R. Müller, and A. Tkatchenko, "Towards exact molecular dynamics simulations with machine-learned force fields," *Nature Communications*, vol. 9, no. 1, p. 3887, 2018.

[299] S. Batzner, A. Musaelian, L. Sun, M. Geiger, J. P. Mailoa, M. Kornbluth, N. Molinari, T. E. Smidt, and B. Kozinsky, "E(3)-equivariant graph neural networks for data-efficient and accurate interatomic potentials," *Nature Communications*, vol. 13, no. 1, p. 2453, 2022.

[300] H. E. Sauceda, L. E. Gálvez-González, S. Chmiela, L. O. Paz-Borbón, K.-R. Müller, and A. Tkatchenko, "BIGDML –towards accurate quantum machine learning force fields for materials," *Nature Communications*, vol. 13, no. 1, p. 3733, 2022.

[301] R. Drautz, "Atomic cluster expansion for accurate and transferable interatomic potentials," *Physical Review B*, vol. 99, p. 014104, 2019.

[302] L. Zhang, B. Onat, G. Dusson, A. McSloy, G. Anand, R. J. Maurer, C. Ortner, and J. R. Kermode, "Equivariant analytical mapping of first principles Hamiltonians to accurate and transferable materials models," *npj Computational Materials*, vol. 8, no. 1, p. 158, 2022.

[303] K. T. Schütt, F. Arbabzadah, S. Chmiela, K. R. Müller, and A. Tkatchenko, "Quantum-chemical insights from deep tensor neural networks," *Nature Communications*, vol. 8, no. 1, p. 13890, 2017.

[304] J. Gilmer, S. S. Schoenholz, P. F. Riley, O. Vinyals, and G. E. Dahl, "Neural message passing for quantum chemistry," in *Proceedings of the 34th International Conference on Machine Learning* (D. Precup and Y. W. Teh, eds.), vol. 70 of *Proceedings of Machine Learning Research*, pp. 1263–1272, PMLR, 2017.

[305] H. Li, Z. Wang, N. Zou, M. Ye, R. Xu, X. Gong, W. Duan, and Y. Xu, "Deep-learning density functional theory Hamiltonian for efficient ab initio electronic-structure calculation," *Nature Computational Science*, vol. 2, no. 6, pp. 367–377, 2022.

[306] K. Lejaeghere *et al.*, "Reproducibility in density functional theory calculations of solids," *Science*, vol. 351, no. 6280, p. aad3000, 2016.

[307] A. H. Larsen, J. J. Mortensen, *et al.*, "The atomic simulation environment—a Python library for working with atoms," *Journal of Physics: Condensed Matter*, vol. 29, no. 27, p. 273002, 2017.

[308] A. Jain, S. P. Ong, W. Chen, B. Medasani, X. Qu, M. Kocher, M. Brafman, G. Petretto, G.-M. Rignanese, G. Hautier, D. Gunter, and K. A. Persson, "Fireworks: a dynamic workflow system designed for high-throughput applications," *Concurrency and Computation: Practice and Experience*, vol. 27, no. 17, pp. 5037–5059, 2015.

[309] T. J. Scheidemantel, C. Ambrosch-Draxl, T. Thonhauser, J. V. Badding, and J. O. Sofo, "Transport coefficients from first-principles calculations," *Physical Review B*, vol. 68, p. 125210, 2003.

[310] G. K. Madsen and D. J. Singh, "BoltzTraP. A code for calculating band-structure dependent quantities," *Computer Physics Communications*, vol. 175, no. 1, pp. 67–71, 2006.

[311] G. K. Madsen, J. Carrete, and M. J. Verstraete, "BoltzTraP2 a program for interpolating band structures and calculating semi-classical transport coefficients," *Computer Physics Communications*, vol. 231, pp. 140–145, 2018.

[312] G. Samsonidze and B. Kozinsky, "Accelerated screening of thermoelectric materials by first-principles computations of electron–phonon scattering," *Advanced Energy Materials*, vol. 8, no. 20, p. 1800246, 2018.

[313] A. M. Ganose, J. Park, A. Faghaninia, R. Woods-Robinson, K. A. Persson, and A. Jain, "Efficient calculation of carrier scattering rates from first principles," *Nature Communications*, vol. 12, no. 1, p. 2222, 2021.

[314] R. Kubo, "Statistical-mechanical theory of irreversible processes I. General theory and simple applications to magnetic and conduction problems," *Journal of the Physical Society of Japan*, vol. 12, no. 6, pp. 570–586, 1957.

[315] D. A. Greenwood, "The Boltzmann equation in the theory of electrical conduction in metals," *Proceedings of the Physical Society*, vol. 71, no. 4, p. 585, 1958.

[316] L. Calderín, V. Karasiev, and S. Trickey, "Kubo–Greenwood electrical conductivity formulation and implementation for projector augmented wave datasets," *Computer Physics Communications*, vol. 221, pp. 118–142, 2017.

[317] Z. Yuan, *Electrical conductivity from first principles.* PhD thesis, Humboldt-Universität zu Berlin, Mathematisch-Naturwissenschaftliche Fakultät, 2022.

[318] L. Cheng, C. Zhang, and Y. Liu, "How to resolve a phonon-associated property into contributions of basic phonon modes," *Journal of Physics: Materials*, vol. 2, no. 4, p. 045005, 2019.

[319] J. Li, L. Wang, J. Liu, R. Li, Z. Zhang, and X.-Q. Chen, "Topological phonons in graphene," *Physical Review B*, vol. 101, p. 081403, 2020.

[320] M. Fechner, S. Ostanin, and I. Mertig, "Effect of the surface polarization in polar perovskites studied from first principles," *Physical Review B*, vol. 77, no. 9, p. 094112, 2008.

[321] D. I. Bilc, R. Orlando, R. Shaltaf, G.-M. Rignanese, J. Íñiguez, and P. Ghosez, "Hybrid exchange-correlation functional for accurate prediction of the electronic and structural properties of ferroelectric oxides," *Physical Review B*, vol. 77, p. 165107, 2008.

[322] N. A. Spaldin, "A beginner's guide to the modern theory of polarization," *Journal of Solid State Chemistry*, vol. 195, pp. 2–10, 2012.

[323] C. Adamo and V. Barone, "Toward reliable density functional methods without adjustable parameters: The pbe0 model," *The Journal of Chemical Physics*, vol. 110, no. 13, pp. 6158–6170, 1999.

[324] G. Sàghi-Szabó, R. E. Cohen, and H. Krakauer, "First-principles study of piezoelectricity in PbTiO3," *Physical Review Letters*, vol. 80, no. 19, pp. 4321–4324, 1998.

[325] S. J. Ahmed, J. Kivinen, B. Zaporzan, L. Curiel, S. Pichardo, and O. Rubel, "BerryPI: a software for studying polarization of crystalline solids with WIEN2k density functional all-electron package," *Computer Physics Communications*, vol. 184, no. 3, pp. 647–651, 2013.

[326] Y. Zhang, J. Sun, J. P. Perdew, and X. Wu, "Comparative first-principles studies of prototypical ferroelectric materials by LDA, GGA, and SCAN meta-GGA," *Physical Review B*, vol. 96, p. 035143, 2017.

[327] W. Zhong, R. D. King-Smith, and D. Vanderbilt, "Giant LO-TO splittings in perovskite ferroelectrics," *Physical Review Letters*, vol. 72, pp. 3618–3621, 1994.

[328] H. H. Wieder, "Electrical behavior of barium titanate single crystals at low temperatures," *Physical Review*, vol. 99, pp. 1161–1165, 1955.

[329] J. D. Axe, "Apparent ionic charges and vibrational eigenmodes of $BaTiO_3$ and other perovskites," *Physical Review*, vol. 157, no. 2, pp. 429–435, 1967.

[330] M. M. V. Gavrilyachenko, R. Spinko and E. Fesenko, "Spontaneous polarization and coercive field of lead titanate," *Soviet Physics Solid State*, vol. 12, p. 1532, 1970.

[331] J. P. Remeika and A. M. Glass, "The growth and ferroelectric properties of high resistivity single crystals of lead titanate," *Materials Research Bulletin*, vol. 5, no. 1, pp. 37–45, 1970.

[332] K. Carl, "Ferroelectric properties and fatiguing effects of modified PbTiO3 ceramics," *Ferroelectrics*, vol. 9, no. 1, pp. 23–32, 1975.

[333] G. Shirane, H. Danner, and R. Pepinsky, "Neutron diffraction study of orthorhombic $BaTiO_3$," *Physical Review*, vol. 105, pp. 856–860, 1957.

[334] H. L. R. B. T. Toshio, K.H. Hellwege and O. Madelung, *in Ferro- and Antiferroelectric Substances, edited by K.-H. Hellwege and A. M. Hellwege, Landolt-Börnstein, Group III, Vol. 3.* Springer-Verlag, Berlin, 1981.

[335] H. Meštrić, R.-A. Eichel, T. Kloss, K.-P. Dinse, S. Laubach, S. Laubach, P. C. Schmidt, K. A. Schönau, M. Knapp, and H. Ehrenberg, "Iron-oxygen vacancy defect centers in $PbTiO_3$: Newman superposition model analysis and density functional calculations," *Physical Review B*, vol. 71, p. 134109, 2005.

[336] R. Nelmes and W. Kuhs, "The crystal structure of tetragonal $PbTiO_3$ at room temperature and at 700 K," *Solid State Communications*, vol. 54, no. 8, pp. 721–723, 1985.

[337] P. Ghosez, X. Gonze, P. Lambin, and J. P. Michenaud, "Born effective charges of barium titanate: band-by-band decomposition and sensitivity to structural features," *Physical Review B*, vol. 51, no. 10, pp. 6765–6768, 1995.

[338] H. Judith Grenville-Wells and K. Lonsdale, "X-ray study of laboratory-made diamonds," *Nature*, vol. 181, no. 4611, pp. 758–759, 1958.

[339] M. Feneberg, M. Röppischer, C. Cobet, N. Esser, J. Schörmann, T. Schupp, D. J. As, F. Hörich, J. Bläsing, A. Krost, and R. Goldhahn, "Optical properties of cubic GaN from 1 to 20 eV," *Physical Review B*, vol. 85, p. 155207, 2012.

[340] S. Porowski, "Growth and properties of single crystalline GaN substrates and homoepitaxial layers," *Materials Science and Engineering: B*, vol. 44, no. 1, pp. 407–413, 1997. 3rd International Workshop on Expert Evaluation and Control of Compound Semiconductor Materials and Technologies.

[341] J. H. Eggert, D. G. Hicks, P. M. Celliers, D. K. Bradley, R. S. McWilliams, R. Jeanloz, J. E. Miller, T. R. Boehly, and G. W. Collins, "Melting temperature of diamond at ultrahigh pressure," *Nature Physics*, vol. 6, no. 1, pp. 40–43, 2010.

[342] F. Knoop, T. A. R. Purcell, M. Scheffler, and C. Carbogno, "FHI-vibes: ab initio vibrational simulations," *Journal of Open Source Software*, vol. 5, no. 56, p. 2671, 2020.

[343] W. G. Hoover, A. J. C. Ladd, and B. Moran, "High-strain-rate plastic flow studied via nonequilibrium molecular dynamics," *Physical Review Letters*, vol. 48, pp. 1818–1820, 1982.

[344] D. J. Evans, "Computer experiment for nonlinear thermodynamics of Couette flow," *The Journal of Chemical Physics*, vol. 78, no. 6, pp. 3297–3302, 1983.

Declaration

I declare that I have completed the thesis independently using only the aids and tools specified. I have not applied for a doctor's degree in the doctoral subject elsewhere and do not hold a corresponding doctor's degree. I have taken due note of the Faculty of Mathematics and Natural Sciences PhD Regulations, published in the Official Gazette of Humboldt-Universität zu Berlin no. 42/2018 on 11/07/2018.

Nikita Rybin
Berlin, February, 2023